Section III

Stellar Atmospheres and Circumstellar Matter, Planetary Atmospheres

The Sobolev Approximation in the Development and Astrophysical Applications

V.P. Grinin[1,2]

E-mail: *grinin@gao.spb.ru*

The Sobolev approximation is one of the most effective methods of the modeling of emission spectra of astrophysical objects of various types. It plays also an important role in the radiative hydrodynamics. In this short review, after an introduction to the Sobolev method, I discuss the main steps in its development and astrophysical applications.

1 Introduction to the Sobolev method

Emission spectra of many astrophysical objects are formed in the media with large-scale differential motions which velocities are much greater than the thermal velocity of atoms. In these conditions, the Doppler shift of the radiation frequency leads to strong changes in optical properties of the gas in the line frequencies. This circumstance strongly complicates the solution of the radiative transfer problem. However, as shown by V.V. Sobolev [58], in the media with the large velocity gradient, the solution of this problem can be significantly simplified.

The essence of this approximation is as follows: for large velocity gradients, due to the shift between resonance frequencies of the emitting and absorbing atoms, the radiative interaction at each point of the medium $\vec{r}$ is determined by its local vicinity. The characteristic size of this vicinity is equal to the distance from the given point to that, where the aforementioned shift in resonance frequencies is equal to the half-width of the line profile function $\Delta\nu_D$ determined by the thermal (or turbulent) velocity v_t,

$$s_0 = v_t/|dv_{\vec{s}}/ds|. \tag{1}$$

Here $dv_{\vec{s}}/ds$ is the velocity gradient in the comoving coordinate system at the point $\vec{r}$ in the direction $\vec{s} = \vec{r}\,' - \vec{r}$; $s = |\vec{s}\,| \ll |\vec{r}\,|$), and $dv_{\vec{s}}/ds \simeq [\vec{v}(\vec{r}\,') - \vec{v}(\vec{r})]/s$ (see Fig. 1).

For rough estimates, the velocity gradient in this expression can be replaced by the ratio v/R, where v is the characteristic velocity of large-scale motions and R is the characteristic size occupied by the emitting gas. As a result, we obtain the approximate relation: $s_0 \approx R(v_t/v)$. The parameter s_0, which was subsequently called the "Sobolev length", is the main parameter of the Sobolev method, characterizing the size of the local vicinity of the point.

---

[1] Pulkovo Astronomical Observatory, St. Petersburg, Russia
[2] Sobolev Astronomical Institute, St. Petersburg University, St. Petersburg, Russia

V. Grinin et al. (eds) Radiation mechanisms of astrophysical objects. Yerevan: Edit Print, 2017, pp. 141–150.

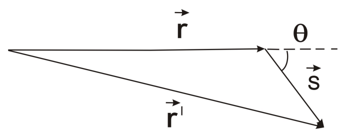

Figure 1

In general case, the equation for the source function has a form

$$S(\vec{r}) = \lambda \int_V K(\vec{r}, \vec{r}\,')\, S(\vec{r}\,')\, d\vec{r}\,' \,+\, g(\vec{r}). \tag{2}$$

Here $K(\vec{r}, \vec{r}\,')$ is the kernel function determining the density probability of a transfer of the radiative excitation from the point $\vec{r}$ to the point $\vec{r}\,'$, λ is the probability of a photon survival at a single scattering, V is the volume of the space filled in with atoms, and $g(\vec{r})$ represents the primary sources of excitation in the spectral line under consideration.

In the media with the large velocity gradient $s_0 \ll R$, Eq. (2) can be essentially simplified. In this case, one can approximately assume that the source function does not change in the vicinity of the point $\vec{r}$, and we can take it outside the integral by setting $S(\vec{r}\,') \approx S(\vec{r})$. A similar procedure can be done with the kernel function $K(\vec{r}, \vec{r}\,')$ if to replace its parameters that determine optical properties of the medium (atomic level populations, thermal or turbulent velocity) by the corresponding values at the point $\vec{r}$. Finally, one can neglect an influence of the boundaries and assume that the medium fills in an infinite volume of space. As a result, the integral equation with the very complicated kernel is transformed to the simple equation

$$S(\vec{r})\ [1 - \lambda + \lambda\beta(\vec{r})] = g(\vec{r}), \tag{3}$$

where β is the probability of a photon to escape the point of the medium $\vec{r}$ without scattering and absorption along the way

$$\beta(\vec{r}) = 1 - \int K(\vec{r}, \vec{r}\,')\, d\vec{r}\,'. \tag{4}$$

It should be noted that in the stationary medium the corresponding kernel function is always normalized to unit. This reflects the obvious fact that a photon emitted in an infinite medium will be absorbed somewhere in it. A principal difference of the radiative diffusion in a medium with a velocity gradient is that this normalization condition is violated, and the integral of the kernel function over infinite space is always less than unity. This means that because of enlightenment of the medium in the line frequencies due to the Doppler effect, there is a nonzero probability for a photon to escape from the point of the medium lying formally at the infinite distance from its boundary: $\beta(\infty) > 0$. This property of the radiation transfer in the line frequencies in moving media is the basis of the Sobolev approximation (SA).

It is important that the photon escape probability from an arbitrary point of the medium is expressed fairly simply in terms of the characteristics of the medium and the velocity field at the given point. For example, in a spherically-symmetric envelope expanding with the velocity $v(r)$ we have

$$\beta(r) = \int_0^1 \frac{1 - e^{-\tau(r,\mu)}}{\tau(r,\mu)}\, d\mu, \tag{5}$$

where $\tau(r,\mu)$ is the effective optical depth of the medium at the point r in the direction $\vec{s}$ forming an angle $\theta = \arccos\mu$ with the vector $\vec{r}$

$$\tau(r,\mu) = k(r)\, v_t |\psi(r,\mu)|^{-1}, \tag{6}$$

$k(r)$ is the integrated line opacity per unit volume (weighted with the line profile function), and

$$\psi(r,\mu) = \frac{dv_{\vec{s}}}{ds} = \frac{dv}{dr}\,\mu^2 + \frac{v}{r}\,(1-\mu^2). \tag{7}$$

In the particular case of an isotropically expanding medium (an example of which is the expanding Universe), $v(r) = Ar$, $\psi(r,\mu) = v/r$ and $\tau(r,\mu) = constant = k\, v_t/A$. As a result, $\beta(r) = (1 - e^{-\tau(r)})/\tau(r)$. From this, we get $\beta = 1/\tau$ for $\tau \gg 1$.

Thus, if the primary sources of excitation $g(\vec{r})$ in the spectral line are known, then we can immediately calculate the source function from Eq. (3), and then calculate the intensity of the spectral line. This method has been originally developed by V.V. Sobolev for the case of a rectangular line profile function and the complete frequency redistribution in a comoving frame. Later, in 1957, he considered in [59] the general case of an arbitrary absorption coefficient. It turned out that the expression for the photon escape probability $\beta(r)$ does not depend on the type of the line profile function. This invariance is one of the most interesting properties of the process of radiative diffusion at line frequencies in moving media which has no analog in the case of stationary media. In the latter case, as we know, the escape probability depends sensitively on the type of the line profile function (see, e.g., the book of Ivanov [42]).

Due to its simplicity, the Sobolev approximation was widely used when modeling and interpreting the emission spectra of stars with circumstellar envelopes and other astrophysical objects. The role of this method in the solution of complex, multilevel problems was especially great. First steps in this direction were taken by Rublev [54, 55], Gorbatskii [20], Boyarchuk [4], Doazan [11], Luud and Il'mas [45], Gershberg and Shnol [18], Grinin and Katysheva [28], Castor and Lamers [7], Natta and Giovanardi [50], and many others (see a more detailed bibliography of the works on this subject in the review [24]).

In 1961 Sobolev's book "Moving Envelopes of Stars" was translated into English by S. Payne-Gaposchkin and published in the USA. Soon a series of fundamental discoveries in astronomy have been done, resulting in appearance of new astrophysical objects: quasars, neutron stars and maser sources. First observations of ultraviolet spectra of stars from space led to the discovery of intense mass outflows (stellar winds) from hot supergiants. All this expanded considerably the field of the application of the SA and stimulated its further development in the papers by Castor [5, 6], Grachev [22], Rybicki and Hummer [57], Hummer and Rybicki [36, 37], Jeffery [39], Hutsemekers and Surdej [38], Petrenz and Puls [53], Dorodnitsyn [13], Grinin and Tambovtseva [30], and others (see below). In particular, the Sobolev approximation has been adapted for studying polarization in spectral lines [39], for the case of relativistic motions [38, 40] and conditions near black holes and neutron stars [12, 13, 14].

1.1 The SEI algorithm

The questions of the accuracy of the SA and the limits of its applicability naturally emerged. The development of numerical and asymptotic methods of the radiative transfer theory has made possible the solution of this problem. It turned out that the limits of applicability of the SA depend sensitively on the type of the line profile function and are determined by the asymptotic behavior of the kernel function in Eq. (2). These and related topics are discussed in more detail in the review papers by Grachev [23] and Grinin [24].

Using the numerical methods, Bastian et al. [2] and Hamann [31] investigated in detail the accuracy of the SA in models of spherically symmetric outflows. They have shown that the error in the calculations performed on the basis of the SA arises mainly when calculating the line profile, while accuracy of the source function calculations was quite good. Based on this result, Bertout [3] and Lamers et al. [44] suggested to use the exact expression for the intensity of the radiation emerging from the medium in the combination with the source function calculated in the Sobolev approximation. This algorithm is known as the Sobolev Exact Integration (SEI) method [44]. It yields a considerable gain in accuracy of the line profiles and is widely used when modeling the emission spectra.

2 The non-local approximation

In the seventies it was found that the presence of the large gradient velocity in the emitting region actually still does not guarantee the condition of locality of the radiative interaction at the line frequencies, and one additional condition must be fulfilled. Namely, the derivative of the velocity in the comoving coordinate system, $dv_{\vec{s}}/ds$ has to be a positive definite function of the angle θ between the vector $\vec{r}$ and the arbitrary direction $\vec{s}$. In the case of radially symmetric motions, this condition is fulfilled for the outflow with the acceleration ($dv/dr > 0$) and does not fulfilled in the case of decelerated outflows. The latter is also true in the case of accretion flows, including the quasi-Keplerian disks. In these cases, at each point $\vec{r}$ there are directions along which $dv_{\vec{s}}/ds = 0$, and the Sobolev length $s_0 = \infty$ (see Fig. 2).

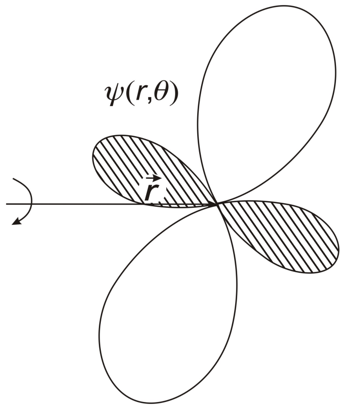

Figure 2: Azimuthal structure of the velocity gradient in the comoving frame in the plane of the quasi-Keplerian disk (from [29]). In the filled regions $\psi(r,\theta) < 0$.

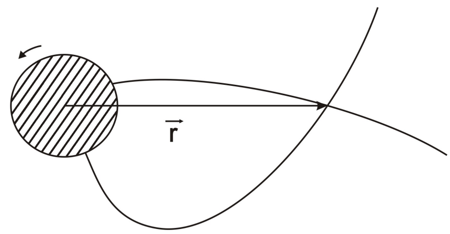

Figure 3: The common-point velocity surface in the rotating and collapsing envelope (from [24]).

These distinctions in the structure of the velocity field in the comoving frame are key for definition of a type of the radiative interaction in a moving medium. The equation for the source function in the case of the non-local radiative interaction was first obtained by Grachev and Grinin [21]. They showed that in shells expanding with deceleration, the source function is determined by the equation

$$S(\vec{r})\,\left[1-\lambda+\lambda\beta(\vec{r})\right] = \lambda \int_{\Omega_c} S(\vec{r}\,')\,\left[1-e^{-\tau(\vec{r}\,',\theta')}\right]\,\beta(\vec{r},\theta)\,\frac{d\Omega}{4\pi} + g(\vec{r}), \qquad (8)$$

which differs from Eq. (3) by the integral term. This additional term allows for the fact that besides the local vicinity of the point, a contribution to photoexcitations at the point $\vec{r}$ comes from the so-called surfaces of comoving points that are in resonance with the point $\vec{r}$ and satisfy the equation $(\vec{v}(\vec{r}\,') - \vec{v}(\vec{r}))\cdot\vec{s} = 0$. An example of such a surface is presented in Fig. 3. The existence of such surfaces provides for the non-local nature of the radiative interaction in media moving with large velocity gradients.

An equation similar to Eq. (8) was derived independently and investigated in detail by Rybicki and Hummer [56]. They introduced the term "the common points surface" which has now become generally accepted. We should also note a paper by Deguchi and Fukui [9] in which Eq. (8) was derived and used for calculations of the spectra of collapsing protostellar clouds as well as a version of a non-local radiative interaction between components of a resonance doublet in moving media, considered by Surdej [60].

Let us note that the integral term in this equation does not contain any new quantities in comparison with the local version of the Sobolev approximation. We see the same expressions for the escape probability β and for the effective optical depth τ as in Eq. (3). An analysis shows that the contribution of the integral term in Eq. (8) to the source function depends on two factors: on the behavior of the primary sources of excitation $g(r)$ and on the solid angle Ω_c in which the surface of comoving points is seen from the point $\vec{r}$. For $\Omega_c \ll 4\pi$, the influence of the integral term on the source function can be neglected in most cases. The non-local version of the Sobolev approximation is applied to modeling the emitting regions around young stars (see, e.g., the works of Hartmann et al. [33], Muzerolle et al. [49]), black holes and neutron stars (the paper of Dorodnitsyn [14]), supernova shells (that of Fransson [16]) and other astrophysical objects. It is interesting to note that the non-local radiative interaction can take place near to the compact objects (black holes and neutron stars) in the *accelerating outflows* due to the gravitation red shift (the work of Dorodnitsyn [13]). In this case the P Cygni profile may have both red- and blue-shifted absorption troughs (in contrast with the classical theory).

3 The radiative force

Due to the large cross sections of the interaction with matter, radiation in spectral lines plays an important role in the dynamics of gas in high-luminosity astrophysical objects. In 1957 Sobolev [59] has obtained the formula for the radiative force in the plane-parallel layer expanding with a constant velocity gradient. Only diffuse radiation produced in the layer was taken into account. The next important step was made by Castor [5]. Developing the ideas laid down in the SA, he has obtained the expression for the radiative force exerted on the gas in a spherically symmetric expanding shell with absorption and scattering of continuous stellar radiation in the line frequencies. It has a simple form

$$f_{r,L} = \frac{k(r)\, F_c\, \Delta\nu_D}{c}\, \min(1, 1/\tau), \tag{9}$$

where F_c is the radiation flux at the stellar surface at the frequency of the spectral line under consideration, k is the integrated line opacity (normalized to a unit of mass), c is the speed of light, and τ is the optical depth defined by Eqs. (6)–(7). Castor, Abbott, and Klein (CAK) [8] subsequently calculated models of the expanding envelopes of hot supergiants and showed that the main contribution to the radiative force comes from a set of weak subordinate lines of ionized atoms such as CII, CIII, etc. It is needed to note that in the earlier attempts to solve this problem it was assumed that the main contribution to the radiative force provided the ultraviolet resonance lines (see the works of Lucy and Solomon [46], Lucy [47]). However, their effect was too small to explain the high mass loss rate from the hot supergiants.

The CAK theory has had a significant effect on the development of the theory of radiative driven stellar winds. Due to the efforts of Castor and his co-authors, this theory is now one of the most advanced fields of theoretical astrophysics. The results of this theory are applied not only to calculations of the radiative driven winds from hot stars but also to modeling of the envelopes and disk winds of quasars and active galactic nuclei.

3.1 The azimuthal component of the radiative force

Completing the topic of the radiative force in moving media, we note one non-trivial property of this mechanism. It consists in the fact that in envelopes with axially symmetric motions, along with the radial component $f_{r,L}$ of the radiative force there is also an azimuthal component $f_{\theta,L}$. Its appearance is related to the fact that in the general case of axially symmetric motions, the derivative of the velocity in the comoving frame in the plane of the motions includes the odd dependence on the angle θ between the vector $\vec{r}$ and the arbitrary direction $\vec{s}$ in the plane of motions

$$\frac{dv_{\vec{s}}}{ds} = \frac{dv}{dr}\cos^2\theta + \frac{v}{r}\sin^2\theta + \left(\frac{du}{dr} - \frac{u}{r}\right)\sin\theta\,\cos\theta. \tag{10}$$

For this reason, the Sobolev length $s_0(r,\theta)$ and, therefore, the optical properties of the medium at the line frequencies are asymmetric functions of the angle θ (Fig. 2). Radiation in the spectral line propagates in such a medium not along the radius vector $\vec{r}$ but at some angle to it. This angle depends on the ratio between the radial and tangential velocity components v and u. A result of this is an azimuthal component of the radiative force. Its sign depends on the physical conditions in the envelope, such as the gradient of the source function and the direction of the radial velocity (expansion or accretion). Depending on these parameters, the direction of the azimuthal radiative force can either coincide with the rotation of a gaseous envelope or act against the rotation. The efficiency of this mechanism, operating on the principle of "Segner's wheel", depends on the ratio between the radiation density at spectral lines frequencies and the kinetic energy of gas as well as on the ratio between the velocity components v and u. For example, in the accretion disks $v \ll u$, and the ratio $f_{\theta,L}/f_{r,L} \sim v/u \ll 1$. More detailed information on this radiative mechanism can be found in [25, 26, 27]. Here we only note that in 1995 Owocki, Cranmer, and Gayley [52] independently discovered a similar effect in a numerical solution of the radiative hydrodynamics equations in the envelopes of Be stars (see also [17]).

4 Molecular lines and cosmic masers

Despite the fact that the velocities of internal motions in interstellar molecular clouds do not exceed several kilometers per second, as a rule, they nevertheless can also be objects to which SA can be applied. Because of the low temperatures, the velocities of thermal motions of molecules in the clouds are also very small and often do not exceed several hundreds of meters per second. This fact has been used by many authors who have used the SA for the diagnostics of interstellar clouds based on molecular line intensities. In particular, Goldreich and Kylafis [19], and Deguchi and Watson [10] used the SA to study the polarization of molecular lines.

In cosmic masers the optical depth of the emitting region with an inverted population of molecular levels plays the role of the amplification factor, and in the case of powerful masers it can be much larger than unity. Under these conditions, even a relatively small number of working molecules going out of resonance can cause considerable changes in the maser emission intensity (e.g., the paper of Watson and Wyld [63]). Maser lines are therefore the most sensitive indicators of internal motions of the medium, especially in the case of unsaturated regime. For the same reason, maser emission is also very sensitive to the type of radiative interaction in the medium. Really, only at the non-local radiative interaction, at each point of the medium there are directions in which the velocity gradient in the comoving coordinate system equals zero. In particular, in the quasi-Keplerian disk the equation $\psi(r, \mu) = 0$ has four solutions: $\mu_1, \ldots, \mu_4$ (Fig. 2). In terms of the SA, the optical depth in the line frequencies in these directions formally becomes infinite.

To determine the effective optical depth in this case, one must allow for the second order derivative of the velocity (see Fig. 4) from the work of Grinin and Grigor'ev [29]). Typical examples of such objects are the quasi-Keplerian disks (see, e.g., the paper by Babkovskaia et al. [1]) as well as protostellar clouds in the phase of gravitational contraction. It should be also noted that in addition to a velocity gradient, the maser lines can be also sensitive to the presence of magnetic field. These are the hydroxyl masers and some others. Calculations of such masers require joint allowance for the velocity and magnetic field gradients (see the work of Kegel and Varshalovich [41]).

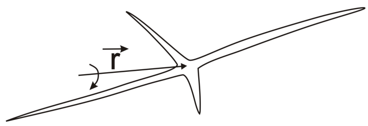

Figure 4: Azimuthal structure of the optical depth in the maser line in the plane of the quasi-Keplerian disk (from [29]).

Thus, despite the appearance of the effective numerical methods (see, e.g., [48, 35, 34] and references there), the Sobolev approximation is an important tool for modeling and diagnostics of emitting regions in the different kinds of astrophysical objects. It is applied in combination with the Monte Carlo method for modeling of the complex emitting regions near the young stars (see, e.g., the papers of Harries [32], Kurosawa et al. [43]). The unique object of application of the SA is the expanding Universe (e.g., the work of Dubrovich and Grachev [15]) which can be optically very thick for the L_α radiation at the large red shifts as shown by Varshalovich and Syunyaev [62]. It is also difficult to overestimate the role of the SA in the theory of the radiative driving stellar winds (see the paper of Owocki and Puls [51] and references therein).

References

1. *N. Babkovskaia, Ju. Poutanen, A.M.S. Richards, R. Szczerba*, Mon. Not. Roy. Astron. Soc., **370**, 1921, 2006.
2. *U. Bastian, C. Bertout, L. Stenholm, R. Wehrse*, Astron. Astrophys., **86**, 105, 1980.

3. *C. Bertout*, Astrophys. J., **285**, 269, 1984.
4. *A.A. Boyarchuk*, Izv. Krym. Astrofiz. Obs., **35**, 45, 1966.
5. *J. Castor*, Mon. Not. Roy. Astron. Soc., **149**, 111, 1970.
6. *J. Castor*, Mon. Not. Roy. Astron. Soc., **169**, 279, 1974.
7. *J. Castor, H.J.G.L.M. Lamers*, Astrophys. J. Suppl., **39**, 481, 1979.
8. *J. Castor, D.C. Abbott, R.I. Klein*, Astrophys. J., **195**, 157, 1975.
9. *S. Deguchi, Y. Fukui*, Publ. Astron. Soc. Japan, **29**, 683, 1977.
10. *S. Deguchi, W.D. Watson*, Astrophys. J., **285**, 126, 1984.
11. *V. Doazan*, Ann. Astrophys., **28**, 1, 1965.
12. *A.V. Dorodnitsyn, I.D. Novikov*, Astrophys. J., **621**, 932, 2005.
13. *A.V. Dorodnitsyn*, Mon. Not. Roy. Astron. Soc., **393**, 1433, 2009.
14. *A.V. Dorodnitsyn*, Mon. Not. Roy. Astron. Soc., **406**, 1060, 2010.
15. *V.K. Dubrovich, S.I. Grachev*, Astron. Lett., **31**, 359, 2005.
16. *C. Fransson*, Astron. Astrophys., **133**, 264, 1984.
17. *K.G. Gayley, S.P. Owocki*, Astrophys. J., **537**, 461, 2000.
18. *R.E. Gershberg, E.E. Shnol*, Izv. Krym. Astrofiz. Obs., **50**, 122, 1974.
19. *P. Goldreich, N.D. Kylafis*, Astrophys. J., **253**, 606, 1982.
20. *V.G. Gorbatskii*, Astron. Zh., **41**, 849, 1964.
21. *S.I. Grachev, V.P. Grinin*, Astrophys., **20**, 190, 1975.
22. *S.I. Grachev*, Astrophys., **13**, 95, 1977.
23. *S.I. Grachev*, Trudy Astron. Obs. St.Peterburg Univ., **44**, 203, 1994.
24. *V.P. Grinin*, Astrophys., **20**, 190, 1984.
25. *V.P. Grinin*, Astrophys., **14**, 537, 1978.
26. *V.P. Grinin*, Astrophys., **16**, 123, 1980.
27. *V.P. Grinin*, Astrophys., **17**, 109, 1981.
28. *V.P. Grinin, N.A. Katysheva*, Izv. Krym. Astrofiz. Obs. (Bull. Crimean Astrophys. Obs.), **62**, 59, 1980.
29. *V.P. Grinin, S.A. Grigor'ev*, Sov. Astron., **27**, 298, 1983.
30. *V.P. Grinin, L.V. Tambovtseva*, Astron. Rep., **55**, 704, 2011.
31. *W.-R. Hamann*, Astron. Astrophys., **93**, 353, 1981.
32. *T.J. Harries*, Mon. Not. Roy. Astron. Soc., **315**, 722, 2000.
33. *L. Hartmann, R., Hewett, N. Calvet*, Astrophys. J., **426**, 669, 1994.
34. *D.J. Hillier, D.L. Miller*, Astrophys. J., **496**, 407, 1998.

35. *D.J. Hillier*, Astron. Astrophys., **231**, 116, 1990.

36. *D.G. Hummer, G.B. Rybicki*, Astrophys. J., **293**, 258, 1985.

37. *D.G. Hummer, G.B. Rybicki*, Astrophys. J., **378**, 248, 1992.

38. *D. Hutsemekers, J. Surdej*, Astrophys. J., **361**, 367, 1990.

39. *D. Jeffery*, Astrophys. J. Suppl., **71**, 951, 1989.

40. *D. Jeffery*, Astrophys. J., **415**, 734, 1993.

41. *W.H. Kegel, D.A. Varshalovich*, Nature, **286**, 136, 1980.

42. *V.V. Ivanov*, Radiative Transfer and the Spectra of Celestial Bodies. Moscow: Nauka, 1969.

43. *R. Kurosawa, M.M. Romanova, T.J. Harries*, Mon. Not. Roy. Astron. Soc., **416**, 2623, 2011.

44. *H.J. Lamers, M. Cerruti-Sola, M. Perinotto*, Astrophys. J., **314**, 726, 1987.

45. *L. Luud, M. Il'mas*, Emission Lines in Stellar Spectra. Tartu, 1974.

46. *L.B. Lucy, P. Solomon*, Astrophys. J., **159**, 879, 1970.

47. *L.B. Lucy*, Astrophys. J., **163**, 95, 1971.

48. *D. Mihalas, P.B. Kunasz, D.G. Hummer*, Astrophys. J., **210**, 419, 1976.

49. *J. Muzerolle, P. D'Alessio, N. Calvet, L. Hartmann*, Astrophys. J., **617**, 406, 2004.

50. *A. Natta, C. Giovanardi*, Astrophys. J., **356**, 646, 1990.

51. *S.P. Owocki, J. Puls*, Astrophys. J., **510**, 355, 1999.

52. *S.P. Owocki, S.R. Cranmer, K.G. Gayley*, Astrophys. J. Lett., **472**, L115, 1996.

53. *P. Petrenz, J. Puls*, Astron. Astrophys., **358**, 956, 2000.

54. *S.V. Rublev*, Sov. Astron. **3**, 76, 1961.

55. *S.V. Rublev*, Sov. Astron. **7**, 492, 1964.

56. *G.B. Rybicki, D.G. Hummer*, Astrophys. J., **219**, 654, 1978.

57. *G.B. Rybicki, D.G. Hummer*, Astrophys. J., **274**, 380, 1983.

58. *V.V. Sobolev*, Moving Envelopes of Stars. Cambridge: Harvard Univ. Press, 1960 (Original in Russian: Dvizhushchiesya Obolochki Zvezd. Leningrad: Izd. Leningr. Univ., 1947).

59. *V.V. Sobolev*, Astron. Zh., **34**, 694, 1957.

60. *J. Surdej*, Astron. Astrophys., **60**, 303, 1978.

61. *J. Surdej, J.P. Swings*, Astron. Astrophys., **96**, 242, 1981.

62. *D.A. Varshalovich, R.A. Syunyaev*, Astrophys., **4**, 140, 1968.

63. *W.D. Watson, H.W. Wyld*, Astrophys. J., **350**, 207, 2000.

Polarized Scattering and Biosignatures in Exoplanetary Atmospheres

S.V. Berdyugina[1]

E-mail: *berdyugina@kis.uni-freiburg.de*

Polarized scattering in planetary atmospheres is computed in the context of exoplanets. The problem of polarized radiative transfer is solved for a general case of absorption and scattering, while Rayleigh scattering and Mie polarized scattering are considered as most relevant examples. We show that (1) relative contributions of single and multiple scattering depend on the stellar irradiation and opacities in the planetary atmosphere; (2) cloud (particle) physical parameters can be deduced from the wavelength-dependent measurements of the continuum polarization and from a differential analysis of molecular band absorption; (3) polarized scattering in molecular bands increases the reliability of their detections in exoplanets; (4) photosynthetic life can be detected on other planets in visible polarized spectra with high sensitivity. These examples demonstrate the power of spectropolarimetry for exoplanetary research for searching for life in the universe.

1 Polarized radiative transfer

Radiative processes in planetary atmospheres are a classical subject, simply for the reason that we live in one. Extensive theoretical studies were carried out during the second half of the twentieth century by such giants as Sobolev [1] and Chandrasekhar [2] as well as the renown radiative transfer school at the Saint Petersburg (Leningrad) State University [3]. Most recently, physics of planetary atmospheres has become one of the most acclaimed subjects because of applications for Earth climate studies and the detection of a large variety of extrasolar planets. This paper provides the theoretical basis for studying atmospheres of exoplanets using techniques of spectropolarimetry available to us. In particular, using molecular band and continuum spectropolarimetry, one can reveal the composition of the gaseous atmosphere, particle layers (clouds, hazes, etc.) and the planetary surface, including the land, water, and life. Modeling these cases is described in this paper.

We start from solving a self-consistent radiative transfer problem for polarized scattering in a planetary atmosphere illuminated by a host star. We solve this problem under the following assumptions:

1) the atmosphere is plane-parallel and static;
2) the planet is spherically symmetric;

[1] Kiepenheuer Institut für Sonnenphysik, Freiburg, Germany

V. Grinin et al. (eds) Radiation mechanisms of astrophysical objects. Yerevan: Edit Print, 2017, pp. 151–162.

3) stellar radiation can enter the planetary atmosphere from different angles and can be polarized;
4) an incoming photon is either absorbed or scattered according to opacities in the atmosphere;
5) an absorbed photon does not alter the atmosphere (model atmosphere includes thermodynamics effects of irradiation);
6) photons can be scattered multiple times until they escape the atmosphere.

These assumptions expand those in [4], namely that multiple scattering is allowed, stellar irradiation can be polarized and vary with an incident angle, and the planetary atmosphere can be inhomogeneous in both longitude and latitude.

Then, the radiative transfer equation for the Stokes vector $\mathbf{I} = (I, Q, U, V)^{\mathrm{T}}$ of scattered polarized radiation of a given frequency (omitted for clarity) towards ($\mu = \cos\theta$, φ) is

$$\mu \frac{d\,\mathbf{I}(\tau,\mu,\varphi)}{d\tau} = \mathbf{I}(\tau,\mu,\varphi) - \mathbf{S}(\tau,\mu,\varphi) \tag{1}$$

with the total source function

$$\mathbf{S}(\tau,\mu,\varphi) = \frac{\kappa(\tau)\,\mathbf{B}(\tau) + \sigma(\tau)\,\mathbf{S}_{\mathrm{sc}}(\tau,\mu,\varphi)}{\kappa(\tau) + \sigma(\tau)}, \tag{2}$$

where κ and σ are absorption and scattering opacities, $\mathbf{S}_{\mathrm{sc}}$ and $\mathbf{B}$ are the scattering source function and the unpolarized thermal emission, respectively, and τ is the optical depth in the atmosphere with $\tau = 0$ at the top. The formal solution of Eq. (1) is (e.g., [1])

$$\mathbf{I}(\tau,\mu,\varphi) = \mathbf{I}(\tau_*,\mu,\varphi)\, e^{-(\tau_*-\tau)/\mu} + \int_{\tau}^{\tau_*} \mathbf{S}(\tau',\mu,\varphi)\, e^{-(\tau'-\tau)/\mu}\, \frac{d\tau'}{\mu}, \tag{3}$$

where τ_* is either the optical depth at the bottom of the atmosphere for the Stokes vector $\mathbf{I}^+(\tau,\mu,\varphi)$ coming from the bottom to the top ($\theta < \pi/2$) or the optical depth at the top of the atmosphere ($\tau_* = 0$) for the Stokes vector $\mathbf{I}^-(\tau,\mu,\varphi)$ coming from the top to the bottom ($\theta > \pi/2$).

The scattering source function $\mathbf{S}_{\mathrm{sc}}$ is expressed via the scattering phase matrix $\hat{\mathbf{P}}(\mu,\mu';\varphi,\varphi')$, depending on the directions of the incident (μ', φ') and scattered (μ, φ) light

$$\mathbf{S}_{\mathrm{sc}}(\tau,\mu,\varphi) = \int \hat{\mathbf{P}}(\mu,\mu';\varphi,\varphi')\, \mathbf{I}(\tau,\mu',\varphi')\, \frac{d\Omega'}{4\pi}. \tag{4}$$

It has contributions from scattering of both incident stellar light and intrinsic thermal emission. Their relative contributions depend on the frequency. For instance, for Rayleigh scattering the intensity of the thermal emission of a relatively cold planet in the blue part of the spectrum may become negligible compared to that of the scattered stellar light. The phase matrix $\hat{\mathbf{P}}(\mu,\mu';\varphi,\varphi')$ is a 4×4 matrix with six independent parameters for scattering cases on particles with a symmetry [5]. In this paper we employ the Rayleigh and Mie scattering phase matrices but our formalism is valid for other phase functions too.

The Stokes vector of the light emerging from the planetary atmosphere $\mathbf{I}(0, \mu, \varphi)$ is obtained by integrating iteratively Eqs. (2) and (3) for a given vertical distribution of the temperature and opacity in a planetary atmosphere. Boundary conditions are defined by stellar irradiation at the top, planetary thermal radiation at the bottom, and (if present) reflection from the planetary surface. Stellar irradiation can be polarized, but the planetary thermal radiation is unpolarized. In particular, stellar limb darkening and linear polarization due to scattering in the stellar atmosphere [7, 8] can be taken into account, including the influence of dark spots on the stellar surface [9]. This effect is not very large but may be important for cooler stars with large spots and planets on very short-period orbits (when the stellar radiation incident angle noticeably varies depending on the stellar limb angle). Also, stellar magnetic fields causing polarization in stellar line profiles due to the Zeeman effect can be included for given atomic and molecular lines [6]. This effect is only important for high-resolution spectropolarimetry which is not yet possible for exoplanets. Depending on the structure of the phase matrix and the boundary conditions, the equations are solved for all or a fewer Stokes vector components. Normally it takes 3–7 iterations to achieve a required accuracy. The radiation flux is then obtained by integrating the Stokes vector over the illuminated planetary surface with a coordinate grid ($6^\circ \times 6^\circ$) on the planetary surface for a given orbital phase angle as described in [4].

Our model includes the following opacity sources:

(1) Rayleigh scattering on H I, H_2, He I, H_2O, CO, CH_4 and other relevant molecules, Thomson scattering on electrons, and Mie scattering on spherical particles with a given size distribution, with all scattering species contributing to the continuum polarization;

(2) absorption in the continuum due to free-free and bound-free transitions of H I, He I, H^-, $H_2{}^+$, $H_2{}^-$, He^-, metal ionization, and collision-induced absorption (CIA) by H_2–H_2;

(3) absorption and scattering in atomic and molecular lines for particular frequencies where they contribute.

Number densities of the relevant species are calculated with a chemical equilibrium code described in [6]. Here we employ model atmospheres from [10] and [11] for stellar and planetary atmospheres, respectively, according to their effective temperatures (T_{eff}). This is appropriate for illustrating radiative transfer effects discussed in Sect. 2 and applicable for the case of highly irradiated hot Jupiters and substellar components. In particular, a model atmosphere of a hot Jupiter has to match the infrared thermal radiation of the planet originating in deeper layers, while upper layers contributing to the optical radiation are completely dominated by the incident stellar radiation. Planetary atmosphere models with specific chemical compositions and temperature–pressure (TP) structures can be also employed. For instance, the planetary atmosphere can be inhomogeneous with the vertical composition and TP-structure varying with latitude and longitude.

2 Results

2.1 Rayleigh scattering

In this section we assume that scattering in the planetary atmospheres occurs only on atoms, molecules or particles which are significantly smaller than the wavelength of scattered light, i.e., we employ the Rayleigh scattering phase matrix, including isotropic scattering intensity. In particular, we focus here on examples of resulting Stokes parameters and source functions depending on stellar irradiation and wavelength.

Figure 1 shows examples of depth dependent Stokes I source functions (top panels) and normalized emerging Stokes I and Q (bottom panels) for three distances between the star and the planet (left to right) at the wavelength of 400 nm. Here, the star is of $T_{\rm eff} = 5500\,$K, and the planet is of $T_{\rm eff} = 1500\,$K. Stokes Q is assumed to be positive when polarization is perpendicular to the scattering plane.

By studying the behavior of the source functions and Stokes parameters depending on various parameters, we conclude the following facts:

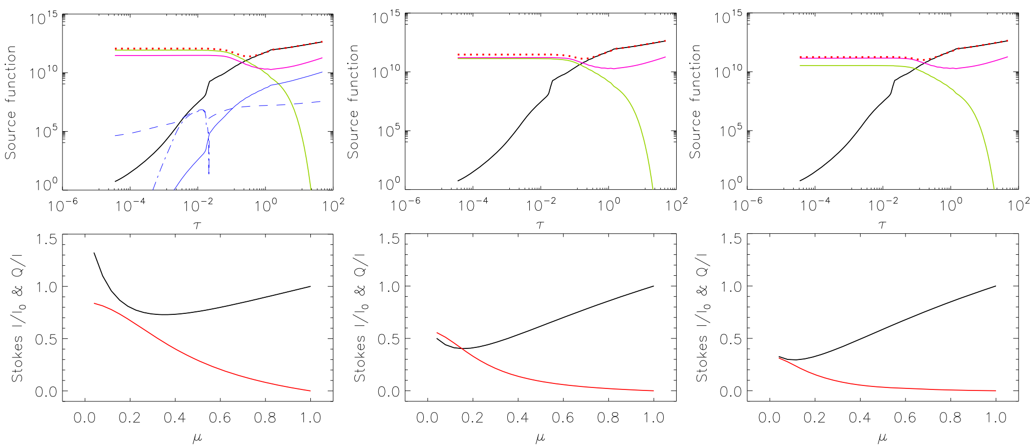

Figure 1: Stokes I source functions (top panels) and normalized emerging Stokes I and Q parameters (bottom panels) for three distances between the star and the planet: 0.02, 0.05, and 0.1 AU (left to right). The source functions are shown separately for thermal radiation of the planet (black), single scattered stellar radiation (green), multiple scattered stellar and planetary radiation (magenta), and the total one (red dotted line). The top left plot also shows relative scattering (dashed blue) and absorption (solid blue) opacities and separately particle scattering (dashed-dotted blue) as a cloud layer in the original model atmosphere (it is the same for all three panels). In the lower panels, the Stokes I/I_0 (black) is normalized to the intensity at the planet disk center ($\mu = 0$). The Stokes Q/I (red) is normalized to I at given μ. Both are at $\tau = 0$. Notice the increase of the single scattering contribution with respect to that of multiple scattering as the distance to the planet decreases (i.e., the stellar flux increases). Accordingly, the planet limb polarization and brightening increase too.

- The polarization at a given depth in the atmosphere arises due to its anisotropic irradiation, i.e., unequal illumination coming from the top and from the bottom (assuming here an azimuthal symmetry). Hence, anisotropy and polarization are small in deeper layers, where planet thermal radiation dominates, and they are larger in upper layers, where stellar irradiation dominates. The depth where this dominance alternates depends on the relative contribution of the scattering and absorption coefficients to the total opacity (which is wavelength dependent). It turns out that in cool gaseous atmospheres this occurs very deep in the atmosphere for the continuum radiation, but can be higher for radiation in cores of strong absorption atomic and molecular lines.
- This anisotropy (and, hence, polarization) is sensitive to the incident stellar flux (cf., number of photons arriving to the planet) at wavelengths where Rayleigh scattering is most efficient, i.e., in the blue part of the spectrum. Thus, hotter stars hosting closer-in planets are systems potentially producing larger polarization in the blue.
- Relative contribution of single-scattered photons with larger polarization with respect to multiple-scattered photons with lower resulting polarization increases with stellar irradiation at shorter wavelengths.
- Depending on stellar irradiation, the intensity distribution on the planetary disk, i.e., $I(0,\mu)/I(0,1)$ can decrease or increase with μ. In fact, the μ value where limb darkening turns into limb brightening approximates the optical depth τ where single and multiple scattering contributions become comparable.
- Planet limb polarization is very sensitive to the stellar irradiation because of the effects listed above. For a larger stellar flux, a larger polarization is seen for a wider range of angles.
- Considering the high sensitivity of planet polarization to stellar irradiation, variability of the stellar flux incident on the planet, e.g., caused by dark (magnetic) spots or flares, can result in a variable *amplitude* of planet polarization, while its orbital phase dependence is preserved, since the latter depends on orbital parameters only (see [4]).

The models presented in Fig. 1 are close to the case of the HD 189733b hot Jupiter which is at about 0.03 AU from its K-dwarf star with the effective temperature of about 5500 K. The relatively high polarization measured from this planet in the blue band (B-band) [12, 13] is well explained by the dominance of the single-scattered stellar photons in its upper atmosphere because of the high irradition and Rayleigh scattering cross-section in the blue. This was first proposed in [13] and further demonstrated with a simple model in [14]. Here, with the precise calculations of the polarized radiative transfer, we show that this hypothesis is valid. Moreover, multi-wavelength polarimetry allowed for estimating the planet albedo and determining its blue color. The relation between the geometrical albedo and polarization is however not so simple as was assumed in [13]. An analysis of this relation for various planetary and stellar parameters using this theory will be carried out in a separate paper.

2.2 Mie scattering

In this section we consider scattering caused by spherical particles of various sizes which can be comparable or larger than the wavelength of scattered light, i.e., we employ the Mie scattering phase matrix. For smaller particles and/or longer wavelengths, it approximates Rayleigh scattering.

Following examples in earlier literature (e.g., [5] and references therein), we assume "gamma" distribution of particle sizes: $n(r) = \mathrm{C}r^{(1-3b)/b}e^{-r/ab}$, with a and b being the effective particle radius and the effective size variance, respectively. Also, we use the so-called size parameter $2\pi a/\lambda$ which can be recalculated to λ for a given a, and vice versa. Particles are characterized by the refractive index n_r with its real part being responsible for scattering. With this, we can reproduce numerical examples in [5] as well as results for Venus in [15]. Here, we investigate scattering on highly refractive materials ($n_r > 1.5$) which are expected to be present in hot Jupiter atmospheres. For instance, olivine, which is common in the Solar system, and its endmembers forsterite Mg_2SiO_4 and fayalite Fe_2SiO_4 have a range of the refractive index from 1.6 to 1.9.

In Fig. 2 we show examples of two Mie phase matrix elements: intensity P_{11} and percent polarization $-100\%P_{21}/P_{11}$ for single scattering on particles with n_r of 1.6 (upper panels) and 1.9 (lower panels), depending on the size parameter and the scattering angle. The latter is $0°$ for forward and $180°$ for backward scattering. These examples illustrate the following known facts (e.g., [16, 15, 5]):

- Forward scattering dominates the intensity for larger particles.
- For the smallest particle size parameters, polarization is strong (up to 100%) and positive near scattering angle $90°$ due to Rayleigh scattering. For the largest size parameters, polarization approaches that of the geometrical optics, i.e., it is small at small scattering angles because of largely unpolarized diffracted light, and it is negative for a wide range of angles because of two refractions within a sphere.
- Strong positive polarization maximum near $165°$–$170°$ is the primary rainbow. It can reach 100% polarization for certain size-angle combinations.
- Strong negative polarization near $140°$–$150°$ is a "glory"-like phenomenon caused by surface waves on the scattering particle. The "glory" itself, which is a sharp maximum in polarization in the backscattering direction, can be seen on particles with larger size parameters.
- Weak positive polarization near $20°$–$30°$ is due to "anomalous diffraction" caused by interference of the diffracted, reflected and transmitted light in the forward direction.

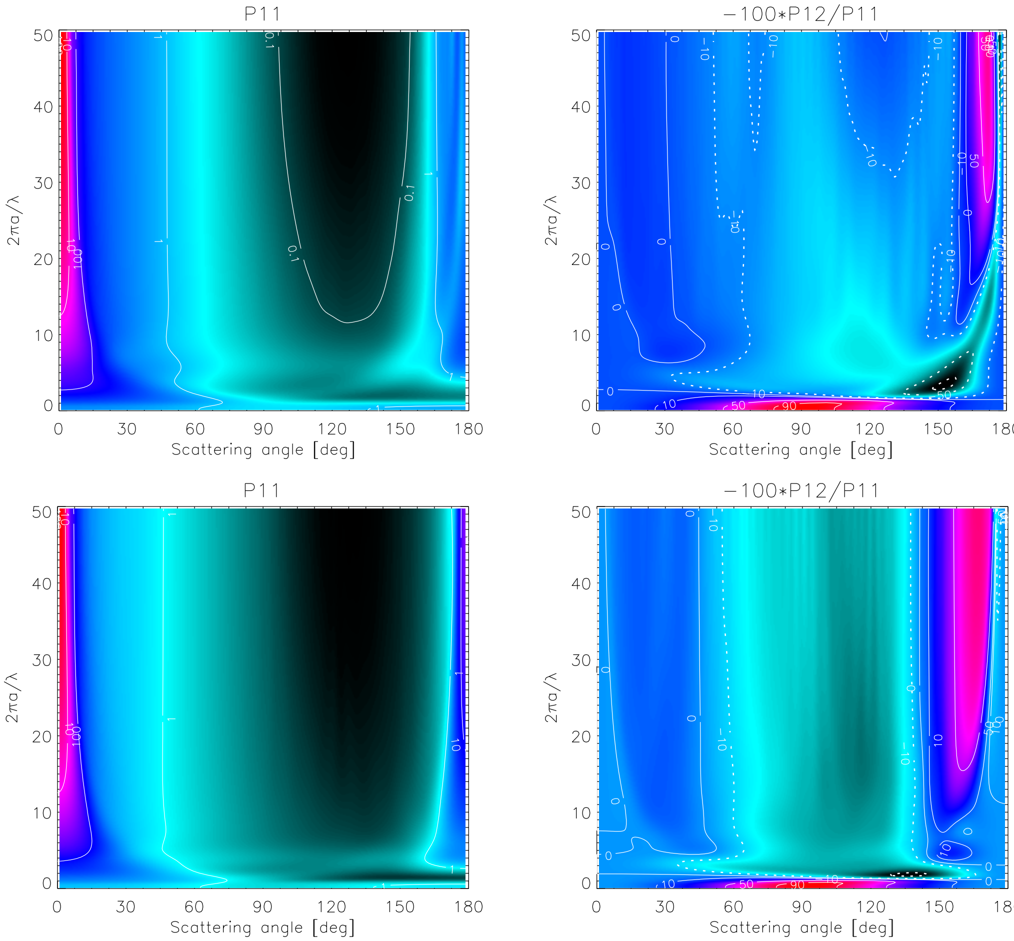

Figure 2: Mie scattering phase matrix elements P_{11} (intensity) and $-100\%P_{21}/P_{11}$ (percent polarization) for single scattering on particles with $n_r = 1.6$ (top panels) and $n_r = 1.9$ (bottom panels) and the effective particle size variance $b = 0.07$. Dotted lines are contours for negative polarization (parallel to the scattering plane).

Now we can model effects of particle scattering on limb intensity and polarization distribution in planetary atmospheres by solving the polarized radiative transfer problem as described in Sect. 1 with the corresponding phase functions. As in Sect. 2.1, we investigate radiative transfer effects depending on irradiation and atmosphere properties. We use the same model atmospheres as before but replace the original layer of scattering particles in the planetary atmosphere with layers of various properties at different heights, imitating a variety of clouds. This *ad hoc* approach allows us to study intensity and polarization depending on particle (cloud) properties. Three examples are shown in Fig. 3. One can see that clouds can significantly affect the brightness of the irradiated atmosphere at depths (angles) where scattering and absorption opacities are comparable. In the presented example of the highly irradiated

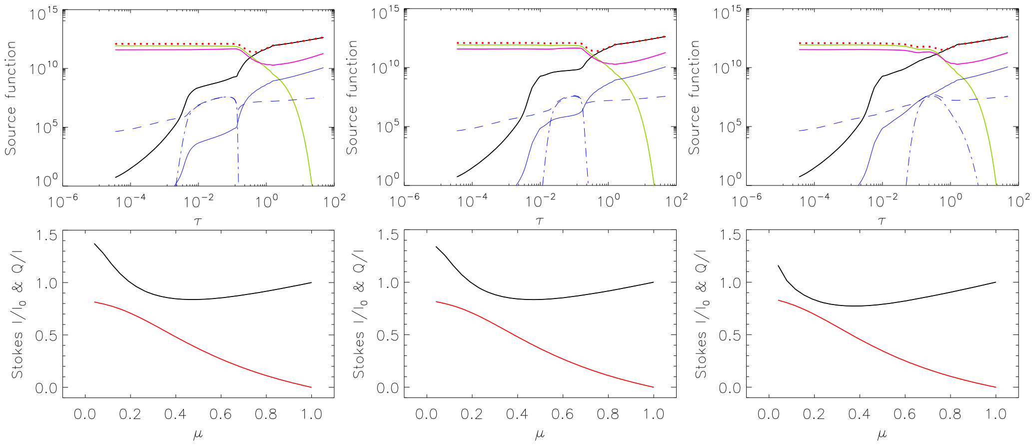

Figure 3: The same as Fig. 1 but for a planet at 0.02 AU from the star with an atmosphere containing *ad hoc* particle layers. The particles are assumed to have an effective size of 20 nm, and the layers are at the depths of 70, 80, and 90 km from the top of the atmosphere (plots are from left to right, respectively).

planetary atmosphere the polarization is still determined by the single-scattered stellar photons. In less irradiated atmospheres, the influence of particles is larger, but still according to the scattering and absorption profiles. More examples with a larger variety of clouds will be published elsewhere.

2.3 Molecular bands

Detecting molecular bands in planetary spectra is the key to their chemical composition and to their habitability assessment. By analyzing the molecular composition we can establish whether the atmosphere is in equilibrium or it is affected by such non-equilibrium processes like stellar activity or life.

Including molecular bands into polarized radiative transfer requires computation of both line absorption and scattering coefficients. We compute molecular line absorption, following [6], and molecular line scattering, following [17], where magnetic field effects on molecular absorption and scattering (the Zeeman, Paschen–Back and Hanle effects) are also included and can be employed for exoplanets. These line opacities augment the continuum opacities at molecular band wavelengths. In addition, depending on the molecular number density distribution, the maximum absorption and scattering for different molecules and bands can occur at different heights [6]. This is an important diagnostics of the atmosphere thermodynamics, e.g., TP profiles.

Despite the growing amount of information, the molecular composition of exoplanetary atmospheres is still largely unknown. Several reported detections of molecular bands were disputed by later measurements (e.g., see overview and references in [18]). Also, a few exoplanets were found to lack any spectral features in the near infrared, which was interpreted as the presence of high clouds

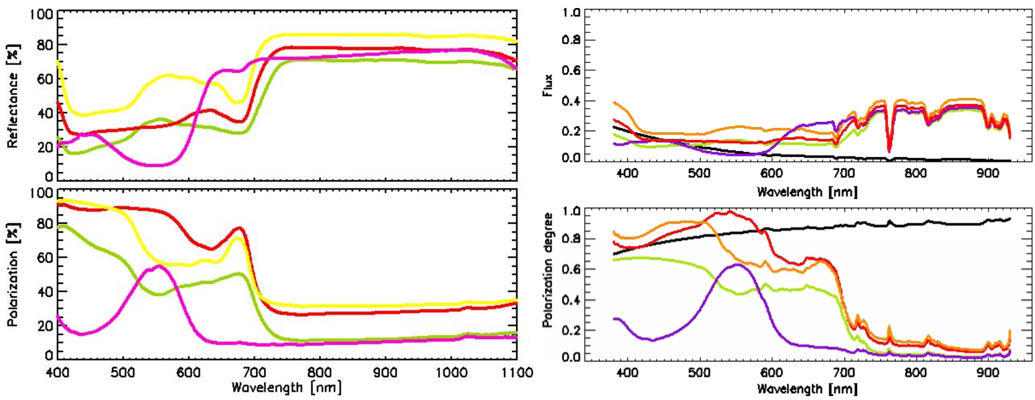

Figure 4: *Left:* reflectance and linearly polarized spectra of plant samples containing various assemblies of biopigments: chlorophyll (green), anthocyanins (red), carotenoids (yellow), phycobiliproteins (purple) [24]. Note that the higher polarization occurs at the wavelengths where these biopigments most efficiently absorb photons. The so-called "red edge" near 700 nm is clearly visible. Also, polarization and reflectance are elevated if the surface of the plant is glossy (wavelength independent), cf., in the red and yellow samples. *Right:* modeled reflectance spectra (top) and linear polarization degree spectra (bottom) for planets with the Earth-like atmosphere, 80% surface coverage by either of the four pigmented organisms shown on the left and 20% ocean surface coverage (visible hemisphere only). The high linear polarization degree clearly distinguishes the presence of the biopigments in contrast to the flux spectra. Black curve represents a planet with an ocean only [26]. The glint from its surface is highly polarized.

masking molecular absorption (e.g., [19]). To explain the presence or absence of molecular bands, synthetic flux absorption and emission thermal spectra in clear and cloudy planetary atmospheres were computed. Recently, it was proposed that cloud physical parameters can be constrained by a differential analysis of various molecular bands forming at different heights in the atmosphere with respect to the cloud height and extent [18]. For instance, water vapor bands at 1.09 μm and 1.9 μm show noticeably different sensitivity to particle size and cloud extent and position at intermediate depths in the atmosphere. This is a sensitive spectral diagnostics of clouds.

Polarized scattering in molecular bands was observed in the solar atmosphere and solar system planets (e.g., [17, 20]). To model this polarization we employ the radiative transfer theory described in Sect. 1 with the line scattering coefficient strongly dependent on wavelength (within line profiles), line polarizability and magnetic field (if included, via the Hanle effect) [17, 21]. The first order radiative transfer effect leads to an apparent correlation of line scattering with absorption. This effect increases the contrast of detection of weak signals in distant planets. For example, model spectra from [26] for the Earth atmosphere (Fig. 4, right panels) show polarization in molecular oxygen and water vapour bands in red wavelengths. However, because of the line-dependent polarizability and magnetic sensitivity, line polarization does not in general correlate with line absorption,

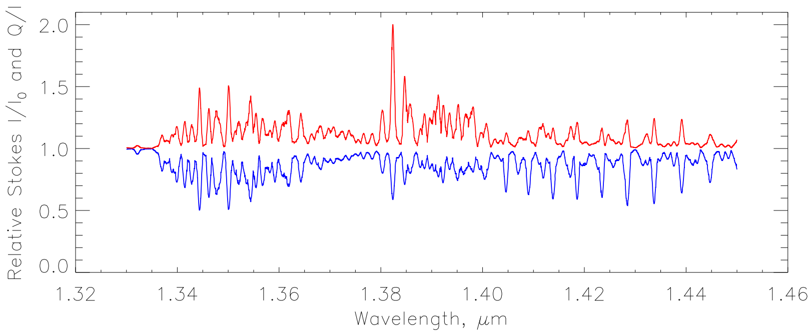

Figure 5: H_2O relative polarization (red) and absorption (blue) spectra plotted, respectively, up and down for clarity, taking into account line polarizability. Note that there is no exact correlation between polarization and absorption.

as is observed in the Second solar spectrum [21]. Neglecting these effects impedes the quantitative interpretation of polarization and the inferred planet parameters. An example taking the polarizability effect into account for about 3500 H_2O lines near 1.4 μm is shown in Fig. 5.

2.4 Biosignatures

A planetary surface visible through an optically thin atmosphere can be searched remotely for spectral and polarized imprints of organisms reflecting and absorbing stellar light. Due to the accessibility and amount of energy provided by the stellar radiation, it seems natural for life to evolve a photosynthetic ability to utilize it as an energy source also on other planets. Thus, flux spectral signatures of biological pigments arising from photosynthesis have been proposed as biosignatures on exoplanets [22, 23]. Moreover, it was recently shown that photosynthetic organisms absorbing visible stellar radiation with the help of various biopigments demonstrate a high degree of linear polarization associated with such absorption bands (see Fig. 4). This effect was also proposed as a sensitive biosignature for high-contrast remote sensing of life [24].

Capturing stellar energy by photosynthetic organisms relies on complex assemblies of biological pigments. While chlorophyll *a* is the primary pigment in cyanobacteria, algae and plants, there are up to 200 accessory and secondary (synthesized) biopigments, including various forms of chlorophyll (*b*, *c* and *d*), carotenoids, anthocyanins, phycobiliproteins, etc. [25]. Various spectral sensitivity of biopigments contribute to their ability to absorb almost all light in the visible range (Fig. 4).

Present and near future observations of Earth-like planets around distant stars cannot resolve the planet surface and image its structures directly. However, uneven distribution of land masses and their various surface properties as on Earth seen from space produce rotational modulation of the reflected light which can be detected and used to constrain the overall surface coverage of various components which can be distinguished with flux and polarization measurements at different wavelengths. To calculate the biosignature effect, we add surface below the atmosphere which implies new lower boundary conditions in Eq. (3). We allow the planetary surface to contain patches due to the presence of photosynthetic organisms, minerals, sands and water and include also scattering and absorption in the planetary atmosphere and clouds. The Earth atmosphere, ocean and clouds are the same as in [26]. Examples are shown in Fig. 4.

The presence of clouds masking the surface dilutes the information on the surface structure and composition. A completely cloudy atmosphere will obviously disguise the presence of biopigments (and everything else) on the planet surface. A small cloud coverage of around 20% will only marginally reduce polarization effect (see [24]). Thus, clouds are the most disturbing factor in detecting surface biosignatures, but weather variability should assist in successful detection if a planet is monitored long enough to reveal long-lived features on the surface.

The effect of the water ocean is also interesting [24]. The optical thickness of the ocean is basically infinite, so its surface is dark in most colors except for the blue, where it reflects the blue light scattered in the atmosphere. However, there is a bright glint at the subsolar location, which moves around the globe as the planet rotates. This glint is due to specular reflection and is highly polarized and practically white. Hence, an ocean only, cloud-free planet with an Earth-like atmosphere will appear somewhat blue (due to Rayleigh scattering in the atmosphere) and highly polarized. It seems therefore that the presence of an ocean and optically thin atmosphere is most favourable for remote polarimetric detection of exoplanets and biopigments.

To conclude, we have presented a broad range of interesting examples where spectropolarimetry provides novel insights into physics of exoplanets and life. The theoretical components outlined in this paper have been developed since the 1950s, and they were successfully employed for probing atmospheres of the Earth, Sun, solar system planets, and other stars. It is imperative now to make a full use of these techniques for advancing our understanding of exoplanets and for searching for life in the universe.

Acknowledgments. This work was supported by the European Research Council Advanced Grant HotMol (ERC-2011-AdG 291659). The author was fortunate to have studied at the Saint Petersburg University under the guidance of Prof. V.V. Sobolev and the professors and docents of his Department. The joint work in the group of Prof. Jan Stenflo at ETH Zurich was also a great benefit for this research.

References

1. *V. V. Sobolev*, Transfer of Radiant Energy in the Atmospheres of the Stars and Planets. Moscow: Gostekhizdat, 1956 (in Russian).

2. *S. Chandrasekhar*, Radiative Transfer. New York: Dover, 1960.

3. *D.I. Nagirner*, J. Quant. Spectrosc. Rad. Transf., **183**, 4, 2016.

4. *D.M. Fluri, S.V. Berdyugina*, Astron. Astrophys., **512**, A59, 2010.

5. *J.E. Hansen, L.D. Travis*, Space Sci. Rev., **16**, 527, 1974.

6. *S.V. Berdyugina, S.K. Solanki, C. Frutiger*, Astron. Astrophys., **412**, 513, 2003.

7. *N.M. Kostogryz, S.V. Berdyugina*, Astron. Astrophys., **575**, A89, 2015.

8. *N.M. Kostogryz, I. Milic, S.V. Berdyugina, P.H. Hauschildt*, Astron. Astrophys., **586**, A87, 2016.

9. *N.M. Kostogryz, T.M. Yakobchuk, S.V. Berdyugina*, Astrophys. J., **806**, 97, 2015.

10. *F. Allard, P.H. Hauschildt, D.R. Alexander et al.*, Astrophys. J., **556**, 357, 2001.

11. *S. Witte, C. Helling, P.H. Hauschildt*, Astron. Astrophys., **506**, 1367, 2009.

12. *S.V. Berdyugina, A.V. Berdyugin, D.M. Fluri, V. Piirola*, Astrophys. J. Lett., **673**, L83, 2008.

13. *S.V. Berdyugina, A.V. Berdyugin, D.M. Fluri, V. Piirola*, Astrophys. J. Lett., **728**, L6, 2011.

14. *S.V. Berdyugina*, in Solar Polarization 6. Eds. J.R. Kuhn et al., Astron. Soc. Pacif. Conf. Ser., **437**, 219, 2011.

15. *J.E. Hansen, J.W. Hovenier*, J. Atmos. Sci., **31**, 1137, 1971.

16. *H.C. van de Hulst*, Light Scattering by Small Particles. New York: Wiley, 1957.

17. *S.V. Berdyugina, J.O. Stenflo, A. Gandorfer*, Astron. Astrophys., **388**, 1062, 2002.

18. *N. Afram, S.V. Berdyugina*, Astron. Astrophys., 2016, submitted.

19. *L. Kreidberg, J.L. Bean, J.-M. Désert et al.*, Nature, **505**, 69, 2014.

20. *F. Joos, H.M. Schmid*, Astron. Astrophys., **463**, 1201, 2007.

21. *J.O. Stenflo*, Solar Magnetic Fields. Dordrecht: Kluwer, 1994.

22. *N.Y. Kiang, J. Siefert, Govindjee, R.E. Blankenship*, Astrobiol., **7**, 222, 2007.

23. *N.Y. Kiang, A. Segura, G. Tinetti et al.*, Astrobiol., **7**, 252, 2007.

24. *S.V. Berdyugina, J.R. Kuhn, D.M. Harrington et al.*, Int. J. Astrobiol., **15**, 45, 2016.

25. *G.D. Scholes, G.R. Fleming, A. Olaya-Castro, R. van Grondelle*, Nature Chem., **3**, 763, 2011.

26. *D.M. Stam*, Astron. Astrophys., **482**, 989, 2008.

* The color figures are available online in the Proceedings at *http://www.astro.spbu.ru/sobolev100/*.

On the Localization of Emission Line Region in Mira Stars

O. Belova[1]

E-mail: *whitecanvas05122010@mail.ru*

New evidence is obtained that hydrogen emission lines as well as metallic ones originate below the molecular absorption layers in Mira stars.

The time scale t_c of gas cooling behind a shock front propagating through the stellar atmosphere when the gas temperature tends to its preshock value T_0 equal to 2800–3000 K corresponding to the molecular layers, is calculated as a function of temperature T at the final stage. This calculation shows that the gas does not have sufficient time to be cooled to its preshock state. So, T_0 should be greater than the temperature of the molecular layers.

This result agrees with the spectra of Mira-like stars available in the literature. The emission lines show a complex structure with asymmetric or multi-component profiles because of molecular line absorption.

1 Introduction

Mira-like stars belong to a class of long-period pulsating variables on the Asymptotic Giant Branch stage [1]. They pulsate with the largest visible amplitude greater than 2.5 mag and the longest period of about some hundred days. The Miras have complex spectra including molecular absorption bands (TiO and VO), absorption lines of metals (Ca, Fe, Ti, V), and strong emission lines of hydrogen and some metals (MgI, MgII, FeI, FeII and others). The emission lines are observed during approximately 70 – 80% of time: they appear before the luminosity maximum and disappear after the luminosity minimum.

Gorbatskii [2] suggested a shock wave model (similar to that of Cepheids) to explain the emission lines in the spectra of Mira variables. In solving the problem of the shock wave in Mira's atmosphere, one usually considers the regions in which the radiation is mainly formed. These regions are rapidly cooled on the timescale of less than a day. Less attention was paid to further cooling of the gas to the preshock temperature, but estimating the time required for complete relaxation of the gas may be important.

It is shown below that the radiative cooling rate of the gas declines at low temperatures and the cooling time can exceed a half of the period.

[1] SAI MSU, Russia

V. Grinin et al. (eds) Radiation mechanisms of astrophysical objects. Yerevan: Edit Print, 2017, pp. 163–166.

2 Cooling timescale

Let us consider the process of gas cooling in the final stage when the gas temperature T (electron temperature is nearly equal to temperature of atoms and ions) tends to the preshock value T_{bg} (see [3] for more details).

At this stage the main processes are photorecombination, free-free transitions, electron-collisional excitation. The ionization state is determined by photoprocesses as the contribution of electron-collisional ionization to the electron density at the gas temperature of 5000 K is far less than the contribution of photoprocesses at the photosphere temperature of 3000 K. The energy gain due to photoionization and energy losses due to recombination cancel each other out. Thus, the cooling is determined by electron collisions and bremsstrahlung.

In general terms, the equation for the temperature in the final stage of cooling may be written as follows:

$$\frac{dT}{dt} = \Phi\left(\varphi_{ff}(T), Q_{ex}(T)\right) = \Phi(T), \tag{1}$$

where $\varphi_{ff}(T)$ is the contribution of bremsstrahlung, $Q_{ex}(T)$ is that of collisional excitation.

The right side of Eq. (1), designated by $\Phi(T)$, is a function of temperature T under the conditions of quasi-stationary ionization. Consequently, the cooling timescale can be calculated as the integral

$$t(T_{\text{beg}}, T_{\text{fin}}) = \int\limits_{T_{\text{fin}}}^{T_{\text{beg}}} \frac{dT}{\Phi(T)}, \tag{2}$$

where T_{beg} is the temperature from the interval 4000–5000 K at which the integration begins. The timescale t is determined by the final temperature T_{fin}.

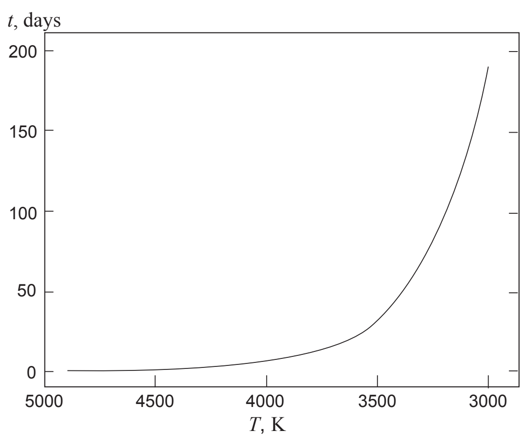

Figure 1: The cooling time as a function of the final temperature T_{fin}.

Some results of our calculations are presented in Fig. 1. As can be seen, the gas is rapidly cooled to a temperature of order of 3700–3500 K, but the rate of cooling significantly decreases for $T_{\rm fin}$ below 3500 K. So, the time of cooling to the temperature equal to 3000 K is approximately 200 days, and that to the temperature of 2800 K is even much more.

It is clear from Table 1 that the cooling time exceeds a half of the period for the majority of Mira variables. Therefore, the gas does not have time to return to the undisturbed value of the temperature. This means that the shock wave passes through the regions under the layer of molecular gas. This fact should be manifested in the spectra of Miras.

Table 1: Typical periods of Mira variables

Star	Period, days	Star	Period, days
o Cet	332	S CrB	360
U Her	406	R Aql	284
S Car	150	RS Vir	354
T Her	165	R Leo	310
T Col	150	R Hya	389

3 Information on emission-line profiles

Let us compare the results of calculations with the observational data. Spectra of Mira variables suitable for analyzing the structure of emission lines were published in [4]–[7].

Gillet et al. [4] studied the Hα profile in the spectra of *o* Cet from the maximum ($\phi \sim -0.05$) to the minimum ($\phi \sim 0.60$). The Hα line has complex structure: there are blue- and red-shifted components. The blue-shifted component has 4 components during about a quarter of period (till $\phi \sim 0.23$): three absorption lines are observed against the emission profile. After the phase $\phi \sim 0.23$, the absorption lines are not separated, but the blue-shifted component has an asymmetric profile. The red-shifted component appears in the spectrum after the phase $\phi \sim 0.14$ and also has an asymmetric shape. These features of the Hα line are associated with the absorption band (γ system) of TiO.

Other papers include emission profiles of Balmer series (Hα–H12) and metal lines (MgI, MgII, FeI, FeII, SiI, MnI) for different Miras. All the profiles demonstrate an asymmetric shape. This is attributed to the effect of scattering by atoms and molecules and absorbing by molecules, mainly TiO.

Thus, emission lines are influenced by atomic and molecular absorption. In this case, the shock wave motion should occur in the layers located below the molecular one. Such a model of Mira's atmosphere is shown in Fig. 2.

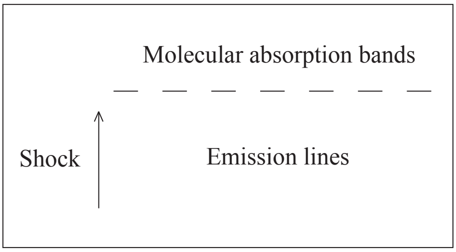

Figure 2: Model of Mira's atmosphere.

4 Conclusion

The problem of cooling of the gas behind the shock front in Mira variables was considered. The cooling time of the gas was calculated as a function of the final temperature and was compared to the typical periods of Mira stars. For most Miras, the cooling time is more than a half of the period, so the gas does not have time to cool down to the unperturbed temperature. In this case, the shock wave should propagate under the layers where molecular absorption bands are formed. This conclusion is confirmed by the available high-resolution optical spectra which show the influence of molecular bands on the emission line profiles.

Acknowledgments. This work was supported by the Russian Foundation for Basic Research (project 15-03-03302) and NSh 9670.2016.2.

References

1. *P.R. Wood*, Mem. Soc. Astron. Ital., **81**, 883, 2010.
2. *V.G. Gorbatskii*, Astron. Zh., **38**, 256, 1961.
3. *O.M. Belova, K.V. Bychkov, G.M. Rudnitskii*, Astron. Rep., **58**, 922, 2014.
4. *M.W. Fox, P.R. Wood, M.A. Dopita*, Astrophys. J., **286**, 337, 1984.
5. *He. Richter, P.R. Wood*, Astron. Astrophys., **369**, 1027, 2001.
6. *D. Gillet, E. Maurice, D. Baade*, Astron. Astrophys., **128**, 384, 1983.
7. *D. Gillet*, Astron. Astrophys., **192**, 206, 1988.

Ionization from Excited Levels as a Cause of Hydrogen Level Non-Stationary Occupation during Radiative Cooling behind a Shock Wave

O.M. Belova[1], K.V. Bychkov[1]

E-mail: *bychkov@sai.msu.ru*

It is shown that for physical conditions typical of late giant star atmospheres, the discrete level occupations are of necessity non-stationary in the case of radiative cooling of hydrogen behind a shock wave. They depend on the whole cooling process as well as on the current values of temperature and electronic density. This fact is due mainly to impact ionization from the excited discrete hydrogen levels.

1 Introduction

Hydrogen contributes significantly to the cooling rate of a shocked gas and defines emission spectrum during flares in stellar atmospheres of the stars whose spectral class is later than A. Both the cooling rate and emission spectra are determined by the relative occupations of discrete levels ν_k and the ionization state x. We assume that N_a and N_p are the atomic and ion hydrogen number densities, respectively, N_k is the number density of hydrogen on the level with the main quantum number k, and N is the total hydrogen number density. So,

$$N = N_a + N_p, \quad x = N_p/N, \quad \nu_k = N_k/N, \quad y_k = N_k/N_1. \tag{1}$$

The discrete level occupations of hydrogen and its ionization state are non-stationary as it follows from our calculations of radiative cooling of shocked gas [1]. This result calls for an explanation. Indeed, transitions between discrete levels are rather quick in stellar atmospheres, and one could expect that both functions of time $\nu_k(t)$ and $x(t)$ are nearly completely determined by the current values of electron temperature $T_e(t)$ and electron density $N_e(t)$, i.e. there is a "quasi-stationary" flow. The Lagrangian coordinate t is the time passed from the beginning of the process, i.e. since the moment when the gas element passed the shock front.

Let us consider a simple model of the two-level atom where the level occupations are controlled by electron impact and spontaneous radiative

[1] SAI MSU, Russia

V. Grinin et al. (eds) Radiation mechanisms of astrophysical objects. Yerevan: Edit Print, 2017, pp. 167–172.

transitions. The occupation y_2 of the excited level is described by the simple formula

$$y_2(t) = y_{2\infty} - (y_{2\infty} - y_{20})\, e^{-\lambda t}, \tag{2}$$

where $y_{20} = y_2(0)$ and $y_{2\infty}$ is the steady state value. The parameter λ is the inverse e-folding time which is expressed through the interaction rates as follows:

$$\lambda = A^*_{21} + Q_{21} + Q_{12}, \tag{3}$$

where Q_{ij} is the excitation $(i<j)$ or deexcitation $(i>j)$ rate, A^*_{21} is spontaneous emission probability. The value of $1/\lambda$ is rather large compared with the temperature evolution time scale. So, if the set of processes is restricted only by the transitions between the discrete levels, we could obtain "quasi-stationary" values of ν_k. However, electron impact ionization from the excited levels changes the time scale. It tends to establish the stationary ionization and occupation states simultaneously, and as a result the whole process is slowed down. The influence of ionization can be demonstrated by the analytical solution of a simple two-level system.

2 Analytical solution

Let us write the kinetic equations for a two-level atom taking into account transitions between discrete levels and ionization by electron impact. All the coefficients are suggested to be constant, and Q_{12} is used for impact excitation rate, R_{21} for deactivation rate (radiative and impact), and Q_{ic} for impact ionization from levels $i = 1, 2$. Recombination is not included, and hence both ν_1 and ν_2 tend to zero. The equations describing evolution of the level occupations are as follows:

$$\frac{d\nu_1}{dt} = -(Q_{12} + Q_{1c})\nu_1 + R_{21}\nu_2, \tag{4}$$

$$\frac{d\nu_2}{dt} = -(R_{21} + Q_{2c})\nu_2 + Q_{12}\nu_1. \tag{5}$$

The characteristic equation has two roots

$$\lambda_1 = \frac{s+d}{2}, \quad \lambda_2 = \frac{s-d}{2}, \tag{6}$$

where

$$s = Q_{12} + R_{21} + Q_{1c} + Q_{2c}, \tag{7}$$

$$p = Q_1\, R_{21} + Q_2\, (Q_{12} + Q_{1c}), \tag{8}$$

$$d = \sqrt{s^2 - 4p}\,. \tag{9}$$

With chosen initial conditions

$$\nu_{10} = 1, \quad \nu_{20} = 0, \tag{10}$$

the solution is

$$\nu_1 = \frac{Q_{12} + Q_{1c} - \lambda_2}{\lambda_1 - \lambda_2} e^{-\lambda_1 t} + \frac{\lambda_1 - Q_{12} - Q_{1c}}{\lambda_1 - \lambda_2} e^{-\lambda_2 t}, \tag{11}$$

$$\nu_2 = \frac{Q_{12}}{\lambda_1 - \lambda_2} \left(e^{-\lambda_2 t} - e^{-\lambda_1 t} \right). \tag{12}$$

The excitation coefficient Q_{12} and the ionization coefficient from the ground level Q_{1c} are often small compared to the deactivation rate

$$Q_{12} + Q_{1c} \ll R_{21}. \tag{13}$$

Then Eqs. (6) for λ_1 and λ_2 are simplified

$$\lambda_1 \approx s, \quad \lambda_2 \approx m/s, \tag{14}$$

where

$$m = Q_1 (Q_2 + R_{21}) + Q_{12} Q_2. \tag{15}$$

Note that the simplified value of λ_1 is near to λ from Eq. (2). They coincide if we substitute $A^*_{21}+Q_{21}$ instead of R_{21} and omit Q_{1c} and Q_{2c} in the expression for s. The inequality $m \ll s$ follows from Eq. (13), and hence

$$\lambda_2 \ll \lambda_1. \tag{16}$$

So, ionization changes significantly the evolution of excited level occupation in comparison with Eq. (2). Now the whole process develops in two stages. Occupation changes quickly at the first stage on the "short" time scale which is defined by deactivation. The final value of occupation establishes on the "long" time scale $1/\lambda_2$ in which ionization from the excited level plays the important role.

Equation (12) contains all these features. The occupation ν_2 quickly grows on the time scale $1/\lambda_1$ due to diminishing the negative term $e^{-\lambda_1 t}$ in Eq. (12), reaches a maximum at the moment t_m such as

$$t_m = \frac{\ln(\lambda_1/\lambda_2)}{\lambda_1 - \lambda_2}, \tag{17}$$

and drops exponentially after the maximum on the "long" scale $1/\lambda_2$. All these features are drawn on Fig. 1.

3 Radiative cooling behind a shock front

Here we consider numerical results for a multilevel system to which the analytical approach is not applicable. Let the unperturbed equilibrium gas pass through the shock front at the velocity 50 $\mathrm{km\,s^{-1}}$, with the temperature T_0 and number density N_0 being typical of Mira Ceti atmospheres: $T_0 = 3000\,\mathrm{K}$ and $N_0 = 10^{12}\ \mathrm{cm^{-3}}$.

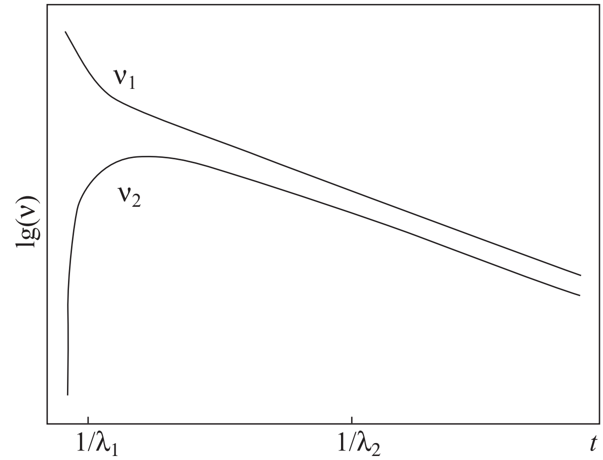

Figure 1: Analytical solution for a two-level system.

We have written the differential equations for the problem in [1]. Here we rewrite the equation describing the occupations of excited hydrogen levels as follows:

$$\begin{aligned}\frac{d\nu_k}{dt} = &-\left[q_{kc}N_e + \sum_{k>i}\left(A^*_{ki} + q_{ki}N_e\right) + \sum_{k<i} q_{ki}N_e\right]\nu_k \\ &+ (r_k + \gamma_k N_e)N_e x + \sum_{i>k}\left(A^*_{ik} + q_{ik}N_e\right)\nu_i + N_e \sum_{k<i} q_{ik}\nu_i,\end{aligned} \tag{18}$$

where q_{ki} are the coefficients of electron impact transitions between discrete levels k and i for excitation ($k<i$) and deactivation ($k>i$), r_k and γ_k are for radiative and triple recombination on the level k, respectively, x is the proton relative concentration, A^*_{ij} designs the spontaneous radiative transition probability taking into account the line scattering

$$A^*_{ij} = A_{ij}/\zeta_{ij}, \tag{19}$$

with ζ_{ij} being the scattering number before a quantum leaves the cooling gas. For ν_k and x, we have

$$\sum_{k=1}^{K} \nu_k + x = 1. \tag{20}$$

The upper limit K is the main quantum number of the highest level which is realized under the given conditions. We obtain $K = 25$ using Inglis–Teller equation.

Some results of calculations of non-stationary cooling of the shocked gas are drawn on Fig. 2 as functions of time $T_e(t)$ and $\nu_5(t)$. Note that T_e can rise when the gas cools behind the shock. Time t on the bottom axis is measured in seconds. A fragment of gas evolution during about 0.007 s is selected at about 3 seconds

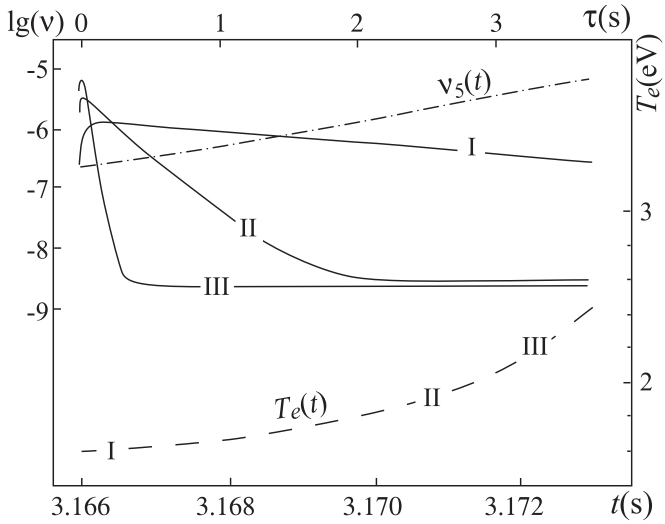

Figure 2: Electron temperature T_e (dashed) and non-stationary occupation ν_5 (dash-dot) evolution of the shocked gas behind a shock: the lower horizontal axis is the time (in sec) elapsed from the shock passed, the right vertical axis is T_e in eV, the left one is occupation in logarithmic scale, the upper horizontal axis is τ (in sec), solid lines I, II and III describe evolution $\nu_5^{(\mathrm{qs})}(\tau)$ as a solution of Eq. (18) for the temperature values I, II, and III.

after passing the shock. The lower dashed line describes the function $T_e(t)$, while $\nu_5(t)$ is drawn by the upper dash-dot line in the logarithmic scale. The right vertical axis is the electron temperature measured in electron-volts, and the left one is decimal logarithm of the occupation ν_5.

Three solid curves (I, II, and III) are the solutions of the system (17) for a given value of $T_e(t)$. These curves show "quasi-stationary" functions $\nu_5^{(\mathrm{qs})}(T_e(t), \tau)$ with the initial conditions $\nu_k(\tau = 0) = \nu_k(t)$, where $T_e(t)$ is a parameter and the independent variable τ is the time elapsed from the moment t. The values of τ are given on the upper horizontal axis. Three values of the parameter $T_e(t)$, chosen and noted by I, II, and III on the lower dashed curve, are as follows: $T_e^{(\mathrm{I})} = 1.6\,\mathrm{eV}$, $T_e^{(\mathrm{II})} = 1.9\,\mathrm{eV}$, $T_e^{(\mathrm{III})} = 2.2\,\mathrm{eV}$.

The functions $\nu_5^{(\mathrm{qs})}(T_e(t), \tau)$ make sure that $\nu_5(t)$ corresponds to a properly non-stationary process. All solid curves are similar to the analytical solution: a fast rise from the initial value followed by slow transition to a maximum and after that to a constant value $\nu_\infty(T_e(t))$.

Comparing the three solid curves with the lower dashed line, we see that the time for any $\nu_5^{(\mathrm{qs})}(T_e(t), \tau)$ to reach its steady state value $\nu_\infty(T_e(t))$ is longer than the time needed for T_e to grow up. This is the first evidence for non-stationary cooling process. And comparing the solid lines with the dash-dot one, we obtain the second evidence. The numerical difference between $\nu_5(t)$ and the corresponding steady state values are very large and can reach orders of magnitude (one for the curve I, and 3–4 orders for II and III).

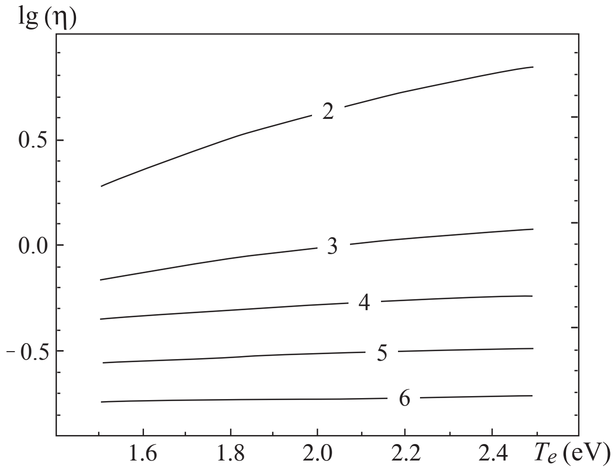

Figure 3: Ratio $q_{kc}/q_{k,k-1}$ vs T_e.

4 Ionization and deexcitation rates

We see that ionization from the excited states is an important factor which determines non-stationary character of shocked gas cooling. Its efficiency depends on the ratio

$$\eta_k = \frac{q_{kc}}{q_{k,k-1}}. \tag{21}$$

The greater η_k, the more effective the influence of ionization is. This relation is drawn on Fig. 3 for the first five excited levels of hydrogen atom as a function of the electron temperature T_e. The temperature range $1.5\,\mathrm{eV} < T_e < 2.5\,\mathrm{eV}$ is typical of a flow behind the front in a cold star atmosphere. The electron impact coefficients q_{kc} and $q_{k,k-1}$ were calculated from the Johnson formulas [2]. As follows from Fig. 3, ionization prevails in the case of the second level ($n = 2$), and the value of η_k remains sufficient up to $n = 6$.

So, electron impact ionization from the excited hydrogen levels ($n \leqslant 6$) is the cause of non-stationary cooling of the shocked gas.

Acknowledgments. This work was supported by the Russian Foundation for Basic Research (project 15-03-03302) and NSh 9670.2016.2.

References

1. *O.M. Belova, K.V. Bychkov, E.S. Morchenko, B.A. Nizamov*, Astron. Rep., **58**, 650, 2014.

2. *L.C. Johnson*, Astrophys. J., **174**, 227, 1972.

Variability of [OI] 6300 Å and [OI] 6363 Å Emission in HD 200775

A.P. Bisyarina[1], A.M. Sobolev[1], S.Yu. Gorda[1]

E-mail: *bisyarina_nastya@mail.ru*

Variability of the emission in [OI] 6300 Å and [OI] 6363 Å lines from Herbig Be binary star HD 200775 is reported for the first time. The system has the common disk observed in IR-emission and an accretion disk around the primary component which is probably formed due to accretion of the common disk material. The orbital period of the binary system is about 3.7 years. The [OI] line profiles from the newly-obtained spectral data and the archival ones, derived during the last 20 years or so, were examined. The major part of the data was obtained with the 1.2 m telescope at Kourovka Astron. Obs., Ural Federal Univ. Similarity of the line profiles obtained at the same orbital phases in different epochs and with different instruments was found. So, the variability of [OI] line emission is related to the binarity of the system.

1 Context

HD 200775 (V380 Cep, MWC 361) is a Herbig Be binary star with the orbital period of about 3.7 years. Mid-infrared interferometric observations of the binary orbit [1] and a number of spectroscopic works [1]–[7] were performed to estimate the orbital parameters. Periodic maximum activity phases related to the binarity were recognized in the spectra of the star [2]. This activity is characterized by an increase in the equivalent width of the Hα line formed in the material associated with the primary component.

The authors of [8, 9] observed diffuse IR-emission from the system and suggested that it was originated from the common circumbinary disk. In [8, 6] the presence of an accretion disk close to the primary (more massive) component of the system was pointed out. This disk is probably formed by the material accretion from the common disk onto the primary component. There is no evidence of any disk material near the secondary component.

Forbidden OI line emission in Herbig Ae/Be and T Tauri stars is often observed as a blue-shifted high-velocity component originated from an outflow and a low-velocity component (e.g., [10, 11]). The origin of the latter is unclear, it might be formed on the disk surface or in the slow disk wind. A review of [OI] line emission in 49 Herbig Ae/Be stars, including HD 200775, has been performed

[1] Kourovka Astronomical Observatory of the Ural Federal University, Russia

V. Grinin et al. (eds) Radiation mechanisms of astrophysical objects. Yerevan: Edit Print, 2017, pp. 173–176.

in [12]. However, variability of [OI] lines in spectra of this binary star is for the first time reported in this paper.

2 Observational data

Our data were obtained from May 2, 2012 to April 2, 2015 using a high-resolution spectrograph mounted at the 1.2 m telescope of the Kourovka Astronomical Observatory of the Ural Federal University. The operating wavelength range was 4000–7800 Å, an effective exposure was 1 hour (each image is a median average of three 20-min CCD images). One spectrum was obtained in 2013 with NES spectrograph of the Special Astrophysical Observatory of Russian Academy of Science (SAO RAS). We also used archival spectral data obtained from 1994 till 2011 with ELODIE and SOPHIE spectrometers of Observatoire de Haute-Provence, the ESPaDOnS spectrometer from Canadian-France Hawaii Telescope, as well as NES data from the SAO RAS archive.

3 Results

In the spectra of HD 200775 we see a broad low-velocity component of the [OI] line (Fig. 1). There is no evidence of the high-velocity one. Unfortunately, the wavelength region around the [OI] 6300 Å line includes a number of telluric lines and narrow atmospheric oxygen emission. But these lines only arise at well-defined wavelengths, while at the other wavelengths variations in stellar emission still can be seen. The most significant changes (except for atmospheric components) occur near the values of −65, 30 and 55 km/s.

We have also considered emission in the [OI] 6363 Å line (Fig. 1, right panel). This line is about twice less intensive than the [OI] 6300 Å one. So, the signal-to-noise ratio of many of our spectra did not allow us to examine the line. On the other hand, the spectral region near this line is free from telluric lines. Thus,

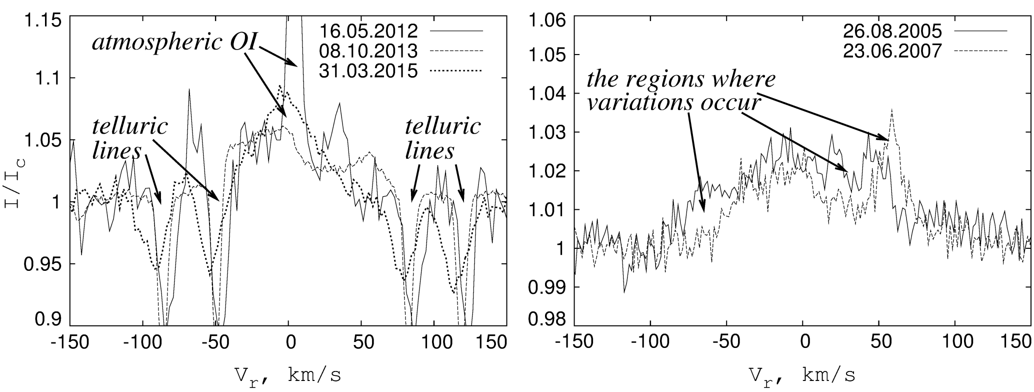

Figure 1: [OI] 6300 Å (left panel) and [OI] 6363 Å (right panel) lines profiles in HD 200775 at different epochs.

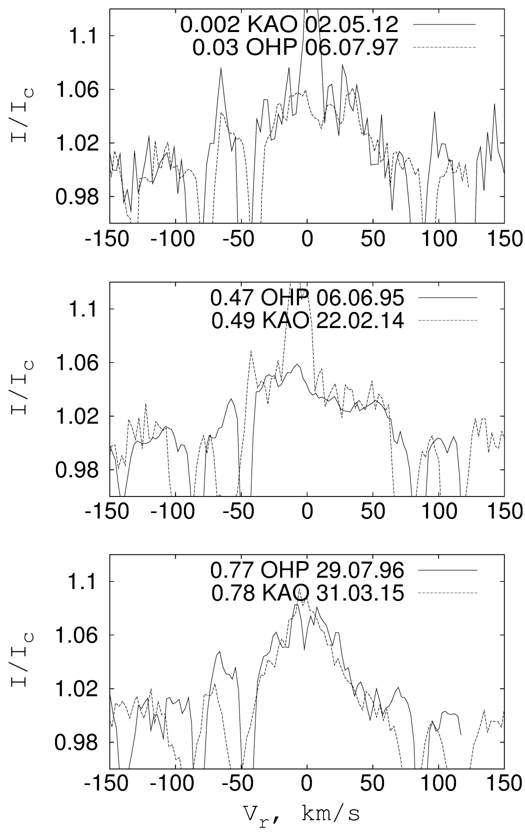

Figure 2: Comparison of [OI] 6300 Å line profiles. The line profiles are different on different panels but similar inside the panels for close orbital phases.

we can verify our results obtained for the [OI] 6300 Å line. We found that the variations in this line profile occur nearly at the same velocity values as for the [OI] 6300 Å line.

Estimating the orbital period, made on the basis of the data covering 20 years in our previous work [7], allowed us to use very accurate values of orbital phases. As a result, we noticed that the [OI] 6300 Å line profiles in the spectra, obtained with different instruments and at different observational epochs but at the same orbital phases, are similar (Fig. 2). This means that the variability of [OI] emission is related to the binarity of the system.

4 Summary

Variability of the [OI] emission in the spectra of HD 200775 is reported for the first time. Significant changes of the lines profiles appear in three components – near −65, 30 and 55 km/s for both [OI] 6300 Å and [OI] 6363 Å lines. They were examined on the basis of 20 years data including new and archival high-resolution spectra. We found that the line profiles in spectra obtained in different epochs but at the same orbital phases are similar. Thus, we showed that the variations are related to the binarity of the system. The mechanism of the [OI] line variability in HD 200775 is still an open question.

Acknowledgments. The work was supported by the Russian Science Foundation, grant No. 15-12-10017.

References

1. *J.D. Monnier, J.-P. Berger, R. Millan-Gabe et al.*, Astrophys. J., **647**, 444, 2006.
2. *A.S. Miroshnichenko, C.L. Mulliss, K.S. Bjorkman et al.*, Publ. Astron. Soc. Pacif., **110**, 883, 1998.
3. *N.Z. Ismailov*, Astron. Rep., **47**, 206, 2003.
4. *M.A. Pogodin, A.S. Miroshnichenko, A.E. Tarasov et al.*, Astron. Astrophys., **417**, 715, 2004.
5. *E. Alecian, C. Catala, G.A. Wade et al.*, Mon. Not. Roy. Astron. Soc., **385**, 391, 2008.
6. *M. Benisty, K. Perraut, D. Mourard et al.*, Astron. Astrophys., **555**, A113, 2013.
7. *A.P. Bisyarina, A.M. Sobolev, S.Yu. Gorda*, Astron. Bull., **70**, 243, 2015.
8. *J.D. Monnier, P.G. Tuthill, M. Ireland et al.*, Astrophys. J., **700**, 491, 2009.
9. *Y.Z. Okamoto, H. Kataza, M. Honda et al.*, Astrophys. J., **706**, 665, 2009.
10. *J. Kwan, E. Tademaru*, Astrophys. J. Lett., **332**, L41, 1988.
11. *G.A. Hirth, R. Mundt, J. Solf*, Astron. Astrophys., **285**, 929, 1994.
12. *B. Acke, M.E. van den Ancker, C.P. Dullemond*, Astron. Astrophys., **436**, 209, 2005.

Non-Stationary Processes in Atmospheres of Early-Type Stars: Influence on Forbidden to Intercombination Ratio f/i

V.V. Dushin[1], A.F. Kholtygin[1]

E-mail: *v.dushin@spbu.ru*

We report the results of non-stationary level population modeling of highly ionized atoms in the atmospheres of early-type stars. We studied the influence of the fast heating and cooling processes on the ratio of forbidden to intercombination line intensities $R = f/i$ for He-like ions (CV, NVI, OVII, etc.) in X-ray spectra.

It is shown that the instantaneous ratio R_m for the non-stationary plasma varies by up to 4 orders of magnitude on short time scales (milliseconds) in comparison with the value for the stationary plasma. In the same time the value of R_a averaged on long time scales (hours and minutes) varies by up to 20%. Using the ratio R calculated in the case the stationary plasma for the non-stationary plasma can lead to an overestimation of the plasma electron density by up to 1–2 orders of magnitude.

1 Introduction

The density diagnostics of the X-ray emitted plasma of the early-type stars based on the forbidden-to-intercombination line ratio R showed that this ratio is much lower than that predicted for the homogeneous non-stationary plasma (e.g., [1]). This could be explained as follows:

- The stellar UV-radiation excites electrons in the upper level 1s2s $^3\mathrm{S}_1$ of the forbidden line f and populates the upper level 1s2p $^3\mathrm{P}_{1,2}$ of the intercombination line i, which weakens the line f and strengthens the line i.
- Bound electrons are excited from the upper level of the line f by free electrons, which decreases the line f. This happens if the X-ray radiation originates from the dense clouds in stellar atmospheres.

In this paper we outline an alternative hypothesis.

2 Processes in non-stationary plasma

We suppose that the level population in the stellar atmospheres can become non-stationary.

[1] St. Petersburg State University, Russia

V. Grinin et al. (eds) Radiation mechanisms of astrophysical objects. Yerevan: Edit Print, 2017, pp. 177–180.

Non-stationarity could be caused by collisions of the plasma flows in the region on the stellar magnetic equator or by nano-flares in the stellar atmosphere similarly to the solar ones.

The non-stationary level population can be described by the following equation:

$$\frac{dx_i}{dt} = n_e \sum_{j \neq i}^{N} x_j q_{ji} + \sum_{j=i+1}^{N} x_j A_{ji} - x_i \left(\sum_{j=1}^{i-1} A_{ij} + n_e \sum_{j \neq i}^{N} q_{ij} \right). \tag{1}$$

Here x_i is the relative population of the i-th level, N is the number of levels considered, n_e is the electron density, q_{ji} is the excitation/deexcitation rate from the level j to the level i, A_{ij} is the corresponding Einstein A-value. In our models we used $N = 50$ levels, which was enough for a precise modeling.

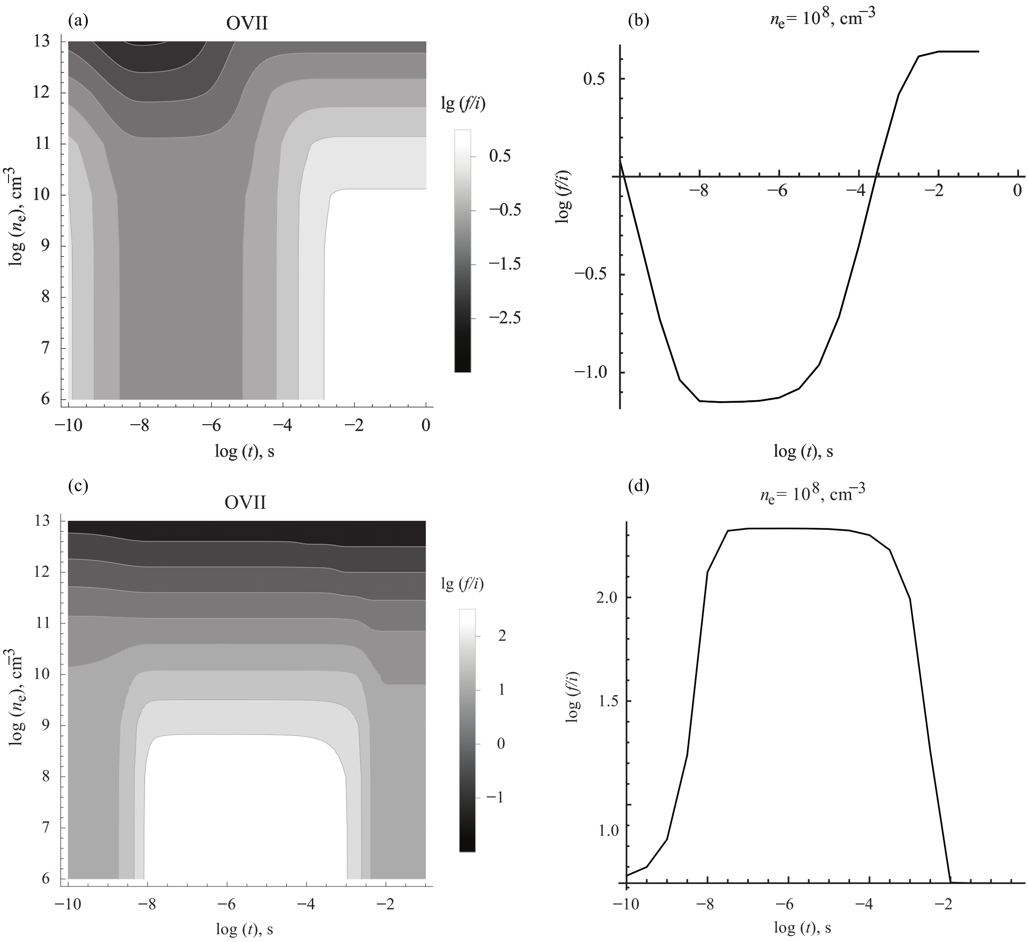

Figure 1: *Panel a*: Dependence of the ratio R_m on time and electron number density for OVII in the model for rapidly heated plasma. At $t = 0$, the plasma instantaneously heats from $T_\mathrm{e} = 10^6$ K to $T_\mathrm{e} = 10^7$ K, after the heating the temperature remains constant. *Panel b*: the same but for $n_\mathrm{e} = 10^8$ cm^{-3}. *Panels c, d*: the same as the upper row, but for rapid cooling from $T_\mathrm{e} = 10^7$ K to $T_\mathrm{e} = 10^6$ K.

Table 1: The parameters of the models: T_c is the plasma temperature in the "cool" state, t_c is the time of cooling, R_c is the stationary line ratio for T_c, the similar parameters for plasma heating are indexed with "h"

Model	T_c, K	t_c, s	T_h, K	t_h, s	R_c	R_h
A	5×10^5	3×10^{-2}	10^8	10^{-5}	9×10^{-3}	4×10^{-2}
B	5×10^5	10^{-5}	10^8	10^{-5}	3	2.75
C	5×10^5	3×10^{-2}	10^8	10^{-5}	9×10^{-4}	4×10^{-3}
D	5×10^5	10^{-3}	10^7	3×10^{-3}	7.5×10^{-1}	1.34
E	5×10^5	3×10^{-2}	10^8	10^{-5}	4.44	2.94
F	5×10^5	3×10^{-2}	10^8	10^{-5}	4.26	2.93
G	5×10^5	3×10^{-3}	10^7	2×10^{-3}	1.78	2.94
H	5×10^5	10^1	10^7	10^{-1}	5.61	8.25
I	5×10^5	10^{-3}	10^8	10^{-5}	2.98	2.75

Table 2: The results of the modeling, where n_e is the input model electron density, R_a is the averaged line ratio f/i, $\bar{n}_e$ is the electron density derived from R_a, when supposing the stationarity of the plasma

Model	Ion	n_e, cm^{-3}	R_a	$\bar{n}_e$, cm^{-3}	$\lg(n_e/\bar{n}_e)$
A	OVII	10^{13}	10^{-2}	8×10^{12}	0.1
B	OVII	10^{10}	–	–	–
C	OVII	10^{14}	2×10^{-3}	5×10^{13}	0.3
D	OVII	10^{11}	1.18	5×10^{10}	0.3
E	OVII	10^8	3.48	6×10^9	−1.8
F	OVII	10^9	3.35	6×10^9	−0.8
G	NVI	10^{10}	2.12	8×10^9	0.1
H	CV	10^9	6.24	8×10^8	0.1
I	OVII	10^{10}	2.93	–	–

3 Modeling and discussion

We used both a modified APEC [2] code and an additional code written in Mathematica to solve equation (1). We calculated the ratio R for various conditions of the plasma heating and cooling.

It can be seen that in the case of fast heating of low density plasma the ratio R decreases dramatically for a short time (see the "valley" in Fig. 1b). A similar behavior holds for the case of cooling: we can see the dramatic increase of the ratio R in the first second (the "plateau" in Fig. 1d). For stationary case, R holds in the interval 1–10.

Unfortunately, such fast processes could not be observed, since the exposure time of X-ray satellites is of the order of 10^4 s and above. That is why we studied the influence of non-stationary processes on the average f/i-ratio (R_a). The model parameters are presented in Table 1, results of the modeling are summarized in Table 2. It can be seen that the models E and F show significant difference between R_a and R_c and R_h. It means that using the ratios R for the stationary plasma leads to the overestimation of the n_e derived from observations.

The parameters of heating and cooling which are given in the captions to Fig. 1 are typical of solar nano-flares or similar events in stellar atmospheres.

4 Conclusion

We showed that non-stationary processes could affect on the instantaneous forbidden-to-intercombination ratio R_m which increases (for fast cooling) or decreases (for fast heating) by up to 1–3 orders of magnitude during the first second. These processes could also strongly change the averaged ratio R_a by decreasing it by up to 20%. In this case one can incorrectly estimate the plasma electron density (errors can be of up to 2 orders of magnitude), when supposing the stationary level population in the plasma.

Acknowledgments. Some of our results were previously published in [3]. The authors acknowledge St. Petersburg State University for research grant 6.38.18.2014.

References

1. *W.L. Waldron, J.P. Cassinelli*, Astrophys. J. Lett., **548**, L45, 2001.
2. *R.K. Smith, N.S. Brickhouse, D.A. Liedahl, J.C. Raymond*, Astrophys. J. Lett., **556**, L91, 2001.
3. *V. V. Dushin, A.F. Kholtygin*, Astron. Rep., **59**, 709, 2015.

Properties of Emission of Coronal Holes on the Sun according to Observations in Radio Range

O.A. Golubchina[1]

E-mail: *golubchina_olga@mail.ru*

This paper is a brief review devoted to the investigation of coronal holes (CHs) on the Sun. The special attention is paid to CHs research in the millimeter and centimeter wavelength ranges. Observations in the millimeter range and from satellites in ultraviolet and soft X-ray ranges, as well as observations of Solar eclipse on March 29, 2006 at centimeter waves with the radio telescope RATAN-600 have yielded new data for understanding of the physical nature of coronal holes on the Sun.

1 Statement of the problem

Coronal holes (CHs) are areas of low temperature and density at the surface of the Sun. These areas are unipolar, with an open configuration of the magnetic field. Polar coronal holes are always visible on the poles of the Sun during the periods of a minimum solar activity as the rotary directed dipole component of the magnetic field prevails at this phase. During the periods of an increased solar activity, CH can exist at any latitude of the Sun. A CH is formed by random convective motions of the open magnetic field lines in the photosphere and reconnection of lines of the open magnetic field with the closed coronal lines. Lines of the open magnetic field in CH expand super-radially. Carrying out a stream of the charged particles from CH and low rate of emergence of new magnetic flux [1] can explain low density of particles in CH on the Sun. For the first time, observations of a CH above the solar limb were performed by Waldmeier [2] in a green line (5303 Å) with coronograph of the Zurich observatory. CHs above the limb were observed as the least intensive and long-living formations. A progress in studying CHs started in 1973–1974 with spacecraft observations in the ultra-violet (EUV) and soft X-ray (3–60 Å) ranges. The CH areas are seen in EUV and soft X-ray ranges as very dark places on the Sun because of low density and temperature in CH. CHs are identified with the areas of increased brightness in the line HeI 10830 Å as they possess the lowest absorption in the line [3, 4]. Therefore, radiation in this line often serves as an indicator of a CH. CHs represent a huge interest not only as a phenomenon in the physics of the Sun, but also as the source of quasi-stationary high-speed streams of solar plasma – the solar wind which extends to

[1] St. Petersburg Branch of Special Astrophysical Observatory, Russia

V. Grinin et al. (eds) Radiation mechanisms of astrophysical objects. Yerevan: Edit Print, 2017, pp. 181–185.

the limits of the Solar System. The high-speed solar wind ($V = 700 - 800$ km/s) is the source of recurrent geomagnetic disturbances. By means of observations of solar eclipses in white light and from satellites in the ultra-violet (EUV) and X-ray ranges, a precise correlation between the high-speed solar wind and polar CHs, large low-latitude CHs was established [3, 5]. Magnitosphere protects the Earth from dangerous influence of the solar wind. It is obvious that the study of CHs is very important for human survival not only on the Earth, but also in space.

2 Observations of polar CHs at mm-wavelengths

Large coronal holes on the Sun emerge within approximately 7 years near a minimum of solar activity and are absent within 1–2 years near to a maximum [6]. Observations of polar CHs were first made in CRAO at the wavelengths of 8.2 and 13.5 mm with the radio telescope RT-22 (1974–1977) and in Australia (CSIRO) at 3.5 mm with the 4 m paraboloid (1977) [7]. Polar CHs are investigated at the solar latitude φ of up to 80°. Observations are impossible in the radio range if $\varphi > 80°$ as there is a steep temperature gradient near to the limb of the Sun. It was shown that the polar CHs are areas of the increased intensity of radio emission at mm-wavelengths. (If T is the excess of temperature over the temperature of the quiet Sun, $T = 1500$ K at $\lambda = 8.2$ mm, and $T = 2200$ K at $\lambda = 13.5$ mm.) Similar observations made in Japan on a radio telescope with the diameter $d = 45$ m have shown a considerably smaller temperature excess of $T =$ (240–560) K at $\lambda = 8.3$ mm. The temperature excess was not revealed in a polar area of the Sun at the wavelength of 3.1 mm [9]. More careful researches of polar CHs were performed in Finland (Metsähovi Radio Observatory) by means of a radio telescope of 14 m in diameter at 3.4, 3.5, and 8 mm with attraction of observations in the ultraviolet (EUV SOHO/EIT) and soft-X-ray (0.25–4) keV ranges and in white light. The polar areas at up to 70° of the solar latitude were studied with this radio telescope. Observations of polar CHs in Metsähovi Radio Observatory revealed that at the frequency of 87 GHz ($\lambda = 3.5$ mm) polar areas can demonstrate enhanced brightness as well as depressions. Sometimes a polar CH is visible as a radio depression with local brightening inside it [10, 11]. Comparisons of the obtained radio maps with the images of the Sun in the EUV and soft X-ray ranges allowed establishing the fact that the brightness increase in polar area at the mm-wavelengths correlates with polar plumes, diffuse EUV emission and bright points inside the CH. An increase of intensity of the radio emission in the mm-range coincides with the dark surfaces on images in the EUV and soft X-ray ranges (SOHO/EIT). However, from these observations it was impossible to determine, whether the increase of intensity of radiation from polar CH at the mm wavelengths is due to a thermal or non-thermal mechanism. Note that inside of the areas of an increased radio emission of polar CHs, there are medium and strong magnetic fields.

3 Emission of polar and low-latitude CHs in cm-range

CHs are areas of low radio emission at cm-wavelengths and are always identified with the most dark sites (except for floccules) on the surface of the Sun in EUV and soft X-ray emission. A depression of intensity of radio emission in CHs was revealed by 19 observations (1975–1987) on various radio telescopes in the range 1.38–21.4 cm. The average contrast of the CH radiation in relation to the level of the quiet Sun is 0.9. Radiation in the helium line HeI 10830 Å is weakly absorbed in CHs. Therefore, at cm-wavelengths CHs correlate with the bright areas on the Sun observed in this helium line. The intensity of magnetic fields in CHs is equal to 1–3 G. Observations of CH above the North Pole of the Sun on March 29, 2006 at cm-wavelengths (1.03, 1.38, 2.7, 6.2, 13, 30.7 cm) have been made on the northeast sector of the RATAN-600 by the method of "relay race" [12] during the maximum phase (0.998) of the solar eclipse. A center of the directional pattern (DP) was shifted at $h = +15$ arc min to investigate the radio emission above the North Pole of the Sun. The observation of the solar eclipse at RATAN-600 allowed us to determine physical characteristics of the CH above the North Pole of the Sun at the minimum of solar activity. The distribution of brightness temperature and electron density was reliably determined in the Northern polar CH on the Sun at the distances from 1 to 2 solar radii from the observations at $\lambda = 1.03$, 1.38, 2.7, 6.2, 6.3, 13, 30.7 cm and and their computer simulation [13]. As a first approximation, the electron density can be calculated at the wavelengths of 1.03 and 1.38 cm. It was established that the distribution of the electron density from the solar limb up to $2R_c$, where R_c is the radius of the optical disk of the Sun, is close to the distribution obtained in white light at the minimum of solar activity [13, 18]. As a consequence, a question arise, whether the physical characteristics of a large low-latitude CH and a polar CH are identical. Results of observations of the quiet Sun and low-latitude CHs on the background of the quiet Sun which were earlier obtained with RATAN-600 for a minimum of solar activity [8] have been utilized to answer this question. The coincidence of brightness temperatures of the quiet Sun with brightness temperatures found from the observations of the polar CH during the solar eclipse at $\lambda = 1.03$, 1.38, 2.7 cm testifies that a CH above the North Pole of the Sun is not visible at such short wavelengths. Low-latitude coronal holes on the background of the quiet Sun are not visible at short wavelengths either. Sharply dropping brightness temperature is revealed from the observational data for the solar eclipse at $\lambda = 6.2$, 13, and 30.7 cm over the range of distances (1.005–1.03) R_c, which testifies to a detection of a CH at these wavelengths. Investigation of low-latitude CHs also confirmed the detection of a CH if the wavelengths were greater than 4 cm. The simulated brightness temperatures of the low-latitude CHs were compared with the temperatures at the nearest points to the limb of the Sun which were obtained from the observations of the solar eclipse. It revealed their coincidence on close wavelengths. The coincidence of the above-mentioned properties of cm-radio emission of the low-latitude CHs and CHs above the North Pole of the Sun testifies to the same nature of large CHs regardless of the place of their location on the Sun.

4 Radio emission of CHs in meter and decameter ranges

CH researches were conducted on interferometers, multi-element radio telescopes and radio heliographs in the meter and decameter ranges ($\lambda = 73 - 970$ cm) during 1974–1989. In the meter range a lowered intensity of radio emission of CHs was detected [14]. These CHs are well correlated with the dark areas on the EUV-images of the Sun. The temperature of CHs was found to be $T = 0.8 \times 10^6$ K, and the average temperature outside of CHs was $T = 1.0 \times 10^6$ K, i.e. the lower intensity of the radio emission of CHs has been detected [14, 15, 16] according to the observations of CHs in the meter range at 3.75 m (80 MHz) and 1.88 m (160 MHz) in 1972. The study of CHs showed both the increased and lowered intensities of radio mission in the decameter range. This is connected with the uncertainty of identification of the observed areas on the Sun because of the influence of strong radio refraction [17].

5 Results

Summarizing, it is possible to briefly formulate the basic characteristics of coronal holes in various wavelength ranges.

CHs in the radio range correlate with the most dark sites on the surface of the Sun observed in the ultra-violet and X-ray (3–60 Å) ranges and with areas of the increased brightness in the line HeI 10830 Å. Polar coronal holes at mm-wavelengths can show both a brightness increase and a depression. In the cm-range of wavelengths CHs are observed as areas of a reduced intensity, starting from the wavelengths of about 4–6 cm. CHs on the surface of the Sun are not visible at short wavelengths of the cm-range. At cm-wavelengths the distribution of electron density in the CHs above the pole of the Sun at the distances from the solar limb up to $2R_c$ is close to that obtained in white light during the epoch of a minimum of solar activity. The temperature characteristics of big CHs in the cm-range do not depend on their location on the Sun. CHs are the areas of a lower intensity in the meter- and dm-ranges. CHs show both increased and lowered intensities of radio emission at decameter wavelengths. This is connected with the uncertainty of identification of the observed area on the Sun because of strong radio refraction.

References

1. *V.I. Abramenko, L.A. Fisk, V.B. Yurchyshyn*, Astrophys. J. Lett., **641**, L65, 2006.
2. *M. Waldmeier*, Z. Astrophys., **38**, 219, 1956.
3. *S.R. Cranmer*, Living Rev. Solar Phys., **6**, 3, 2009.
4. *H. Zirin*, The Solar Atmosphere. Waltham: Blaisdell Publ. Co., 1966.
5. *Y.-M. Wang*, Astrophys. J., **660**, 882, 2007.
6. *K.L. Harvey, F. Recely*, Sol. Phys., **211**, 31, 2002.
7. *A.N. Babin, S.I. Gopasuk, V.A. Efanov et al.*, Izv. Krym. Astrofiz. Obs., **55**, 3, 1976.
8. *V.N. Borovik, M.S. Kurbanov, M.A. Livshits, B.I. Ryabov*, Sov. Astron., **34**, 522, 1990.
9. *T. Kosugi, M. Ishiguro, K. Shibasaki*, Publ. Astron. Soc. Japan, **38**, 1, 1986.
10. *S. Pohjolainen, F. Portier-Fozzani, D. Ragaigne*, Astron. Astrophys. Suppl., **143**, 227, 2000.
11. *A. Riehokainen, S. Urpo, E. Valtaoja et al.*, Astron. Astrophys., **366**, 676, 2001.
12. *O.A. Golubchina, G.S. Golubchin*, Astrofiz. Issled. (Izv. Spec. Astrofiz. Obs.), **14**, 125, 1981.
13. *O.A. Golubchina, A.N. Korzhavin*, Geomag. Aeron., **54**, 1039, 2014.
14. *G.A. Dulk, K.V. Sheridan, S.F. Smerd, G.L. Withbroe*, Sol. Phys., **52**, 349, 1977.
15. *Z. Wang, E.J. Schmahl, M.R. Kundu*, Sol. Phys., **111**, 419, 1987.
16. *K. Shibasaki, C.E. Alissandrakis, S. Pohjolainen*, Sol. Phys., **273**, 309, 2011.
17. *P. Lantos, C.E. Alissandrakis, T. Gergely, M.R. Kundu*, Sol. Phys., **112**, 325, 1987.
18. *V.V. Zheleznyakov*, Radioemission of the Sun and Planets. Moscow: Nauka, 1964 (in Russian).

Magnetic Fields in Massive Stars: New Insights

S. Hubrig[1], M. Schöller[2], A.F. Kholtygin[3], L.M. Oskinova[4], I. Ilyin[1]

E-mail: *shubrig@aip.de*

Substantial progress has been achieved over the last decade in studies of stellar magnetism due to the improvement of magnetic field measurement methods. We review recent results on the magnetic field characteristics of early B- and O-type stars obtained by various teams using different measurement techniques.

1 Massive O-type stars with different spectral designations and kinematic characteristics

During the last years, a number of magnetic studies focused on the detection of magnetic fields in massive early B- and O-type stars. The characterization of magnetic fields in massive stars is indispensable to understand the conditions controlling the presence of those fields and their implications for the stellar physical parameters and evolution. Accurate studies of the age, environment, and kinematic characteristics of magnetic stars are also promising to give us new insights into the origin of the magnetic fields. While a number of early B-type stars were detected as magnetic already several decades back, the first magnetic field detection in an O-type star was achieved only 13 years ago, even though the existence of magnetic O-type stars had been suspected for a long time. Indirect observational evidences for the presence of magnetic fields were the many unexplained phenomena observed in massive stars, which are thought to be related to magnetic fields, like cyclical wind variability, Hα emission variation, chemical peculiarity, narrow X-ray emission lines, and non-thermal radio/X-ray emission.

However, direct measurements of the magnetic field strength in massive stars, using spectropolarimetry to determine the Zeeman splitting of the spectral lines, are difficult since only a few spectral lines are available for these measurements. In addition, these spectral lines are usually strongly broadened by rapid rotation and macroturbulence and frequently appear in emission or display P Cyg profiles. In high-resolution spectropolarimetric observations, broad spectral lines frequently extend over adjacent orders, so that it is necessary to adopt order

[1] Leibniz-Institut für Astrophysik Potsdam (AIP), Germany
[2] European Southern Observatory, Germany
[3] Astronomical Institute, St. Petersburg State University, Russia
[4] Institut für Physik und Astronomie, Universität Potsdam, Germany

V. Grinin et al. (eds) Radiation mechanisms of astrophysical objects. Yerevan: Edit Print, 2017, pp. 187–196.

shapes to get the best continuum normalization. Furthermore, most of the existing high-resolution spectropolarimeters are operating at smaller telescopes and cannot deliver the necessary high signal-to-noise (SNR) observations for a majority of the massive stars. Especially, O-type stars and Wolf-Rayet (WR) stars are rather faint. Indeed, the Bright Star Catalog contains only about 50 O-type stars and only very few WR stars.

In view of the large line broadening in massive stars, to search for the presence of magnetic fields, the low-resolution VLT instrument FORS 2 – and prior to that FORS 1 – appears to be the most suitable instrument in the world, offering the appropriate spectral resolution and the required spectropolarimetric sensitivity, giving access to massive stars even in galaxies in our neighborhood. Only the Faint Object Camera and Spectrograph at the Subaru Telescope has an operating spectropolarimetric mode, and, pending the commissioning of the PEPSI spectrograph in polarimetric mode installed at the Large Binocular Telescope, no further high-resolution spectropolarimetric capabilities are available on any of the 8–10 m class telescopes.

The first spectropolarimetric observations of O-type stars at ESO started with FORS 1 already in 2005. During a survey of thirteen O-type stars, the discovery of the presence of a magnetic field was announced in the Of?p star HD 148937 [3]. The class of Of?p stars was introduced by Walborn [5] and includes only five stars in our Galaxy. Of?p stars display recurrent spectral variations in certain spectral lines, sharp emission or P Cygni profiles in He I and the Balmer lines, and strong C III emission lines around 4650 Å. In the last years, it was shown that all Of?p stars are magnetic with field strengths from a few hundred Gauss to a few kG. Among them, only two Of?p stars, HD 148937 and CPD–28 2561 are observable from Paranal and, noteworthy, the first magnetic field detections were achieved through FORS 1 and FORS 2 observations [4].

All FORS 1/2 observations of HD 148937 are presented in Fig. 1 together with the ESPaDOnS observations obtained at CFHT [2]. This figure demonstrates the excellent agreement between the FORS 2 and ESPaDOnS measurements, highlighting the outstanding potential of FORS 2 for the detection of magnetic fields and the investigation of the magnetic field geometry in massive stars. Notably, while an exposure time of 21.5 h at the CFHT was necessary to obtain seven binned measurements, the exposure time for the individual FORS 2 observations accounted only for two to four minutes and only 2.3 h were used for the observations at six different epochs, including telescope presets and the usual overheads for readout time and retarder waveplate rotation.

Also the FORS 2 measurements of the mean longitudinal magnetic field of the second Of?p star, CPD–28 2561, were consistent with a single-wave variation during the stellar rotation cycle, indicating a dominant dipolar contribution to the magnetic field topology with an estimated polar strength of the surface dipole B_d larger than 1.15 kG [6]. Interestingly, in the studies of these two Of?p stars, none of the reported detections reached a 4σ significance level. While 3σ detections with FORS 2 can not always be trusted

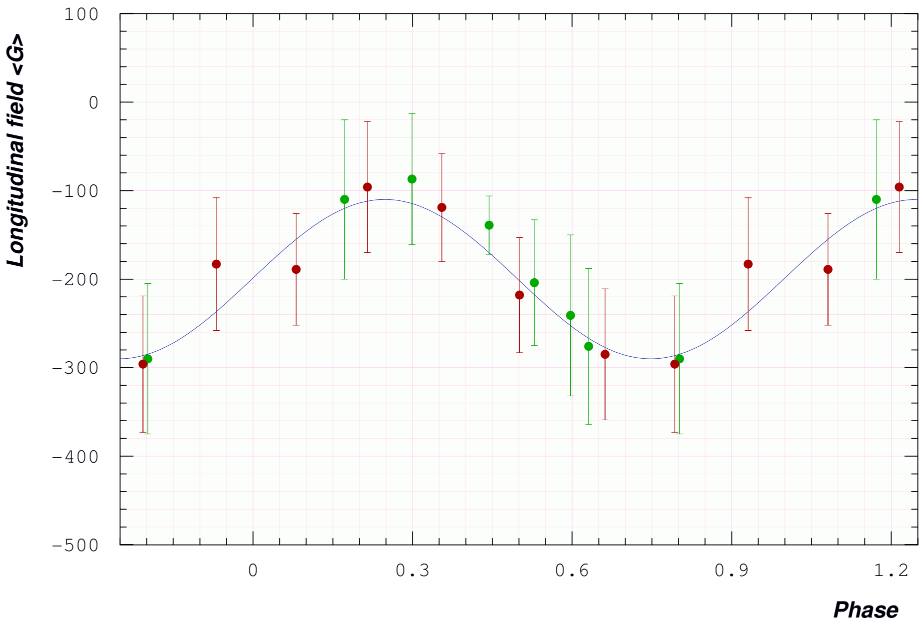

Figure 1: Longitudinal magnetic field variation of the Of?p star HD 148937 according to the 7.032 d period determined by Nazé et al. [1]. Red symbols correspond to ESPaDOnS observations [2], while green symbols are FORS 1 and FORS 2 measurements [3, 4]. Note that the measurement errors for both ESPaDOnS and FORS 1/2 observations are of similar order.

for single observations, they are genuine if the measurements show smooth variations over the rotation period, similar to those found for the Of?p stars HD 148937 and CPD–28 2561. The detection of rotational modulation of the longitudinal magnetic field is important to constrain the global field geometry necessary to support physical modeling of the spectroscopic and light variations.

To identify and to model the physical processes responsible for the generation of their magnetic fields, it is important to establish whether magnetic fields can also be detected in massive stars that are fast rotators and have runaway status. Recent detections of strong magnetic fields in very fast rotating early B-type stars indicate that the spindown timescale via magnetic braking can be much longer than the estimated age of these targets (e.g. [7]). Furthermore, current studies of their kinematic status identified a number of magnetic O and Of?p stars as candidate runaway stars (e.g. [8]). Increasing the known number of magnetic objects with extreme rotation, which are probably products of a past binary interaction, is important to understand the magnetic field origin in massive stars. The star ζ Ophiuchi (=HD 149757) of spectral type O9.5V is a well-known rapidly rotating runaway star, rotating almost at break-up velocity with $v \sin i = 400\,\mathrm{km\,s^{-1}}$ [9]. The analysis of the FORS 2 observations showed the presence of a weak magnetic field with a reversal of polarity [4] and an amplitude of about 100 G. The resulting periodogram for the magnetic field measurements using all available lines showed a dominating peak corresponding to a period of about 1.3 d which is roughly double the period of 0.643 d determined by Pollmann [10], who studied the variation of the equivalent width of the He I 6678 line.

The presence of magnetic fields might change our whole picture about the evolution from O stars via WR stars to supernovae or gamma-ray bursts. Neglecting magnetic fields could be one of the reasons why models and observations of massive-star populations are still in conflict. Another potential importance of magnetic fields in massive stars concerns the dynamics of stellar winds. A few years ago, Hubrig et al. [11] carried out FORS 2 observations of a sample of Galactic WR stars including one WR star in the Large Magellanic Cloud. Magnetic fields in WR stars are especially hard to detect because of wind-broadening of their spectral lines. Moreover, all photospheric lines are absent and the magnetic field is measured on emission lines formed in the strong wind. Remarkably, spectropolarimetric monitoring of WR 6, one of the brightest WR stars, revealed a sinusoidal nature of $\langle B_z \rangle$ variations with a period of 3.77 d with an amplitude of only 70–90 G.

2 Pulsating massive stars

Recent high-precision uninterrupted high-cadence space photometry using a number of satellites (e.g., WIRE, MOST, CoRoT, Kepler, BRITE) led to a revolutionary change in the observational evaluation of variability of massive stars. Supported by results of photometric monitoring, it is expected that a large fraction of massive stars show photometric variability due to either β Cep- or SPB-like pulsations, or stochastic p-modes, or convectively-driven internal gravity waves.

High-resolution spectropolarimetric observations of pulsating stars frequently fail to show credible measurement results, if the whole sequence of subexposures at different retarder waveplate angles has a duration comparable to the timescale of the pulsation variability. As an example, even for the bright fourth magnitude β Cephei star ξ^1 CMa with a pulsation period of 5 h, a full HARPS sequence of subexposures requires about 30 min. In contrast, one FORS 2 observation of the same star lasts less than 10 min. Owing to the strong changes in the line profile positions and the shapes in the spectra of pulsating stars, a method using spectra averaged over all subexposures leads to erroneous wavelength shifts and thus to wrong values for the longitudinal magnetic field.

For the first time, FORS 1 magnetic field surveys of slowly pulsating B (SPB) stars and β Cephei stars were carried out from 2003 to 2008. As a number of pulsating stars showed the presence of a magnetic field, our observations implied that β Cephei and SPB stars can no longer be considered as classes of non-magnetic pulsators. Notably, although the presence of magnetic fields

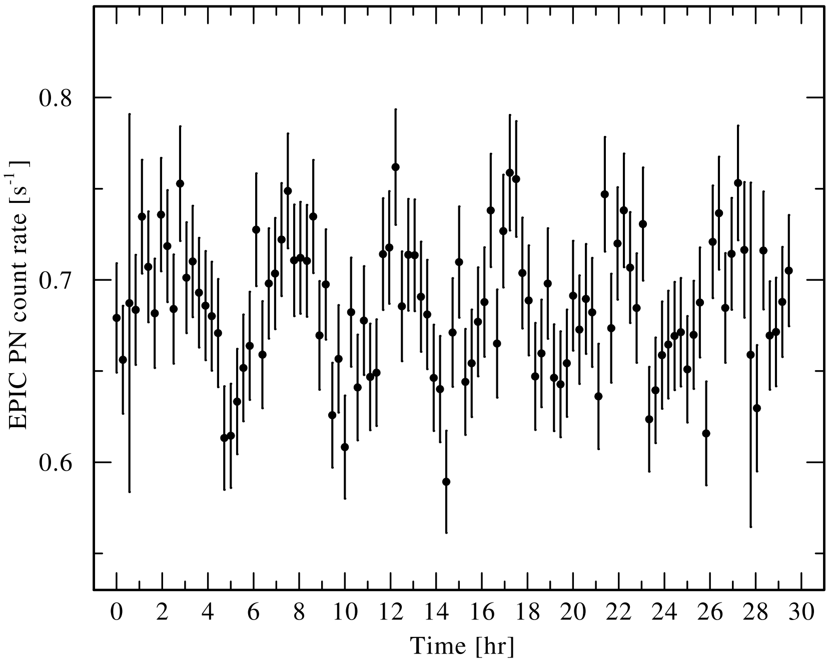

Figure 2: X-ray light curve of ξ^1 CMa in the 0.2 keV – 10.0 keV (1.24 Å – 62 Å) energy band, where the background was subtracted. The horizontal axis denotes the time after the beginning of the observation in hours. The data were binned to 1000 s. The vertical axis shows the count rate as measured by the EPIC PN camera. The error bars (1σ) correspond to the combination of the error in the source counts and the background counts.

in these stars is already known for more than ten years, the effect of these fields on the oscillation properties is not yet understood and remains to be studied. ξ^1 CMa, discovered as magnetic with FORS 1 observations long ago, is still the record holder with the strongest mean longitudinal magnetic field among the β Cephei stars of the order of 300–400 G [12]. Using FORS 2 measurements obtained in service mode in 2009/10, Hubrig et al. [13] detected a rotational modulation of its magnetic field with a period of about 2.19 d and estimated a magnetic dipole strength of about 5.3 kG.

Fully unexpected, observations of this particular star with the *XMM-Newton* telescope revealed for the first time X-ray pulsations with the same period as the stellar radial pulsation [14]. In Figs. 2 and 3, we present the observed X-ray light curve and the X-ray/optical light curves phased with the pulsation period. This first discovery of X-ray pulsations from a non-degenerate massive star stimulates theoretical considerations for the physical processes operating in magnetized stellar winds.

Observations of pulsating stars also allowed the first detection of a magnetic field in another β Cephei star, ϵ Lup [15], which is an SB2 system and recently received attention due to the presence of a magnetic field in both components.

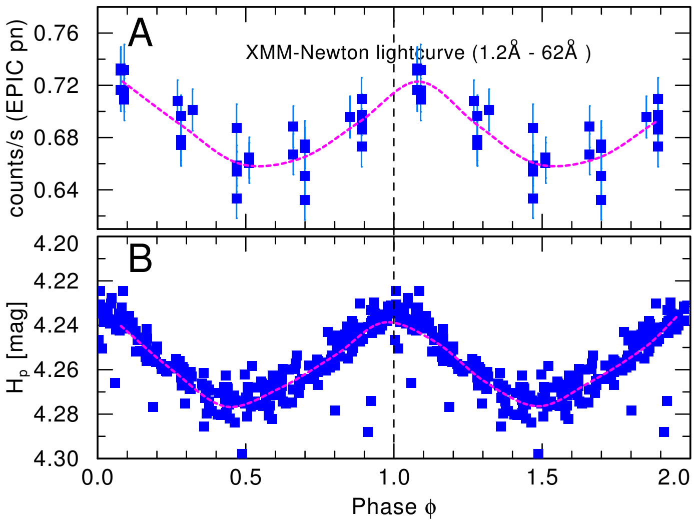

Figure 3: X-ray (upper panel) and optical (lower panel) light curves of ξ^1 CMa, phased with the stellar pulsation period. The X-ray light curve is produced from the data obtained with the *XMM-Newton* EPIC PN camera, using 1 h binning. The dashed red line interpolates the averages in phase bins of $\Delta\phi = 0.1$. The lower panel shows the *Hipparcos* Catalogue Epoch Photometry data. The abscissa is the magnitude H_p in the *Hipparcos* photometric system (330–900 nm with maximum at about 420 nm). The dashed red line interpolates the averages.

Since binary systems with magnetic components are rather rare, the detection of a magnetic field in this system using low resolution FORS spectropolarimetry indicates the potential of FORS 2 also for magnetic field searches in binary or multiple systems.

3 Improvements in the measurement techniques

During the last years, the measurement strategy for high-resolution and low-resolution spectropolarimetric observations was modified in many aspects. To measure the mean longitudinal magnetic fields in high-resolution polarimetric spectra obtained with ESPaDOnS, NARVAL, and HARPS, most teams are using the moment technique introduced by Mathys [16] and the Least-Squares Deconvolution (LSD) introduced by Donati et al. [17]. In the last years, Carroll et al. [18] developed the multi-line Singular Value Decomposition (SVD) method for Stokes Profile Reconstruction. The basic idea of SVD is similar to the Principal Component Analysis approach, where the similarity of the individual Stokes V profiles allows one to describe the most coherent and systematic features present in all spectral line profiles as a projection onto a small number of eigenprofiles (e.g. [19]). The excellent potential of the SVD method, especially in the analysis of extremely weak fields, e.g. in the Herbig Ae/Be star PDS 2, was recently demonstrated by Hubrig et al. ([20], right side of their Fig. 4).

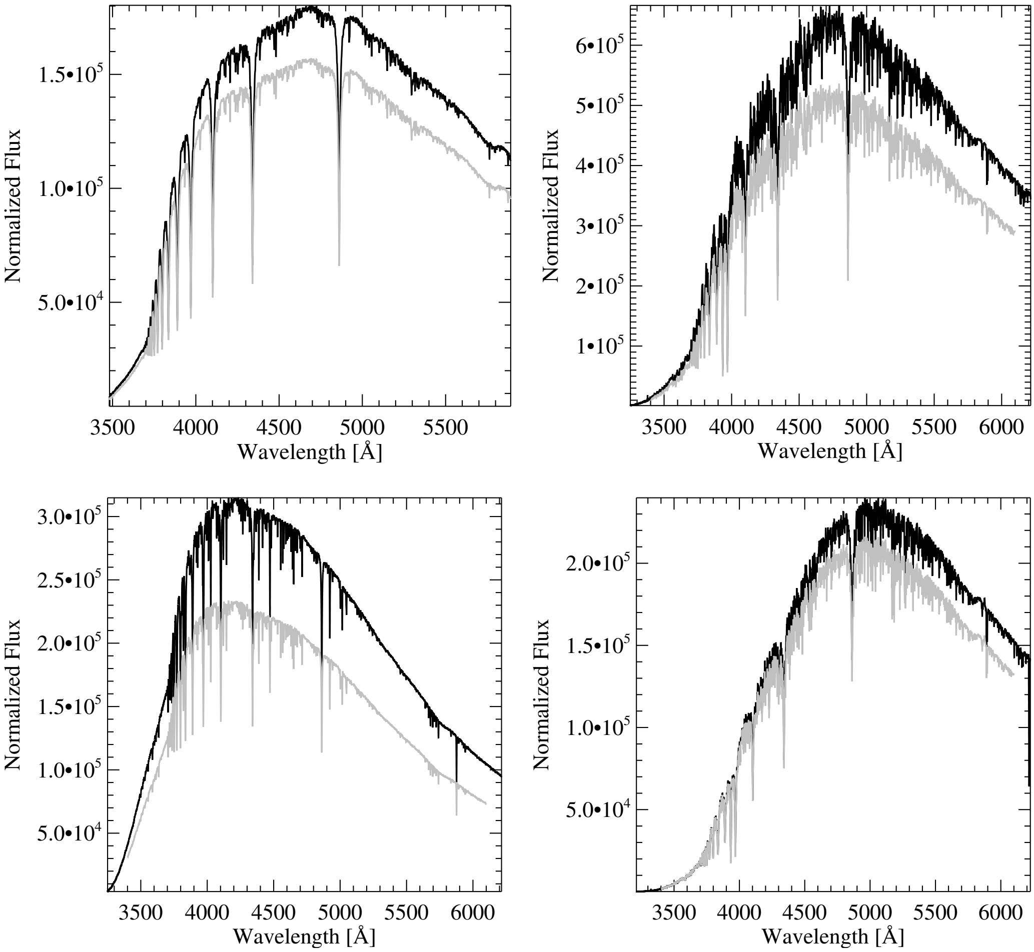

Figure 4: Fluxes extracted by Bagnulo et al. [22] (grey color) compared to those using our own pipeline (black color). The differences in the fluxes are presented (from left to right) for the HgMn star α And, the δ Scuti star HD 21190, the nitrogen rich early B-type star HD 52089, and the Herbig Ae star PDS 2. All these stars were announced in studies by Hubrig et al. as magnetic.

In the reduction process of low-resolution spectropolarimetric observations, Hubrig et al. [21] perform rectification of the V/I spectra and calculate null profiles, N, as pairwise differences from all available V profiles. From these, 3σ-outliers are identified and used to clip the V profiles. This removes spurious signals, which mostly come from cosmic rays, and also reduces the noise. A full description of the updated data reduction and analysis will be presented in a paper by Schöller et al. (*in preparation*).

The mean longitudinal magnetic field, $\langle B_\mathrm{z}\rangle$, is defined by the slope of the weighted linear regression line through the measured data points, where the weight of each data point is given by the squared signal-to-noise ratio of the Stokes V spectrum. The formal 1σ error of $\langle B_\mathrm{z}\rangle$ is obtained from the standard relations for weighted linear regression. This error is inversely proportional to the rms signal-to-noise ratio of Stokes V. Finally, we apply the factor $\sqrt{\chi^2_{\min}/\nu}$ to the error determined from the linear regression, if larger than 1.

Since 2014, Hubrig et al. [21] also implement the Monte-Carlo bootstrapping technique, where they typically generate $M = 250\,000$ statistical variations of the original dataset, and analyze the resulting distribution $P(\langle B_{\rm z}\rangle)$ of the M regression results. Mean and standard deviation of this distribution are identified with the most likely mean longitudinal magnetic field and its 1σ error, respectively. The main advantage of this method is that it provides an independent error estimate.

A number of discrepancies in the published measurement accuracies has been reported by Bagnulo et al. [22] who used the ESO FORS 1 pipeline to reduce the full content of the FORS 1 archive. The same authors already published a few similar papers in the last years suggesting that very small instrument flexures, negligible in most of the instrument applications, may be responsible for some spurious magnetic field detections, and that FORS detections may be considered reliable only at a level greater than 5σ. However, no report on the presence of flexures from any astronomer observing with the FORSes was ever published in the past. The authors also discuss the impact of seeing, if the exposure time is comparable with the atmospheric coherence time, which they incorrectly assume to be in seconds and not in milliseconds. In the most recent work do the authors present for the first time the level of intensity fluxes for each image and report which spectral regions were used for the magnetic field measurements. However, no fluxes for left-hand and right-hand polarized spectra are available, thus the reproduction of their measurements is not possible. Notably, already small changes in the spectral regions selected for the measurements can have a significant impact on the measurement results [23].

Since the measurement accuracies predominantly depend on photon noise, an improper extraction of the spectra, for instance the use of smaller extraction windows, would explain why Bagnulo et al. [22] disregarded 3σ detections by other authors. Indeed, the inspection of the levels of intensity fluxes for each subexposure compiled in the catalog of Bagnulo et al. [22] shows that their levels are frequently lower, down to 70% in comparison to those obtained in our studies. In Fig. 4 we present the comparison of fluxes for a few stars for which detections were achieved and published by Hubrig et al. during the last years. It is obvious that the detection of weak magnetic fields is especially affected if the extracted fluxes are low. From the consideration of the SNR values presented by Bagnulo et al. [22], we also noted that emission lines are not taken into account during the measurements. The reason for this is not clear to us as there is no need to differentiate between absorption and emission lines: the used relation between the Stokes V signal and the slope of the spectral line wing holds for both type of lines, so that the signals of emission and absorption lines add up rather than cancel.

4 Summary

To increase the reliability of magnetic field detections, but also to carry out a quantitative atmospheric analysis and to probe spectral variability, it is certainly helpful to follow up FORS 2 detections with high-resolution HARPS observations. To our knowledge, the only collaboration that uses FORS 2 and HARPS to monitor magnetic fields is the BOB ("B-fields in OB stars") collaboration [24], which is focused on the search of magnetic fields in massive stars. Combining observations with different instruments allowed the BOB collaboration to report during the last couple of years the presence of magnetic fields in a number of massive stars. As an example, the first detection of a magnetic field in the single slowly rotating O9.7 V star HD 54879 was achieved with FORS 2 and follow-up HARPS observations could show that HD 54879 is, so far, the strongest magnetic single O-type star detected with a stable and normal optical spectrum [25].

References

1. *Y. Nazé, A. Ud-Doula, M. Spano et al.*, Astron. Astrophys., **520**, A59, 2010.
2. *G.A. Wade, G. Grunhut, G. Gräfener et al.*, Mon. Not. Roy. Astron. Soc., **419**, 2459, 2012.
3. *S. Hubrig, M. Schöller, R.S. Schnerr et al.*, Astron. Astrophys., **490**, 793, 2008.
4. *S. Hubrig, M Schöller, I. Ilyin et al.*, Astron. Astrophys., **551**, A33, 2013.
5. *N.R. Walborn*, Astron. J., **78**, 1067, 1973.
6. *S. Hubrig, M. Schöller, A.F. Kholtygin et al.*, Mon. Not. Roy. Astron. Soc., **447**, 1885, 2015.
7. *T. Rivinius, R.H.D. Townsend, O. Kochukhov et al.*, Mon. Not. Roy. Astron. Soc., **429**, 177, 2013.
8. *S. Hubrig, N.V. Kharchenko, M. Schöller*, Astron. Nachr., **332**, 65, 2011.
9. *E. Kambe, R. Hirata, H. Ando*, Astron. Astrophys., **273**, 435, 1993.
10. *E. Pollmann*, Inf. Bull. Var. Stars, No. 6034, 1, 2012.
11. *S. Hubrig, K. Scholz, W.-R. Hamann et al.*, Mon. Not. Roy. Astron. Soc., **458**, 3381, 2016.
12. *S. Hubrig, M. Briquet, M. Schöller et al.*, Mon. Not. Roy. Astron. Soc., **369**, L61, 2006.
13. *S. Hubrig, I. Ilyin, M. Schöller et al.*, Astrophys. J. Lett., **726**, L5, 2011.
14. *L.M. Oskinova, Y. Nazé, H. Todt et al.*, Nature Commun., **5**, 4024, 2014.
15. *S. Hubrig, M. Briquet, P. De Cat et al.*, Astron. Nachr., **330**, 317, 2009.
16. *G. Mathys*, Proc. IAU Coll., **138**, 232, 1993.

17. *J.F. Donati, M. Semel, B.D. Carter et al.*, Mon. Not. Roy. Astron. Soc., **291**, 658, 1997.

18. *T.A. Carroll, K.G. Strassmeier, J.B. Rice, A. Künstler*, Astron. Astrophys., **548**, A95, 2012.

19. *T.A. Carroll, M. Kopf, K.G. Strassmeier, I. Ilyin*, Proc. IAU Symp., **259**, 633, 2009.

20. *S. Hubrig, T.A. Carroll, M. Schöller, I. Ilyin*, Mon. Not. Roy. Astron. Soc., **449**, L118, 2015.

21. *S. Hubrig, M. Schöller, A.F. Kholtygin*, Mon. Not. Roy. Astron. Soc., **440**, 1779, 2014.

22. *S. Bagnulo, L. Fossati, J.D. Landstreet, C. Izzo*, Astron. Astrophys., **583**, A115, 2015.

23. *S. Hubrig, D.W. Kurtz, S. Bagnulo et al.*, Astron. Astrophys., **415**, 661, 2004.

24. *T. Morel, N. Castro, L. Fossati et al.*, The Messenger, **157**, 27, 2014.

25. *N. Castro, L. Fossati, S. Hubrig et al.*, Astron. Astrophys., **581**, A81, 2015.

* The color figures are available online in the Proceedings at *http://www.astro.spbu.ru/sobolev100/*.

Relative Intensities of Hydrogen Lines as a Tool to Study Astrophysical Plasma

N.A. Katysheva[1], V.P. Grinin[2,3]

E-mail: *natkat2006@mail.ru*

The hydrogen lines play an important role in diagnostics of astrophysical plasma. In recent years, the lines of higher hydrogen series became the objects of the research, thanks to the rapid development of the infrared spectroscopy. In this paper we investigate the relative intensities of the Paschen and Brackett lines as well as the ratio of $I(L_\alpha)/I(H_\alpha)$ over a large range of the optical depth of gas. The calculations are fulfilled on the basis of the Sobolev approximation for collisional excitations and ionizations of atoms for the electron temperature $T_e < 10000$ K. The behavior of the electron density N_e at the gas thermalization is investigated. It is shown that a very sharp jump in the degree of ionization is observed near the LTE conditions. The obtained results can be used both for the diagnostics of emitting regions and for determining the extinction for the objects with strong absorption.

1 Introduction

Emission hydrogen lines are present in spectra of different astrophysical objects – from cool stars to quasars and Seyfert galaxies. They indicate the deviation from the local thermodynamic equilibrium (LTE). Earlier, the visible spectral range was the basic one, and the Balmer emission lines were observed most frequently, making the theory of Balmer decrement (B.D.) one of the main methods of the diagnostics of emitting gas. The most detailed calculations of B.D. for a multi-level hydrogen atom were carried out on the basis of the escape probability method by V.V. Sobolev [1] for different cases of excitation and ionization of the gas. Boyarchuk [2], Hirata and Uesugi [3] calculated B.D. for radiative excitations and ionizations, Gershberg and Schnol [4], Grinin and Katysheva [5] computed B.D. just for collisional ones. Ilmas [6], Grinin and Katysheva [7] considered both the cases. The relative intensities of the Paschen, Brackett and Pfund series of hydrogen were calculated by Luud and Ilmas [8] to explain the spectra of γ Cas [8].

The Lyman and Balmer decrements for collisional excitations and ionizations were computed in [5] for a wide range of the electron temperatures ($T_e = 10000$–20000 K), electron number densities ($N_e = 10^7$–10^{13} cm^{-3}) and the escape probabilities ($\beta_{12} = 1$–10^{-8}), where β_{12} was the photon escape probability

[1] Sternberg State Astronomical Institute, Lomonosov Moscow State University, Russia
[2] Main Astronomical Observatory, Pulkovo, Russia
[3] Sobolev Astronomical Institute, St. Petersburg State University, Russia

V. Grinin et al. (eds) Radiation mechanisms of astrophysical objects. Yerevan: Edit Print, 2017, pp. 197–202.

in the Lyman α line. This quantity is connected with the optical depth τ_{12} of the Lyman α line (in the 1D model) by the following formula:

$$\beta_{12} = (1 - \exp(-\tau_{12}))/\tau_{12}. \quad (1)$$

In the paper [5] it was originally shown that for $T_e = 10000\,\mathrm{K}$ the theoretical ratio of Lyα and Baα line intensities, $I(L_\alpha)/I(H_\alpha)$, could be of the order of unity or smaller, for large N_e and large optical thickness of emitting gas. On the basis of those calculations, the intensities of the Lyman, Balmer and Paschen lines of quasars and Seyfert galaxies were discussed in [9].

2 The ratio $I(L_\alpha)/I(H_\alpha)$

The progress in new astronomical equipment in recent years allowed an inclusion of the lines of Lyman and far infrared series of hydrogen in the analysis. The ratio $I(L_\alpha)/I(H_\alpha)$ is of considerable interest. The first data on $I(L_\alpha)/I(H_\alpha)$ in solar outbursts, quasars and Seyfert galaxies were obtained in the middle of the 1970s. In the case of the recombination mechanism (Menzel's case A), this ratio is more than 10. Zirin [10], and Canfield and Puetter [11] presented first results of observations of Lyman and Balmer lines. They found that the ratio $I(L_\alpha)/I(H_\alpha)$, on average, was of the order of 1. Then, Allen et al. [12] measured the $I(L_\alpha)/I(H_\alpha)$ ratio for some quasars, where it was in the range 0.8–3. McCarthy et al. [13] found that $I(L_\alpha)/I(H_\alpha)$ was equal to 4.7($\pm$1.8) and 3.5($\pm$1.3) for the radio galaxies with redshift of about 2.4: B3 0731+438 and MRC 0406-244, respectively. Explanations of the discrepancy between Menzel's case A and obtained $I(L_\alpha)/I(H_\alpha)$ were suggested in the papers [14]–[18]. It was shown that a small ratio $I(L_\alpha)/I(H_\alpha)$ could be derived for large optical depth and strong radiation.

In this paper, we continued our calculations and computed the populations of the hydrogen atomic levels and the line intensities on the base of the Sobolev approximation for the case of collisional excitations and ionizations, using our program described in [5]. We considered the model of a 15-level atom for the gas velocity $V = 300$ km/s. The model parameters were: $T_e = 8000$ and $9000\,\mathrm{K}$ and hydrogen density $N_H = 10^{11}$ and 10^{12} cm^{-3}.

In Fig. 1 the dependence of the $I(L_\alpha)/I(H_\alpha)$ ratio on the geometrical depth of the emitting gas, Z, is presented. The graph shows that an increase of Z (and, correspondingly, an increase of the optical depth) leads to a decrease of this ratio – firstly smooth and later sharp – from about 700 down to 1 or less. Such a behavior of the relative intensities is caused by approaching the physical state of gas to the LTE.

It is interesting to consider the electron density N_e as a function of the layer geometrical thickness Z. In Fig. 2 we show results of the calculations for two values of T_e (8000 and 9000 K) and two values of the hydrogen density N_H. We see that for low thickness Z, the degree of ionization is small and N_e is practically constant.

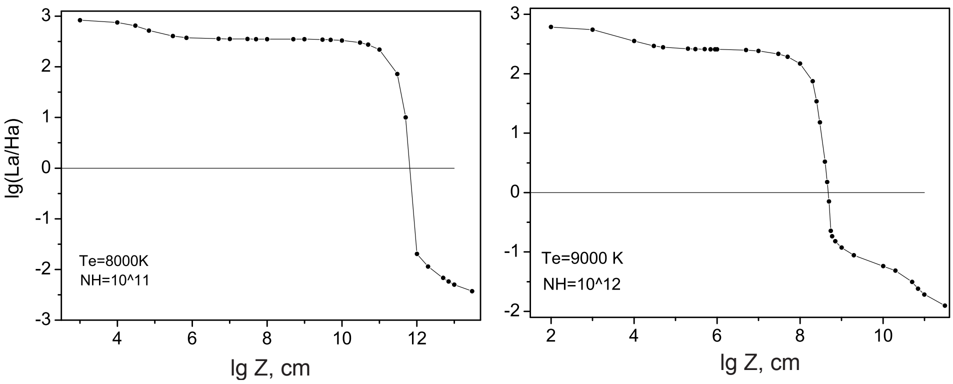

Figure 1: The ratio $I(L_\alpha)/I(H_\alpha)$ vs the geometrical depth Z (in cm) of the emitting gas for $T_e = 8000$ K, $N_H = 10^{11}$ cm^{-3} (left) and $T_e = 9000$ K, $N_H = 10^{12}$ cm^{-3} (right).

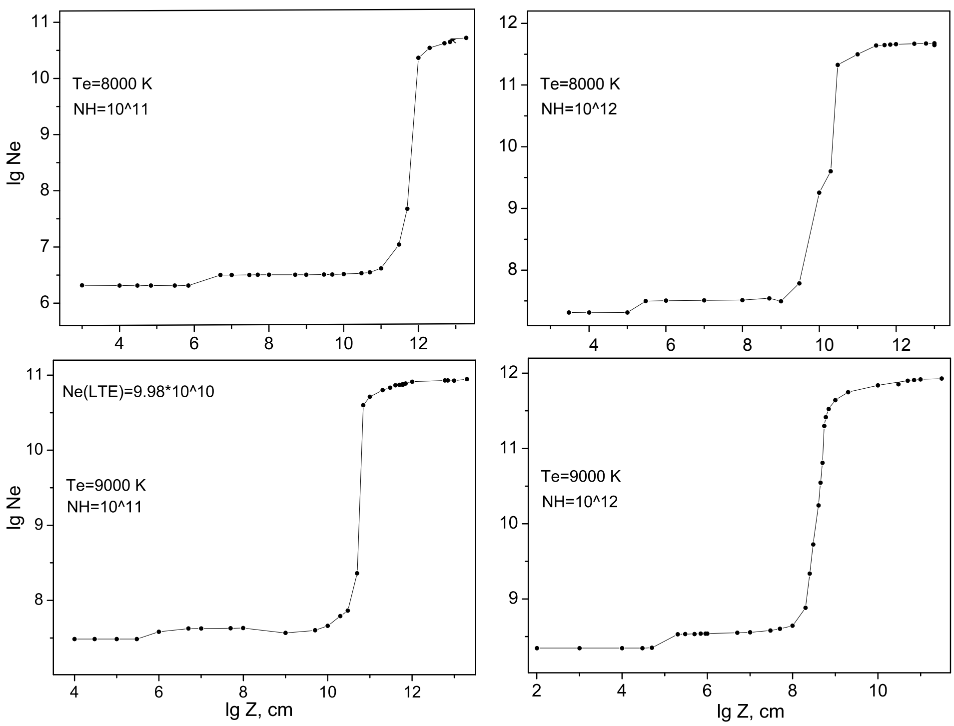

Figure 2: N_e vs the geometrical depth Z for $T_e = 8000$ and 9000 K, $N_H = 10^{11}$ cm^{-3} (left) and 10^{12} cm^{-3} (right).

At $Z \approx 10^5$ cm a small step is visible on the curves as N_e increases slightly due to the blocking of the radiation beyond the Lyman jump. Further growth of Z leads to an increase of the degree of ionization. A dramatic stepwise rise of the degree of ionization by about 10^4 times (!) occurs at a comparatively small interval of Z (depending on T_e and N_H). The comparison of Fig. 2 and Fig. 1 shows that a sharp increase of N_e and a strong decrease of $I(L_\alpha)/I(H_\alpha)$ occur in the same thickness range in which the gas conditions are close to the LTE.

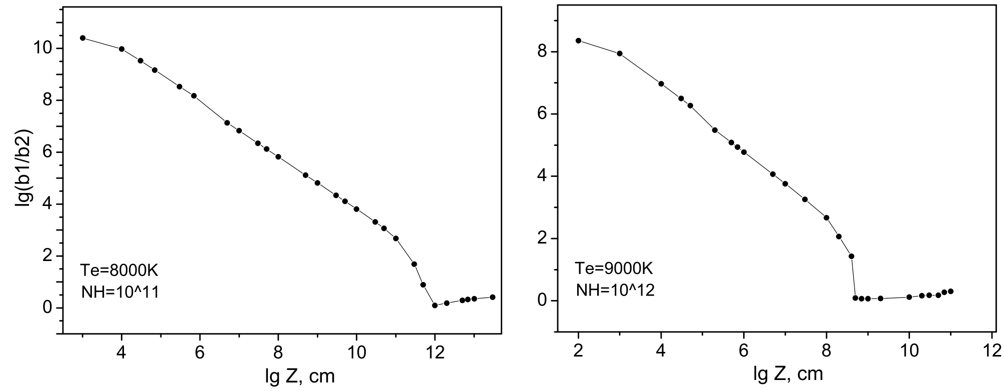

Figure 3: The ratio of Menzel parameters b_1/b_2 as a function of the geometrical depth Z for $T_e = 8000$ K, $N_H = 10^{11}$ cm^{-3} (left) and $T_e = 9000$ K, $N_H = 10^{12}$ cm^{-3} (right).

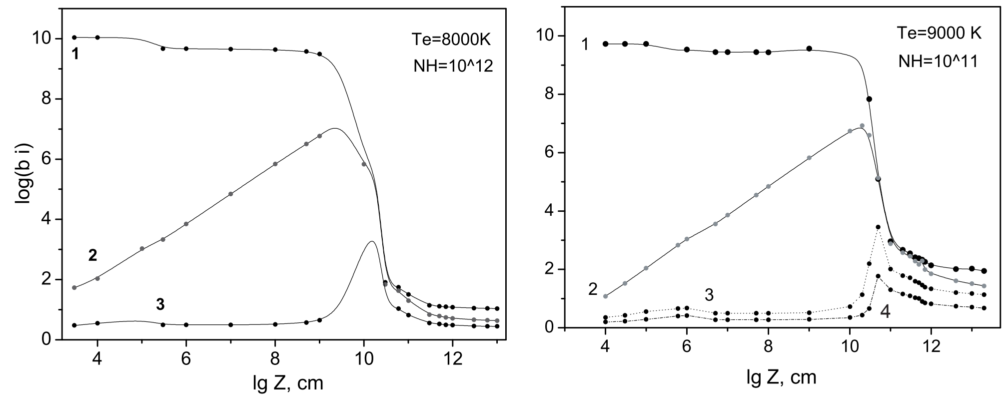

Figure 4: Dependence of b_i on the geometrical depth Z for $T_e = 8000$ K, $N_H = 10^{12}$ cm^{-3} (left) and 9000 K, $N_H = 10^{11}$ cm^{-3} (right). Indices 1, 2, 3 near the curves indicate the number of the atomic level.

What is the reason of such a sharp jump of N_e and, correspondingly, of the degree of ionization? Figs. 3 and 4 show, respectively, the ratio of Menzel parameters b_1/b_2 and the parameters b_1, b_2, b_3 (in a logarithmic scale) as a function of Z. In Fig. 3 we see a graduate decline of the ratio (b_1/b_2) from small Z to a certain geometrical depth, and then the value of b_1/b_2 becomes practically constant. The reason is the large optical depth of gas in the L_α and H_α lines at which the emitting gas becomes thermalized.

In Fig. 4 we see that the curve 1 decreases slowly with the increasing optical depth in the Lyman and then the Balmer lines, while curve 2 increases, and this corresponds to the decline in Fig. 3. If the optical depth of higher series is small, the values b_3 and b_4 change weakly. When the emitting gas becomes optically thick in the Paschen lines, the parameters b_3 and b_4 increase. Further thermalization of gas quickly reduces the Menzel parameters b_1 and b_2, and the role of collisional excitations from the excited levels and multi-cascade ionization increases essentially.

3 Infrared lines

Last years the far infrared spectroscopy developed very actively. For instance, high-resolution IR spectra of hot stars γ Cas, HD 45677, P Cyg with multiple lines of hydrogen (from Pfund to Humphrey series) were obtained. Lenorzer [19] presented ISO (Infrared Space Observatory) spectra and used them to diagnose the radiating gas, by considering fluxes in the lines Hu(14-6), Brα, Pfγ, and their ratios. They showed that on the diagram Hu(14-6)/Brα vs Hu(14-6)/Pfγ, there was a split of optically thin stellar winds and optically thick discs. For example, the fluxes of P Cyg and η Car are close to the optically thin case, whereas γ Cas to the optically thick one. Therefore, the lines of high series can give an additional information about the gas parameters.

Edwards et al. [20] carried out spectroscopic observations of 16 T Tauri stars, analyzed intensities of the Paschen and Brackett lines and compared them to the theoretical ones for Menzel's case B and those calculated by Kwan and Fischer [21]. The statistics of the observed intensity ratios $I(P_\alpha)/I(P_\beta)$ showed that they were less than 1, and P_β/Br_γ ratio was in the range from 3 to 6.

So, the diagnostics of IR-lines could give a significant contribution to study of stellar envelopes. Let us consider the ratio of the line intensities $Br7/P7 = Br_\gamma/P_\delta = 0.420\,\beta_{47}/\beta_{37}$ and $P7/H7 = P_\delta/H_\varepsilon = 0.303\,\beta_{37}/\beta_{27}$. Since these lines are formed by the transitions from the same upper (seventh) level, the intensity ratios of these lines depend only on the corresponding values of the gas optical depths.

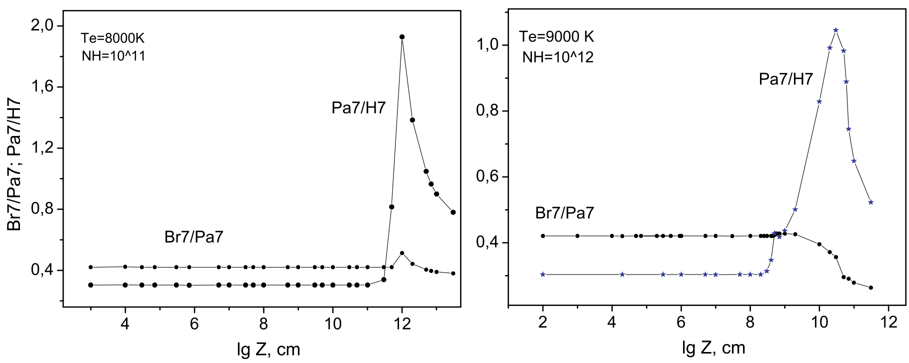

Figure 5: Ratios $I(Br_\gamma)/I(Pa_\delta)$ and $I(Pa_\delta)/I(H_\varepsilon)$ vs the geometrical thickness Z.

Fig. 5 presents the dependence of the ratios $I(Br_\gamma)/I(P_\delta)$ and $I(P_\delta)/I(H_\varepsilon)$ on Z. As it follows from the theoretical relations for the gas optically thin in the Paschen–Brackett series, these values are constant. With an increase of the optical depth $\tau_{L\alpha}$, the Menzel parameters b_i tend to equilibrium ones ($\sim$1).

If we known that the optical depth of P_α is less than 1, then it is possible to use the ratio of the lines mentioned above to estimate the interstellar or circumstellar extinction. Detailed calculations of $I(P_\alpha)/I(H_\alpha)$ have been carried out by Katysheva [9] for the case of collision ionizations and excitations for $T_e = 10000$–$20000\,$K.

4 Conclusion

The results of the calculations presented above show that the role of the multi-cascade ionizations grows rapidly with the increase of the optical depth in the subordinate lines as a result of line-blocking in these lines. This is a natural reaction of the gas approaching the LTE. Such a gas state is observed in the dense emitting regions, for example, in the flares of UV Cet-type stars [22, 23, 24].

Acknowledgments. This work was partly supported by Russian President grant NSh-1675.2014.2 (N.K.) and the RFBR grant 15-02-09191 (V.G.).

References

1. *V.V. Sobolev*, Moving Envelopes of Stars. Cambridge: Harvard University Press, 1960.
2. *A.A. Boyarchuk*, Bull. Crim. Astrophys. Obs., **35**, 45, 1966.
3. *R. Hirata, A. Uesugi*, Contrib. Kwasan Obs. Kyoto, **156**, 1967.
4. *R.E. Gershberg, E.E. Shnol*, Izv. Krym. Astrofiz. Obs., **50**, 1122, 1974.
5. *V.P. Grinin, N.A. Katysheva*, Bull. Crim. Astrophys. Obs., **62**, 52, 1980.
6. *M. Ilmas*, Hydrogen Lines in Spectra of Cool Stars. Tartu, 1974.
7. *V.P. Grinin, N.A. Katysheva*, Bull. Crim. Astrophys. Obs., **62**, 47, 1980.
8. *L. Luud, M. Ilmas*, Hydrogen Lines in Spectra of Stars. Tartu, 1974.
9. *N.A. Katysheva*, Astrophys., **19**, 32, 1983.
10. *H. Zirin*, Astrophys. J. Lett., **222**, L105, 1978.
11. *R.C. Canfield, R.C. Puetter*, Astrophys. J. Lett., **236**, L7, 1980.
12. *D. Allen, J.R. Barton, P.R. Gillingham, R.F. Carswell*, Mon. Not. Roy. Astron. Soc., **200**, 271, 1982.
13. *P.J. McCarthy, R. Elson, P. Eisenhardt*, Astrophys. J. Lett., **387**, L20, 1992.
14. *S.A. Drake, R.K. Ulrich*, Astrophys. J. Suppl., **42**, 351, 1980.
15. *R.C. Canfield, R.C. Puetter*, Astrophys. J., **236**, 390, 1981.
16. *R.C. Canfield, R.C. Puetter, P.J. Ricchiazzi*, Astrophys. J., **249**, 383, 1981.
17. *J. Kwan, J.H. Krolik*, Astrophys. J. Lett., **233**, L91, 1979.
18. *J.H. Krolik, C.F. McKee*, Astrophys. J. Suppl., **37**, 459, 1978.
19. *A. Lenorzer, B. Vandenbussche, P. Morris et al.*, Astron. Astrophys., **384**, 473, 2002.
20. *S. Edwards, J. Kwan, W. Fischer et al.*, Astrophys. J., **778**, 148, 2013.
21. *J. Kwan, W. Fischer*, Mon. Not. Roy. Astron. Soc., **411**, 2383, 2011.
22. *V.P. Grinin, V.V. Sobolev*, Astrophys., **13**, 348, 1977.
23. *V.V. Sobolev, V.P. Grinin*, Astrophys., **38**, 15, 1995.
24. *W.E. Kunkel*, Astrophys. J., **161**, 503, 1970.

Polarimetric Properties of Icy Moons of the Outer Planets

N.N. Kiselev[1,4], V.K. Rosenbush[1], V.L. Afanasiev[2], S.V. Zaitsev[1], S.V. Kolesnikov[3,4], D.N. Shakhovskoy[4]

E-mail: *kiselevnn@yandex.ru*

The progress in the study of polarization phenomena exhibited by planetary moons is reviewed. Besides previously published data, we focus primarily on the new results of our recent polarimetric observations of the Galilean satellites of Jupiter, bright satellites of Saturn (Enceladus, Dione, Rhea, Iapetus), and the major moons of Uranus (Ariel, Umbriel, Titania, Oberon) at backscattering geometries, including phase angles approaching zero. In addition to a negative branch of polarization, which is typical of atmosphereless solar system bodies (ASSBs), some high-albedo objects, including E-type asteroids, reveal a backscattering polarization feature in the form of a spike-like negative polarization minimum. These optical phenomena serve as important tests of modern theoretical descriptions of light scattering by regolith surfaces. We found the polarimetric properties of different ASSBs near opposition are highly various. The possible reasons for such behavior are discussed.

1 Introduction

The surfaces of planetary satellites are covered with regolith particles which are likely to be aggregates. The properties of the regolith (the structure and packing density of the aggregates, the sizes of constituents, compositions, shapes, and orientation) can be inferred from measurements of the polarization characteristics, namely, the degree P and the plane of linear polarization θ. The degree of polarization P varies with the phase angle α (the angle between the Sun and the observer as viewed from the object), producing polarization phase curve.

Many atmosphereless solar system bodies (ASSBs) exhibit a brightening and negative values of the degree of linear polarization (NPB) near the opposition $\alpha \leq 20°$. A class of high-albedo ASSBs (satellites of planets, E-type asteroids) reveals a unique combination of a nonlinear increase of brightness, so-called brightness opposition effect (BOE), and a sharp minimum of polarization (POE) centered at exactly the backscattering direction. There is also the so-called polarization longitude effect (PLE), i.e., a difference between the polarization

[1] Main Astronomical Observatory of the National Academy of Sciences of Ukraine
[2] Special Astrophysical Observatory of the Russian Academy of Sciences, Russia
[3] Observatory of Odessa National University, Ukraine
[4] Crimean Astrophysical Observatory, Crimea

V. Grinin et al. (eds) Radiation mechanisms of astrophysical objects. Yerevan: Edit Print, 2017, pp. 203–209.

curves for the leading and trailing hemispheres of satellites. Until the mid 1990s, the available polarimetric data, even for the bright Galilean moons of Jupiter, were rather limited and even mutually contradictory [1]. Polarization measurements of moons of the outer planets were scarce. Therefore, our goal was to fill in the missing data for the satellites of planets with different albedo which show the BOE. The objects of our program are the high-albedo Galilean moons of Jupiter (Io, Europa, Ganymede), Saturn's moons (Enceladus, Dione, Rhea, and Iapetus). We also include in our program the major moons of Uranus (Ariel, Umbriel, Titania, Oberon) as well as Jupiter's moon Callisto which are moderate-albedo objects, but demonstrate a sharp surge of brightness.

2 Observations

The polarimetric observations of the planetary satellites near opposition were carried out during different observing runs with different instruments in 1998–2015. The one-channel photopolarimeter of the 2.6 m Shain telescope and the UBVRI photopolarimeter of the 1.25 m telescope of the Crimean Astrophysical Observatory (CrAO) were used. A small part of observations was conducted at the 0.7 m telescope of the Chuguyev Observation Station of the Institute of Astronomy of Kharkiv National University (IAKhNU) and the 1 m telescope of the CrAO (Simeiz) using a one-channel photoelectric polarimeter of the IAKhNU. A description the polarimeters is given in [2]. The faint satellites of Uranus (Ariel, Umbriel, Titania, Oberon) were observed at the 6-m BTA telescope of the SAO with the multimode focal reducer SCORPIO-2 [3].

The degree of linear polarization P and the position angle of the polarization plane θ of the program objects were obtained with reduction programs specially designed for each polarimeter [2, 4]. From the observations of standard stars, we found the instrumental polarization fairly stable, always below 0.2% for all

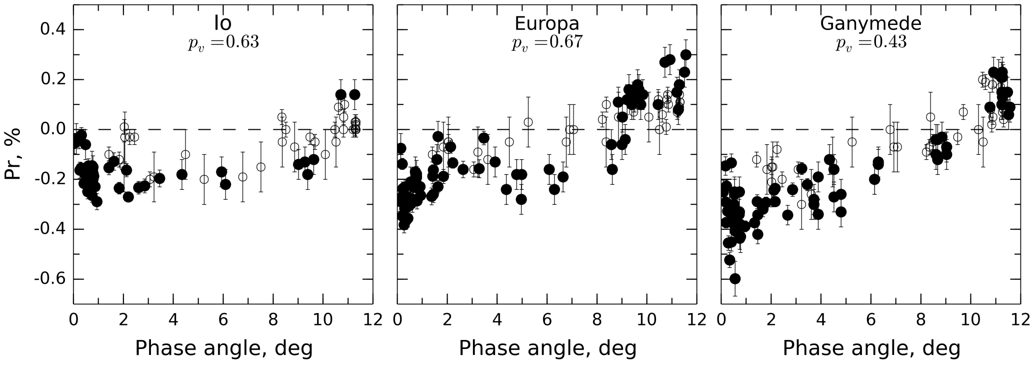

Figure 1: NPB for Io, Europa, and Ganymede with sharp minima of polarization centered at small phase angles. Dark symbols correspond to the present work, filters R and WR; open symbols to data from [5], filter V.

instruments. It was taken into account. A typical random error in the degree of linear polarization ranges from 0.02% to 0.1%, depending on the brightness of the satellite, the count accumulation time, and the observing conditions.

In planetary astrophysics, the polarization quantity of interest is $P_r = P\cos 2\theta_r$, where θ_r is the angle between the measured direction of the plane of linear polarization and the normal to the scattering plane. Thus, we present the results of our observations in the form of the phase–polarization curves (P_r versus α).

3 Results

3.1 The Galilean satellites: Io, Europa, Ganymede, and Gallisto

The polarization–phase curves for Io, Europa, and Ganymede are plotted in Fig.1.

We found that for all observations with $P \gg \sigma_P$, angle θ_r lies near 90°, and the values P_r are negative at all phase angles smaller than the inversion angle. As one can see in Fig. 1, the sharp asymmetric features with polarization minima about $-(0.3 \div 0.4)\%$ at phase angles $< 1°$ are observed. The shape of the negative polarization branches (NPB) of the satellites varies considerably from almost flat for Io up to strongly asymmetric curve for Ganymede.

Europa clearly demonstrates two minima at the NPB: $P_{min} \approx -0.4\%$ at $\alpha \approx 0.8°$ and $P_{min} \approx -0.2\%$ at $\alpha \approx 5.5°$. The same effect can be seen for Io and Ganymede, although less pronounced. The sharp secondary minimum of polarization centered at very small phase angle, called polarization opposition effect, was predicted by Mishchenko for high-albedo ASSBs [8].

A detailed study of the PLE for Callisto was carried out by Rosenbush [6]. The NPBs for the leading and trailing hemispheres of Callisto are the regular curves of polarization without any sharp asymmetric features like the POE (see Fig. 2).

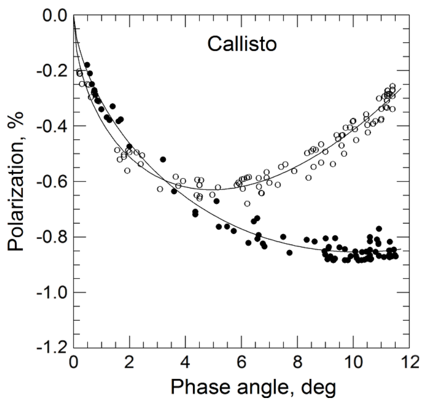

Figure 2: NPB for the leading (dark symbols) and trailing (open symbols) hemispheres of Callisto in the V filter after the correction for the orbital longitudinal variations [6]. Solid curves represent the best fit to the data by a trigonometric expression [7].

3.2 Saturn's moons: Enceladus, Dione, Rhea, and Iapetus

The NPBs for Enceladus, Dione, Rhea are plotted in Fig. 3. Enceladus is a unique object having the highest albedo ($p_v = 1.38$) of any object in the solar system. Moreover, Enceladus shows the ice fountains over the south polar region. Data for NPB of Enceladus are still rather limited because they are obtained for the first time. The asymmetric NPBs with polarization minima $P_{min} \approx -0.8\%$ at $\alpha_{min} \approx 1.8°$ are observed for Rhea and Dione. The NPB for Rhea is more sharp asymmetric than that for Diona.

Iapetus is a unique moon of Saturn with the greatest albedo asymmetry of any object in the Solar System. Its leading hemisphere has albedo $p_v = 0.02$–0.05, whereas the trailing hemisphere has $p_v = 0.6$. As a result, the large variations of polarization degree with longitude of Iapetus are revealed. In Fig. 4 we present the observations obtained for the bright trailing hemisphere (open symbols) as well as for the leading hemisphere (dark symbols). As one can see (Fig. 4, left panel), a strongly asymmetric phase curve of polarization for the bright trailing hemisphere with minimum $P_{min} \approx -0.7\%$ at $\alpha_{min} \approx 1.5°$ is revealed. The PLE for Iapetus is shown in Fig. 4 (right bottom panel). It is in a good agreement with the albedo distribution (Fig. 4, right upper panel) which is derived from a mosaic of Cassini images [9].

3.3 The major moons of Uranus: Ariel, Titania, Oberon, and Umbriel

Observations of the satellites were carried out at the 6 m BTA telescope [4] within the phase angle range of 0.06 – 2.37°. The NPB for Ariel, Titania, Oberon, and Umbriel in the V filter are presented in Fig. 5 (left panel). For Ariel, the maximum branch depth $P_{min} \approx -1.4\%$ is reached at the phase angle $\alpha_{min} \approx 1°$; for Titania $P_{min} \approx -1.2\%$, $\alpha_{min} \approx 1.4°$; for Oberon $P_{min} \approx -1.1\%$, $\alpha_{min} \approx 1.8°$.

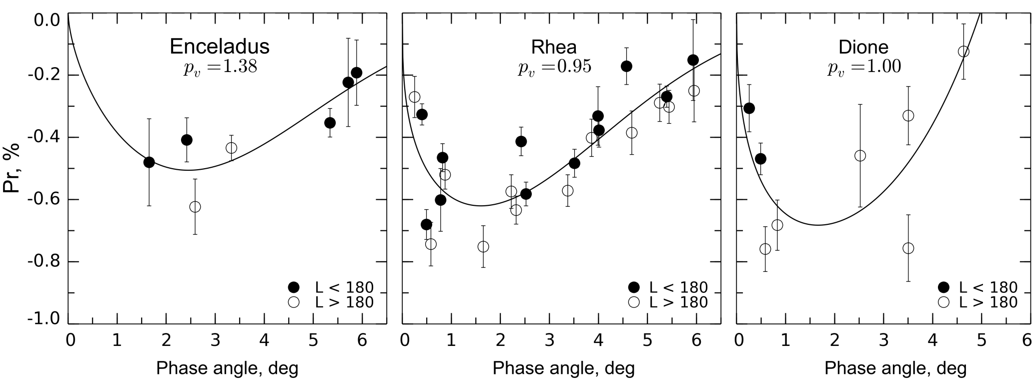

Figure 3: NPB for Enceladus, Rhea, and Dione. Dark and open circles show data for leading ($L < 180°$) and trailing ($L > 180°$) hemispheres, respectively. Solid curves represent the fit to the data by a trigonometric expression [7].

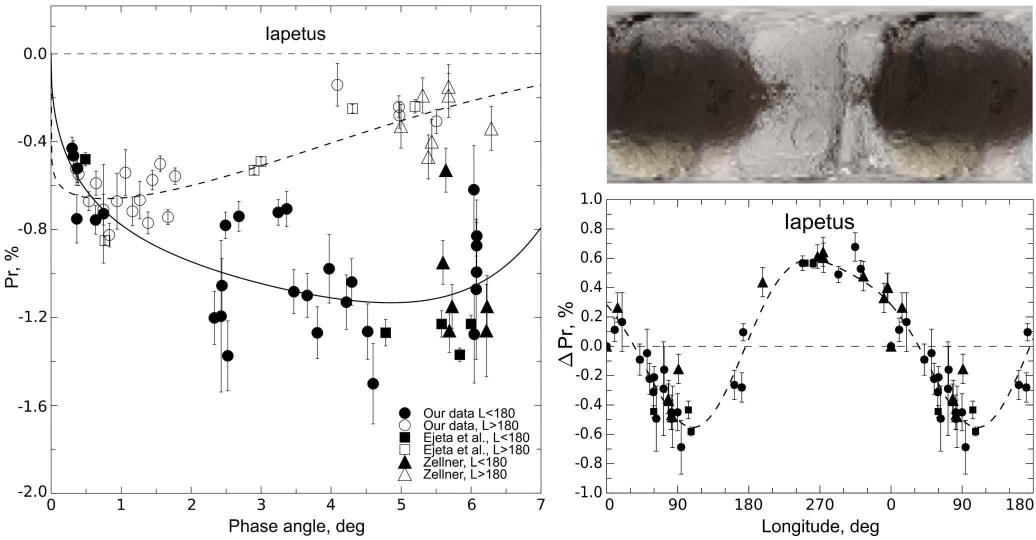

Figure 4: Phase-angle (left panel) and longitude (right bottom panel) dependencies of polarization for Iapetus. The albedo distribution map [9] is given in the right upper panel. Circles show our data, filters R and WR; squares data from [10, 11], filter R; triangles data by Zellner [12, 13], filter V.

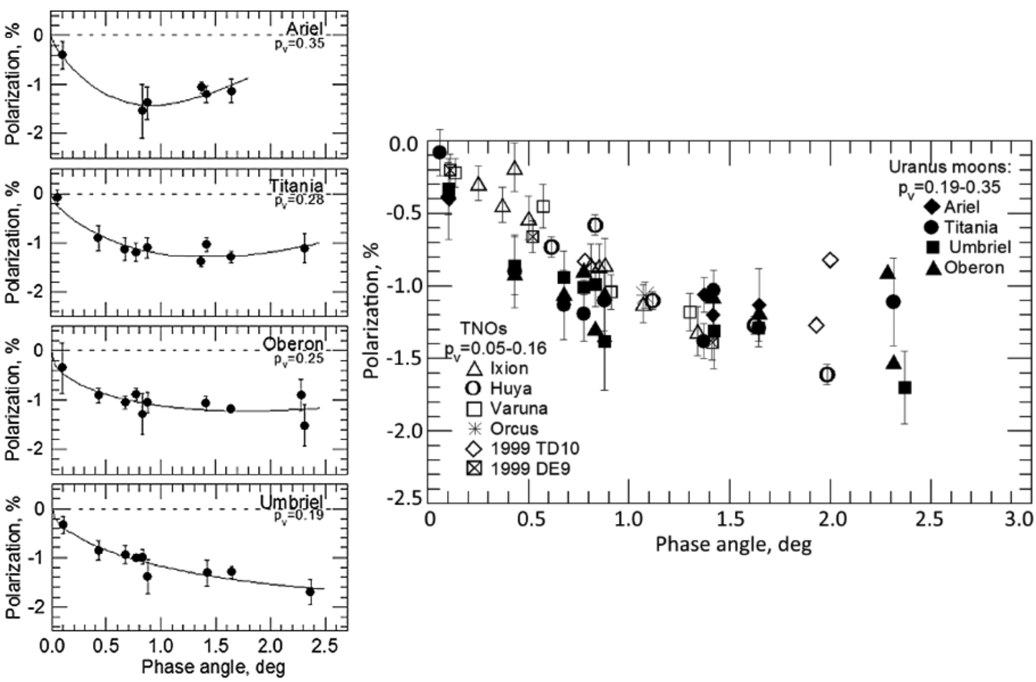

Figure 5: NPB for the Uranian satellites (left panel). Right panel shows a comparison of the phase-angle polarization dependencies of the Uranian moons (dark symbols) and TNOs (open symbols). Data for TNOs are taken from [14].

For Umbriel, the polarization minimum was not reached: for the last measurement point at $\alpha = 2.4°$, polarization amounts to -1.7%. The declining P_{min} and shifting α_{min} towards larger phase angles correlate with a decrease of the geometric albedo of the Uranian moons. There is no longitudinal dependence of polarization for the moons within the observational errors which indicates a similarity in the physical properties of the leading and trailing hemispheres [4].

We found (see Fig. 5, right panel) that for the Uranian moons the polarization phase dependencies are in a good agreement with the measured polarization of the group of small trans-Neptunian objects (Ixion, Huya, Varuna, Orcus, 1999 TD10, 1999 DE9) which are characterized by a large gradient of negative polarization, approximately 1% per degree in the $0.1-1°$ range of phase angles, according to [14].

4 Summary

The extensive polarimetric observations of moons of the outer planets, obtained during the past two decades, demonstrate that the behavior of the phase-angle dependence of polarization near the opposition is highly various. It is ranging from a bimodal curve consisting of a secondary minimum distinctly separated from the main minimum of the NPB (the Galilean satellites of Jupiter) to an asymmetric negative polarization branch (Saturn's and Uranian satellites). A quantitative analysis of these observational data in terms of specific physical parameters is hardly possible at this time because of the still limited data (limited range of phase angles and wavelengths). Nevertheless the data can be qualitatively interpreted in terms of the currently available light scattering mechanisms on the regolith surfaces. Shadow hiding, coherent backscattering, near-field effects, and anisotropic scattering by single particles are often considered as the dominant mechanisms that define the characteristics of the scattered radiation (intensity and polarization) at small phase angles. The shape of the NPB, as well as characteristics of BOE and POE, depend on the relative contributions of the mentioned mechanisms which, in turn, depend on the physical characteristics of the regolith layer and the scattering geometry. The packing density and the refractive index, as well as size and shape of the monomers constituting the aggregate particles, determine the effectiveness of each of the scattering mechanisms and, hence, the behavior of brightness and polarization near the opposition. This is what draws significant interest in the study of light scattering effects on surfaces of ASSBs, including planetary satellites, in terms of both observations and their modeling and development of light scattering theory.

References

1. *V. Rosenbush, N. Kiselev, V. Afanasiev*, in Polarimetry of Stars and Planetary Systems. Eds. L. Kolokolova, J. Hough, A.-Ch. Levasseur-Regourd. Cambridge: Cambridge Univ. Press, 2015, p. 340.

2. *M.I. Mishchenko, V.K. Rosenbush, N.N. Kiselev et al.*, Polarimetric Remote Sensing of Solar System Objects. Kyiv: Akademperiodika, 2010.

3. *V.L. Afanasiev, V.R. Amirkhanyan*, Astrophys. Bull., **67**, 438, 2012.
4. *V.L. Afanasiev, V.K. Rosenbush, N.N. Kiselev*, Astrophys. Bull., **69**, 121, 2014.
5. *A. Dollfus*, Icarus, **25**, 416, 1975.
6. *V.K. Rosenbush*, Icarus, **159**, 145, 2002.
7. *K. Lumme, K. Muinonen*, in Proc. IAU Symp. 160: Asteroids, Comets, Meteors. LPI Contrib. No. 810. Houston: Lunar Planet. Inst., 1993, p. 194.
8. *M.I. Mishchenko*, Astrophys. J., **411**, 351, 1993.
9. *S. Albers*, *http://laps.noaa.gov/albers/sos/saturn/iapetus/*
10. *C. Ejeta, H. Boehnhardt et al.*, Astron. Astrophys., **537**, A23, 2012.
11. *C. Ejeta, H. Boehnhardt et al.*, Astron. Astrophys., **549**, A61, 2013.
12. *B.H. Zellner*, Astrophys. J. Lett., **174**, L107, 1972.
13. *J. Veverka*, in Planetary satellites. Ed. J.A. Burns. Tucson: Univ. Arizona Press, 1977, p. 210.
14. *S. Bagnulo, I. Belskaya, K. Muinonen et al.*, Astron. Astrophys., **491**, L33, 2008.

Modeling of Spectral Variability of Romano's Star

O.V. Maryeva[1], V.F. Polcaro[2], C. Rossi[3], R.F. Viotti[2]

E-mail: *olga.maryeva@gmail.com*

The variable star GR 290 (M33/V532, Romano's Star) in the M 33 galaxy has been suggested to be a very massive star in the post-luminous blue variable (LBV) phase. In order to investigate links between this object, the LBV category and the Wolf-Rayet stars of the nitrogen sequence (WN), we have derived its basic stellar parameters and their temporal evolution. We confirm that the bolometric luminosity of the star has not been constant, it changes synchronously with stellar magnitude, being 50% larger during visual light maxima. Presently, GR 290 falls in the H-R diagram close to WN8h stars, being probably younger than them. In the light of current evolutionary models of very massive stars, we find that GR 290 has evolved from a 60 $M_\odot$ progenitor star and has an age of about 4 million years. From its physical characteristics, we argue that GR 290 has left the LBV stage and is presently moving from the LBV stage to a Wolf-Rayet stage of a late nitrogen spectral type.

1 Introduction

GR 290 was discovered as a variable star in 1978 by Giuliano Romano [1] and later classified by him as a Hubble–Sandage variable [2]. Peter Conti in 1984 merged Hubble-Sandage variables with S Dor variables in a united class – Luminous Blue Variables (LBVs), and GR 290 became a candidate LBV [3, 4]. Arguments for changing the class of GR 290 from candidate LBV to LBV were given in [5, 6, 7]. More detailed history of spectral and photometric investigations of GR 290 was described in [8].

However, in 2011 Polcaro et al. [9] suggested that, because of its very high luminosity and its extremely hot spectrum at the 2008 visual minimum (WN8h), GR 290 is probably not too far from the end of the LBV phase and may be evolving towards a late-WN-type star. In 2014 Humphreys et al. [10] also noticed that in recent years (2004–2010) GR 290 has shown large photometric variability of 1.5 mag in the blue, but no spectroscopic transition from a hot star spectrum (at the visual minimum) to the cool optically thick wind one at the visual maximum resembling an A to F-type supergiant that is typical of the LBV/S-Dor phenomenon. On the contrary, the spectrum of GR 290 varied from WN8h

[1] Special Astrophysical Observatory of the RAS, Russia
[2] INAF-IAPS, Italy
[3] Università La Sapienza, Italy

V. Grinin et al. (eds) Radiation mechanisms of astrophysical objects. Yerevan: Edit Print, 2017, pp. 211–214.

at minimum to WN11h at the recent visual maxima and to B, probably late type at its highest recorded maximum. In this regard, Humphreys et al. [10] speculate on whether GR 290 is a hot star in transition to the LBV stage (as suggested by Smith and Conti [11], for the WNh stars) or it may be in a post-LBV state.

Maryeva and Abolmasov [12] investigated the optical spectra of Romano's star in two different states: the brightness minimum of 2008 ($B = 18.5 \pm 0.05$ mag) and a moderate brightening in 2005 ($B = 17.1 \pm 0.03$ mag). Main result of the work [12] is that the bolometric luminosities (L_{bol}) of GR 290 were different in 2005 and 2008. L_{bol} of GR 290 in 2005 is 1.5 times higher, that is not typical of LBVs. This result confirms the suggestion of [9]. However, to refine the evolutionary status of the star, a more detailed investigation of intermediate states was also necessary, and in the present work we report on the results of such investigation.

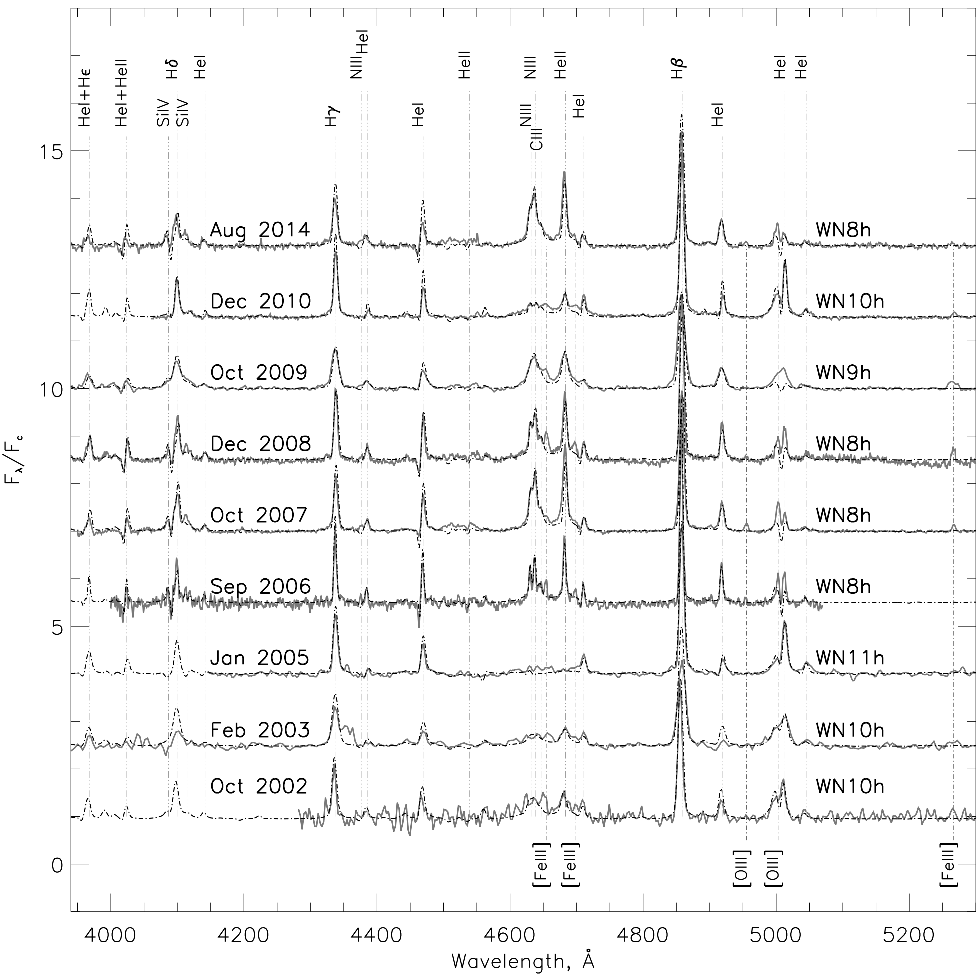

Figure 1: Normalized optical spectra of GR 290 compared with the best-fit CMFGEN models (dash-dotted line). The model spectra are convolved with a Gaussian instrumental profile.

Table 1: Derived properties of Romano's star. $R_{2/3}$ is the radius where the Rosseland optical depth is equal to 2/3, T_{eff} is the effective temperature at $R_{2/3}$, $\dot{M}_{cl}$ is the mass loss rate. For all models, we included clumping with the filling factor 0.15. For all dates, uncertainty of T_{eff} is 1 kK.

Date	V [mag]	Sp. type	T_{eff} [kK]	$R_{2/3}$ [$R_\odot$]	L_*, 10^5 [$L_\odot$]	$\dot{M}_{cl}$, 10^{-5} [$M_\odot \mathrm{yr}^{-1}$]	v_∞ [km/s]
Oct 2002	17.98	WN10h	28	39	8 ± 0.5	2.4 ± 0.3	250 ± 100
Feb 2003	17.70	WN10.5h	27.5	44	10.2 ± 0.7	2.6 ± 0.3	250 ± 50
Jan 2005	17.24	WN11h	23.5	61	$10.5^{+1.5}_{-3}$	4.0 ± 0.3	250 ± 50
Sep 2006	18.4	WN8h	31	28	6.7 ± 0.5	1.5 ± 0.3	250 ± 100
Oct 2007	18.6	WN8h	33.3	23.8	6.3 ± 0.5	1.9 ± 0.3	370 ± 50
Dec 2008	18.31	WN8h	31.5	28.5	7.2 ± 0.5	2.3 ± 0.3	370 ± 50
Oct 2009	18.36	WN9h	32	28.4	7.5 ± 0.5	2.0 ± 0.3	300 ± 100
Dec 2010	17.95	WN10h	26.7	42	8 ± 0.5	2.6 ± 0.3	250 ± 100
Aug 2014	18.74	WN8h	33	22.5	5.3 ± 0.5	1.7 ± 0.3	400 ± 100

2 Modeling

In order to see how the parameters of GR 290 changed with time, we modeled the most representative spectra with best quality obtained during October 2002 – December 2014, when the star displayed an ample range of variation in visual luminosity. This time interval covers two brightness maxima and three minima. For modeling we used CMFGEN atmospheric code [13] and constructed nine models (Fig. 1). We can see from Table 1 that the nature of the stellar wind significantly changes, being much denser and slower during the eruption in 2005, while during the minimum of brightness wind structure is fairly similar to the one of typical WN8h (non variable) stars.

The main result of this analysis is that the bolometric luminosity of GR 290 is variable, it is higher during the phases of greater optical brightness. The present model fitting of a large sample of spectra obtained during two successive luminosity cycles allows us to trace the recent path of the star in the Hertzsprung–Russell (H-R) diagram (Fig. 2).

3 Results

Combining the results of numerical modeling with data of photometric and spectral monitoring, we may conclude that we observed GR 290 in very rare evolutionary phase – post-LBV. The initial mass of GR 290 is near 60 $M_\odot$ and age is about 4 Myr. Probably, the changes of L_{bol} are due to the hydrogen mixing in the core generating a burst of nuclear energy: presently, such repeated nuclear events should be the extra-energy input to increase the bolometric luminosity of GR 290 during its last outbursts. They will end when the hydrogen percentage in the envelope will become too low to be mixed in the core.

More details are published in [14].

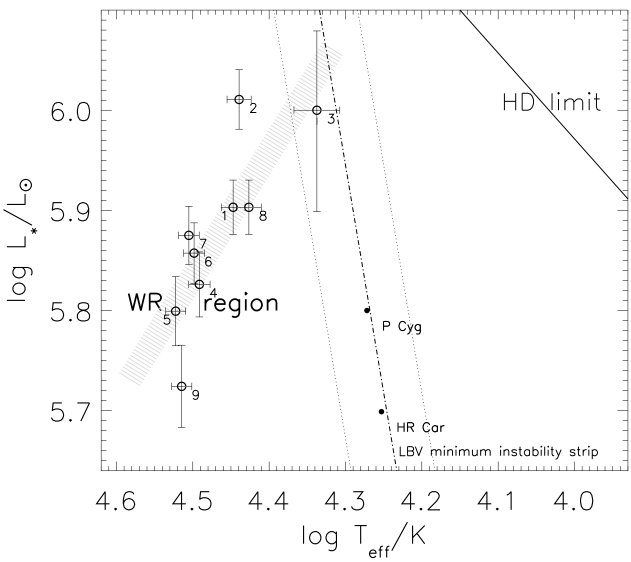

Figure 2: Position of GR 290 in the H-R diagram. HD limit line shows the Humphreys–Davidson limit [3]. 1 – Oct. 2002; 2 – Feb. 2003; 3 – Jan. 2005; 4 – Sep. 2006; 5 – Oct. 2007; 6 – Dec. 2008; 7 – Oct. 2009; 8 – Dec. 2010; 9 – Aug. 2014.

Acknowledgments. The authors would like to thank R. Gualandi, R. Haver and M. Calabresi for providing with new spectral and photometric data. O.M. thanks RFBR (project 14-02-00291) for a support.

References

1. *G. Romano*, Inf. Bull. Var. Stars, No. 1433, 1978.
2. *G. Romano*, Astron. Astrophys., **67**, 291, 1978.
3. *R.M. Humphreys, K. Davidson*, Publ. Astron. Soc. Pacif., **106**, 1025, 1994.
4. *T. Szeifert*, Liege Int. Astrophys. Coll., **33**, 459, 1996.
5. *R. Kurtev, O. Sholukhova et al.*, Rev. Mex. Astron. Astrofiz., **37**, 57, 2001.
6. *V.F. Polcaro, R. Gualandi, L. Norci et al.*, Astron. Astrophys., **411**, 193, 2003.
7. *S. Fabrika, O. Sholukhova, T. Becker et al.*, Astron. Astrophys., **437**, 217, 2005.
8. *O. Maryeva*, Balt. Astron., **23**, 248, 2014.
9. *V.F. Polcaro, C. Rossi, R.F. Viotti et al.*, Astron. J., **141**, 18, 2011.
10. *R.M. Humphreys, K. Weis, K. Davidson et al.*, Astrophys. J., **790**, 48, 2014.
11. *N. Smith, P.S. Conti*, Astrophys. J., **679**, 1467, 2008.
12. *O. Maryeva, P. Abolmasov*, Mon. Not. Roy. Astron. Soc., **419**, 1455, 2012.
13. *D.J. Hillier, D.L. Miller*, Astrophys. J., **496**, 407, 1998.
14. *V.F. Polcaro, O. Maryeva, R. Nesci et al.*, Astron. J., **151**, 149, 2016.

Magnetic Field Function for Early-Type Stars

A. Medvedev[1], A. Kholtygin[2]

E-mail: *a.s.medvedev@gmail.com*

We present a model describing the magnetic field function for early-type stars. The model relies on population synthesis to generate the ensemble of magnetic stars on the upper main sequence. It also includes the capabilities for statistical simulations and parameter estimation necessary for analysis of real data. Our model was able to reproduce the empirical magnetic field distributions for OBA stars. We estimated the model parameters, found constraints on dissipation of stellar magnetic fields and explored the hypothesis that magnetic properties of early-type stars (2–60 $\mathrm{M}_{\odot}$) might be described by a single magnetic field function.

1 Introduction

Magnetic stars on the upper main sequence (upper MS) are particularly interesting for research. All of the theories proposed to explain the origin of the large-scale magnetic fields are closely related to our understanding of early stages of the pre-MS evolution and formation of intermediate-mass and massive stars [12]. Moreover, although these stars are the progenitors of isolated pulsars, their magnetic properties are not interrelated directly, but strongly suggest the evolution of the magnetic fields between the zero-age main sequence (ZAMS) and supernova explosion [7].

Potentially, a lot of information that might be vital for our understanding of stellar magnetism should be gained from the study of the distributions of the stellar magnetic fields. The great increase in the number of known magnetic stars [5, 13] that happened over the last decades, including the discovery of the magnetic O-type stars, provides us with the opportunity to study such distributions even for different groups of OBA stars [8]. It also opened the possibility to check some of the early hypotheses about properties of the stellar magnetic fields in the light of recently acquired data.

For these purposes, we model the magnetic field function for early-type stars. We create a tool that would be useful for analysis of the empirical magnetic field distributions. Our model is based on population synthesis to account for the diversities in stellar parameters that always will exist in real samples of magnetic stars. It is also able to simulate the magnetic field distribution for a sample of a given size and, what is important, to estimate the magnitude of its possible variations.

[1] Special Astrophysical Observatory, Nijnii Arkhyz, Russia
[2] St. Petersburg State University, Russia

V. Grinin et al. (eds) Radiation mechanisms of astrophysical objects. Yerevan: Edit Print, 2017, pp. 215–218.

2 The model

The population synthesis begins with the initial ensemble containing stars that are randomly generated assuming the standard initial mass function [9] and a constant birth-rate. The temporal evolution of the ensemble is computed with the SSE code [6] implemented within the AMUSE environment for astrophysical simulations [10]. The evolution time is set to be large enough for the ensemble to achieve stationarity for a number of MS stars.

The magnetic fields corresponding to ZAMS stars are generated, assuming the lognormal distribution for the initial net magnetic flux, which is defined by the mean logarithm of the net magnetic flux $\langle \log \Phi \rangle$ and its deviation Δ. The evolution of stellar magnetic fields on the MS is represented by the exponential decay of the magnetic flux [8]. The process is described by the dissipation parameter τ_d that coincides with the relative time-scale for the decay, expressed in terms of a stellar MS lifetime. The ensemble generation is accomplished when the root-mean-square (rms) magnetic fields $\mathcal{B}$ for all objects in the ensemble of magnetic stars are finally computed.

The ensemble is then used to obtain the magnetic field function and its appearance for the sample of a given size. This involves random sampling and raw statistical methods for estimating of the mean distribution and limits for its possible variations (Fig. 1).

3 Empirical magnetic field distributions

We obtained the magnetic field distributions for BA, OB and O-type stars using data from different sources [2, 4, 11], and applied our model for their analysis.

We find that the empirical magnetic field distributions for BA and OB stars are very similar. They both reveal the same regular shape, typical of the lognormal distribution. In particular, the distribution for BA stars can be fitted by the

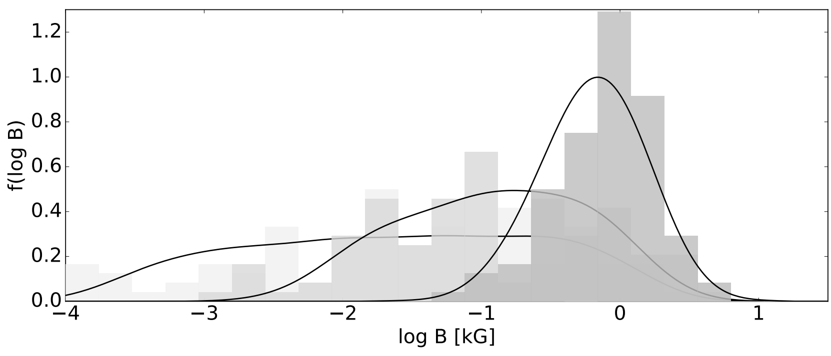

Figure 1: Magnetic field function for early-type stars calculated with our model. Black lines correspond to different values of the dissipation parameter τ_d: 0.15 (left curve), 0.3 (central curve) and ∞ (right curve). The gray histograms show the distribution for the same parameters, but for samples of $\sim$100 stars.

Table 1: Best-fit parameters obtained from the simultaneous approximation of the magnetic field distribution functions for BA, OB and O-type stars. The confidence intervals were obtained by using the C-statistics introduced by Cash [3]

Model	$\langle \log \Phi \rangle$, G cm^2	Δ	$\tau_{\rm d}$
I	$26.86^{+0.07}_{-0.21}$	$0.55^{+0.09}_{-0.13}$	∞
II	$27.23^{+0.11}_{-0.12}$	$0.38^{+0.1}_{-0.13}$	0.5

lognormal distribution with the mean $\langle \log \mathcal{B} \rangle \approx 0.5$ and the standard deviation $\sigma = 0.5$. It is inconsistent with the hypothesis of a "magnetic threshold" proposed by Aurière et al. [1] to explain the lack of stars with $B_d \lesssim 300$ G (or $\mathcal{B} \lesssim 60$ G), appeared in their sample. We found no peculiarities or other indications supporting this conjecture. A similar issue was also reported for OB stars in [5].

Also, we suppose that dissipation of the stellar magnetic fields is not very fast, otherwise we would expect very different appearances of the empirical distributions (Fig. 1). Our analysis shows that only for $\tau_{\rm d} \gtrsim 0.5$ it is possible to achieve the best agreement between the model and empirical distributions. This implies that the time-scales for magnetic field dissipation are at least comparable with the stellar MS lifetimes.

The sample of O-type stars consists of 11 stars only. Such a small size makes it difficult to draw reliable conclusions about the intrinsic magnetic field function. However, we assumed that the empirical distribution for O-type stars might also be drawn from the same magnetic field function as for BA and OB stars. Applying the procedure of simultaneous fitting, we were able to describe all of the empirical distributions with a single model (see Table 1). Therefore, it is not unlikely that magnetic properties of upper MS stars (with $M > 2$–$60\,\mathrm{M}_\odot$) are defined by a common magnetic field function.

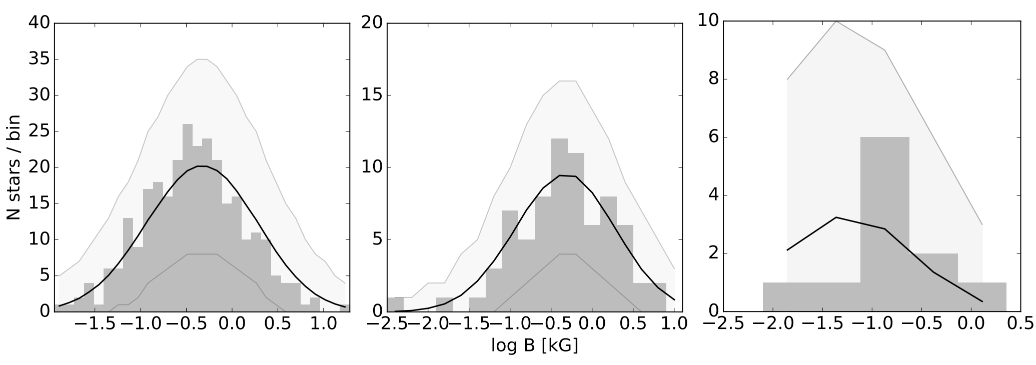

Figure 2: Simultaneous fitting of the magnetic field distributions for BA, OB and O-type stars (from left to right). The gray histograms represent the empirical data, while the black lines show the mean model distribution. The gray filled area corresponds to the 95% confidence limits for possible variations.

4 Conclusions

- We built a model describing distribution of magnetic fields for early-type stars and applied model for analysis of the empirical data.
- The empirical magnetic field distribution for BA and OB stars are very similar and both can be fitted by a lognormal distribution.
- It is possible to reproduce all of the empirical distributions with a single magnetic field function (Table 1).
- The estimated constraint on the dissipation parameter is $\tau_d \leq 0.5$, are in accordance with estimations by Kholtygin et al. [8].
- The empirical distributions for OBA stars provide with no evidence supporting the hypothesis of a "magnetic desert" [1].

Acknowledgments. The authors thank RFBR grant 16-02-00604a and RSF grant 14-50-00043 for the support.

References

1. *M. Aurière, G.A. Wade, J. Silvester et al.*, Astron. Astropys., **475**, 1053, 2007.
2. *V.D. Bychkov, L.V. Bychkova, J. Madej*, Mon. Not. Roy. Astron. Soc., **394**, 1338, 2009.
3. *W. Cash*, Astrophys. J., **228**, 939, 1979.
4. *L. Fossati, N. Castro, T. Morel et al.*, Astron. Astropys., **574**, A20, 2015.
5. *L. Fossati, N. Castro, M. Schöller et al.*, Astron. Astropys., **582**, A45, 2015.
6. *J.R. Hurley, O.R. Pols, C.A. Tout*, Mon. Not. Roy. Astron. Soc., **315**, 543, 2000.
7. *A.P. Igoshev, A.F. Kholtygin*, Astron. Nachr., **332**, 1012, 2011.
8. *A.F. Kholtygin, S.N. Fabrika, N.A. Drake et al.*, Astron. Lett., **36**, 370, 2010.
9. *P. Kroupa*, Science, **295**, 82, 2002.
10. *F.I. Pelupessy, A. van Elteren, N. de Vries et al.*, Astron. Astropys., **557**, A84, 2013.
11. *G.A. Wade*, Astron. Soc. Pacif. Conf. Ser., **494**, 30, 2015.
12. *R. Walder, D. Folini, G. Meynet*, Space Sci. Rev., **166**, 145, 2012.
13. *G.A. Wade, C. Neiner, E. Alecian et al.*, Mon. Not. Roy. Astron. Soc., **456**, 2, 2016.

Continuum and Line Emission of Flares on Red Dwarf Stars: Origin of the Blue Continuum Radiation

E.S. Morchenko[1]

E-mail: *morchenko@physics.msu.ru*

There are two types of models that explain the appearance of the quasi-blackbody radiation during the impulsive phase of stellar flares. Grinin and Sobolev [1] argue that this component of the optical continuum is formed in "the transition layer between the chromosphere and the photosphere." Katsova et al. [4] have "raised" the source of the white-light continuum up to the dense region in the perturbed chromosphere. In the present contribution (the main paper is published in "Astrophysics" [9]), we show that the statement in [4] is erroneous.

1 Introduction

Grinin and Sobolev [1] were the first who showed that the quasi-blackbody spectrum at the flare's maximum brightness is formed near the photosphere. Heating of the deep layers is due to the high energy proton or/and electron beams with the initial energy flux $F_0 \approx 10^{12}$ erg cm^{-2}s^{-1} and $F_0 \approx 3 \times 10^{11}$ erg cm^{-2}s^{-1}, respectively [2, 3].

Katsova et al. [4] calculated the first gas dynamic model of the impulsive stellar flares (the energy flux in the electron beam $F_0 = 10^{12}$ erg cm^{-2}s^{-1}). According to this model, the blue component of the optical continuum is formed in a chromospheric condensation. The condensation is located between a temperature jump and the front of the downward shock (the temperature wave of the second kind [5]). The physical parameters of this source of white-light continuum ($N_H \approx 2 \times 10^{15}$ cm^{-3}, $T \approx 9000$ K, and thickness $\Delta z \approx 10$km) lie in the range of the layer parameters in the model by Grinin and Sobolev [1] ($N_H \sim 10^{15} - 10^{17}$ cm^{-3}, $T \sim 5000 - 20000$ K, and $\Delta z \gtrsim 10$ km). Here, N_H is equal to the sum of the proton and atom concentrations. However, the condensation is formed at height of about 1500 km above the quiescent photosphere of a red dwarf, i.e. in the upper chromosphere.

The downward shock [4] propagates through *a partially ionized gas* of the red dwarf chromosphere. The flow speed is subsonic for the electron component of the plasma but this speed is hypersonic for the ion-atom component [6]. Therefore, both ions and atoms are heated more intensively than electrons

[1] Sternberg Astronomical Institute, Moscow M.V. Lomonosov State University, Russia

V. Grinin et al. (eds) Radiation mechanisms of astrophysical objects. Yerevan: Edit Print, 2017, pp. 219–221.

at the shock front. Thus, the region between the temperature jump and the front of the downward shock is, in fact, *two-temperature* ($T_{ai} \gg T_e$) [7]. Here, T_{ai} is the ion-atom temperature, and T_e is the electron one.

2 Emission spectrum of a two-temperature layer

Morchenko et al. [7] calculated the emission spectrum of a homogeneous pure hydrogen layer with $6\,\mathrm{eV} \leq T_{ai} \leq 12\,\mathrm{eV}$ and $0.8\,\mathrm{eV} \leq T_e \leq 1.5\,\mathrm{eV}$. The layer density lies in the range $3 \times 10^{14}\,\mathrm{cm}^{-3} \leq N_H \leq 3 \times 10^{16}\,\mathrm{cm}^{-3}$.

Initially, we assume that the Lyman-α optical depth in the center of the layer, τ_{12}^D, is approximately equal to 10^7 (see Eq. (1) in [7]). However, at values of $N_H \sim 10^{16}\,\mathrm{cm}^{-3}$ the layer thickness, $\mathcal{L}$, is *small* ($\tau_{12}^D \propto N_1\mathcal{L}$ – see Eq. (53) in [7]). Here, N_1 is the concentration of the ground state atoms. Therefore, we consider the transition from the transparent gas to the gas whose emission is close to the Planck function under conditions when $\mathcal{L}$ is fixed (see the first paragraph of Sect. 7 in [7]).

The following elementary processes were taken into account: the electron impact ionization, excitation, and de-excitation, the triple recombination, the spontaneous radiative recombination, the spontaneous transitions between discrete energy levels. We consider the influence of the layer's radiation (bremsstrahlung and recombination) on the occupation of atomic levels. It is necessary as the flare luminosity is stronger in the optical range than that of the quiescent atmosphere of the whole star.

We take into account the scattering of line radiation in the framework of the Biberman–Holstein approximation [8]. Since $\tau_{12}^D \gg 1$, photons escape the flare plasma in the distant line wings [7]. The following asymptotic formula is valid for the resonance transition:

$$\theta_{12} \approx \left(\frac{\mathcal{B}_{21}\mathcal{E}_0}{\Delta\omega_{21}^D}\right)^{3/5} \frac{1}{(\tau_{12}^D)^{3/5}}. \tag{1}$$

Here, $\mathcal{B}_{21}$ is the Stark broadening parameter, $\mathcal{E}_0$ is the Holtsmark field strength, and $\Delta\omega_{21}^D$ is the Doppler width.

Our calculations [7] have shown that the Menzel factors do not differ from unity at values of $\tau_{12}^D \sim 10^7$ and higher. Moreover, the two-temperature 10 km layer with $N_H = 3 \times 10^{16}\,\mathrm{cm}^{-3}$, $T_{ai} = 10\,\mathrm{eV}$, $T_e = 1\,\mathrm{eV}$ generates the blue continuum radiation (the optical depth at wavelength $\lambda = 4170$ Å, τ_{4170}, is approximately equal to 6).

We also *proposed* that the non-stationary radiative cooling of the gas behind the downward stationary shock can produce an equilibrium region, which is responsible for the quasi-blackbody radiation during the impulsive phase of stellar flares (the last sentence in [7]).

3 Origin of the blue continuum radiation

The model [4] includes the one-temperature ($T_{ai} = T_e = T$) source of the white-light continuum. Let us investigate the applicability of the calculations [7] for a one-temperature layer with $\tau_{12}^D \gtrsim 10^7$. It is true that

$$\tau_{12}^D \propto \frac{1}{\sqrt{\pi}\Delta\omega_{21}^D} \propto {T_{ai}}^{-1/2}. \tag{2}$$

Therefore, the mean photon escape probability, θ_{12}, as well as the Menzel factors of the layer do not depend on the ion-atom temperature. Thus, at $T_e = T_{ai} = T$ numerical results [7] remain valid.

Then it is true that the 10 km layer with the parameters from the model by Katsova et al. [4] is *transparent* in the optical continuum (see the lower curve designated to "I" in Fig. 2 from [7]): $\tau_{4170} \ll 1$, Q.E.D.

In the paper [9] we briefly discuss the theoretical possibility of the origin of the blue continuum radiation behind the downward stationary shock with *radiative cooling*. Based on a simple estimate, it is shown that the Planck emission is formed only under conditions when the gas flows from the viscous jump on a small distance (approximately five hundred meters). Thus, our hypothesis [7] is not confirmed.

Finally, we hold that the quasi-blackbody spectrum during the impulsive phase of stellar flares is formed in the deep layers [1, 10].

References

1. *V.P. Grinin, V.V. Sobolev*, Astrophys., **13**, 348, 1977.

2. *V.P. Grinin, V.V. Sobolev*, Astrophys., **31**, 729, 1989.

3. *V.P. Grinin, V.M. Loskutov, V.V. Sobolev*, Astron. Rep., **37**, 182, 1993.

4. *M.M. Katsova, A.G. Kosovichev, M.A. Livshits*, Astrophys., **17**, 156, 1981.

5. *P.P. Volosevich, S.P. Kurdyumov, L.N. Busurina, V.P. Krus*, Comput. Math. Math. Phys., **3**, 204, 1963.

6. *S.B. Pikel'ner*, Izv. Krym. Astrofiz. Obs., **12**, 93, 1954.

7. *E. Morchenko, K. Bychkov, M. Livshits*, Astrophys. Space Sci., **357**, article id. 119, 2015.

8. *V.V. Ivanov*, Transfer of Radiation in Spectral Lines. Washington: Nat. Bur. Stand., 1973.

9. *E.S. Morchenko*, Astrophys., **59**, 475, 2016.

10. *S.W. Mochnacki, H. Zirin*, Astrophys. J. Lett., **239**, L27, 1980.

Optical Continuum of Powerful Solar and Stellar Flares

B.A. Nizamov[1], M.A. Livshits[2]

E-mail: *nizamov@physics.msu.ru, maliv@mail.ru*

The powerful optical continuum of solar and stellar flares is hard to explain within the concept of the gasdynamic response of the chromosphere to the impulsive heating. It requires too large amount of accelerated particles, in contradiction with the hard X-ray observations. The resolution of this trouble is to take into account the absorption of the short wavelength radiation of the hot flaring plasma by the optical emission source, i.e. the low temperature condensation. Our estimates show that this can help to explain the origin of the optical continuum of powerful impulsive flares on the Sun and red dwarfs and superflares on the young G stars.

1 Introduction

A large amount of the multi-wavelength observations of solar flares as well as the optical and X-ray observations of flares on red dwarfs have been analysed in the last years; non-stationary events with the total energy exceeding that of the most powerful phenomena on the Sun by 2–3 orders of magnitude were detected on some late-type low-mass stars by the *Kepler* spacecraft. This required a new analysis of the data on the stellar flares. Particularly, this refers to the possibility of the generation of the powerful continuous optical radiation of the superflares.

Theoretical investigation of the problem concerning the flares on red dwarfs was carried out in a series of papers by Grinin and Sobolev [8, 9, 10, 11].

It is clear that the heating by the accelerated particles, mainly electrons, should be accompanied by the gasdynamic motions. This dynamic response of the dense layers of the atmosphere was considered for the first time by Kostiuk and Pikelner [13] and later was considered in a numerous number of papers dedicated to the flares on the Sun and the stars [14, 7, 6, 2, 12, 3].

The optical emission in the gasdynamic model is known to originate in the dense low-temperature condensation between the front of the downward moving shockwave and the heating front. The plot of the density $n = n_{\mathrm{H\,I}}+n_{\mathrm{H\,II}}$ for several instants of a powerful solar flare is given in the left panel of Fig. 1. The density is seen to reach quite high values of the order 10^{15} cm^{-3} in a time of about 10 s.

[1] Sternberg State Astronomical Institute, Lomonosov Moscow State University, Russia
[2] Pushkov Institute of Terrestrial Magnetism, Ionosphere and Radiowaves Propagation (IZMIRAN), Russia

V. Grinin et al. (eds) Radiation mechanisms of astrophysical objects. Yerevan: Edit Print, 2017, pp. 223–228.

Although the aforementioned theoretical works were confirmed by the observations in various aspects, it still remains unclear: are such models able to account for the optical continuum arising in powerful flares on the Sun (and the stars)? In the present work an attempt is made to answer this question and find the conditions for the optical continuum in a flare to arise.

2 Method of solution

In the gasdynamic model the optical radiation arises in a peculiar low-temperature gas condensation. Can the radiation of the condensation give a contribution to the continuum? In order to answer this question, we made use of the calculation [2]. This *gasdynamic* calculation provides the gas density, the temperature, the ionization degree and some other parameters as functions of the column density ξ [cm^{-2}] (the gas is assumed to be pure hydrogen). In the right panel of Fig. 1 the thin solid line represents the electron density in the condensation (other lines will be explained later).

The lower boundary of the condensation (the right one in the figure) is a shock wave through which the undisturbed gas flows into the condensation and heats. This explains the high ionization at the lower boundary. The condensation is limited from above by the hot gas which also heats it due to the thermal conductivity. This explains the high ionization at the upper boundary. The ionization is low in the middle part of the condensation.

Given the density, the temperature and the electron number density, one can calculate the spectrum of the radiation emerging from the condensation. We performed such a calculation by the method described in [15], namely we solved the equations of radiative transfer and statistical equilibrium in the condensation

$$\mu \frac{dI_\nu}{d\tau_\nu} = I_\nu - S_\nu, \tag{1}$$

$$\sum_{j\neq i} n_i R_{ij} = \sum_{j\neq i} n_j R_{ji}. \tag{2}$$

It turned out that such a condensation gives no contribution to the continuum. However, it should be noted that the system of equations solved in [2] did not include either the equations of statistical equilibrium or the charge conservation law. Therefore, after solving the equations (1)–(2), it may turn out that the ion density is not equal to the electron density, i.e. the electroneutrality of the medium may be violated. And this is actually the case. In the right panel of Fig. 1 the thin solid line represents the electron density in the condensation which was taken from the gasdynamic calculation, and the dashed line represents the ion density which is obtained from the solution of the equations (1)–(2). In order to enforce the electroneutrality, one should add one more equation to the system, namely:

$$n_p = n_e, \tag{3}$$

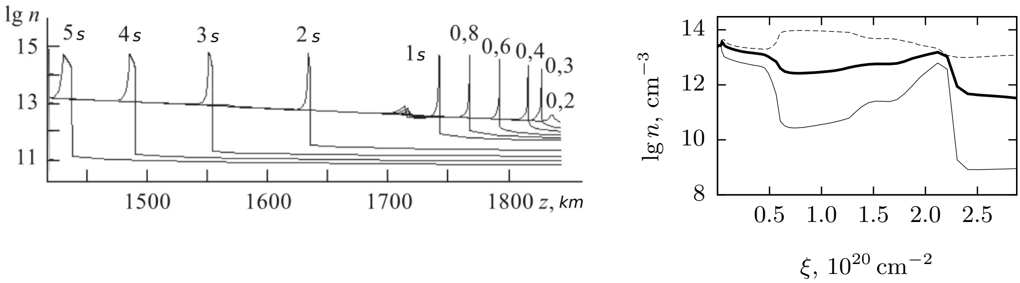

Figure 1: *Left.* The response of the solar atmosphere to the impulsive heating by the non-thermal electrons with the energy flux 10^{11}erg/cm^2/s and sufficiently hard spectrum which corresponds to a powerful solar flare [3]. *Right.* Thin solid line: electron number density in the gasdynamic model. Dashed line: corresponding number density of the ions. Thick solid line: electron and ion number density in case of electroneutrality concerned. The column density ξ is counted from the top of the condensation.

and the electron density should be calculated from the new system of equations instead of being taken from the gasdynamic model. The plot of the electron number density obtained in such a way is represented in the right panel of Fig. 1 by the thick solid line. It is clear from the comparison of this line with the thin solid one that the gasdynamic calculation tends to underestimate the electron density along with the optical depth of the gas in the continuum. Hence, the amount of the continuous radiation is also decreased.

Concerning the impossibility of explaining the optical continuum, we draw attention to one more factor which was not taken into account in [2], namely the irradiation of the condensation by the short-wavelength emission of the hot plasma filling the magnetic loop during the flare. This plasma has the temperature of the order 10^7 K and radiates in XEUV and SXR spectral regions. For a M2 class flare one can use the differential emission measure (DEM) provided by the CHIANTI package [5, 4]. Unfortunately, analogous data for the most powerful solar flares are absent for different reasons, therefore we assumed that for such flares the DEM(T) is an order of magnitude larger than that given in CHIANTI for a M2 class flare and calculated the spectrum of the gas with the density 10^9 cm^{-3} (Fig. 2). Note that this is the spectrum of the coronal gas only, therefore the flux in the He II 304 Å line can be underestimated.

First of all let us consider a simplified problem. Suppose there is a layer of hydrogen of a finite width with a given density and temperature (we call this temperature "initial"). The layer is irradiated by the photosphere. Moreover, in the layer there are artificial sources of heat which, along with the photospheric radiation and the radiation of the layer itself, maintain the given (initial) temperature. These artificial sources are introduced in order not to consider the evolution of the whole process in time, but instead to use the gasdynamic solution (or its analogue) for a certain instant. In other words, we replace the non-stationary problem with a stationary one. It is justified since beginning with approximately the time of 2 s, the evolution of the condensation is

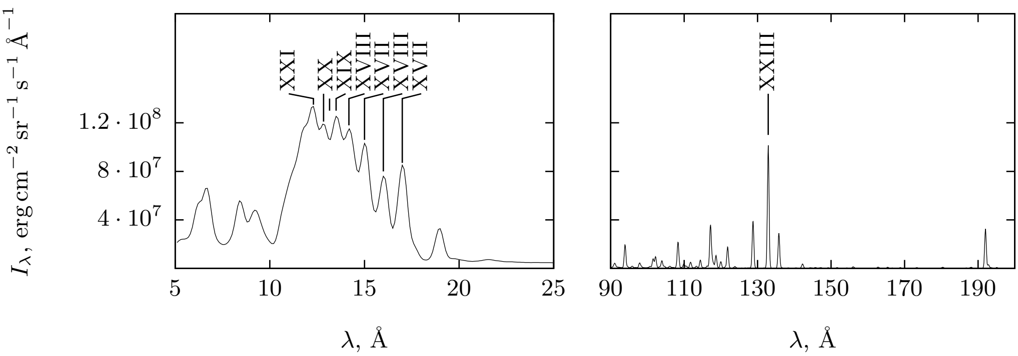

Figure 2: Two parts of the spectrum of the hot flaring plasma. The numbers indicate the ionization stage of the iron atom emitting the relevant line.

essentially quasi-stationary and its structure changes little with time (of course, up to a certain time). In fact, the parameters of the condensation depend on the time. In particular, the temperature is determined by the equation of energy. But taking into account the above consideration, we eliminate the dependence on the time, and in order to maintain the temperature at a given level, we introduce the artificial heat sources. Thus, we assume the validity of the condition of radiative equilibrium with the additional heat source in the layer. This condition takes the form

$$4\pi \int \eta_\nu d\nu = q + \int d\Omega \int I_\nu \chi_\nu d\nu, \tag{4}$$

where η_ν, χ_ν are the emissivity and opacity, and q is the power of the artificial sources. From this relation we find the power of the artificial sources

$$q = 4\pi \int \eta_\nu d\nu - \int d\Omega \int I_\nu \chi_\nu d\nu. \tag{5}$$

So, solving the equations (1)–(4) with the numerical values of q found from the equation (5), we obtain the populations of the atomic levels, the ionization degree and the temperature in the condensation, the latter being equal to the initial temperature. Now in order to take into account the X-ray source, we have to solve the equations (1)–(4) with *the same* sources q, but the upper boundary condition in the equation of radiative transfer should correspond to the X-ray emission falling on the condensation from above. As a result, we obtain the new populations, ionization degree and the new temperature which is higher than the initial one. We also calculate the spectrum of the radiation emerging from the condensation and can compare it with the spectrum of the quiet Sun to see if any additional continuum arises in the condensation and how large it is. Let us compare the specific intensity at the disc center of the radiation emerging from the condensation I_c and the radiation of the

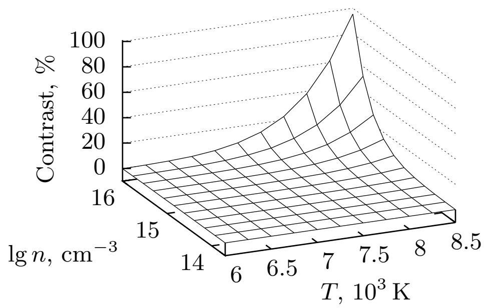

Figure 3: Contrasts in per cents for various values of the density and temperature of the condensation.

photosphere $I_{\rm p}$ at the wavelength 4500 Å. Let us term the quantity $(I_{\rm c} - I_{\rm p})/I_{\rm p}$ the contrast.

In our calculations we represent the condensation as a finite homogenous layer of the width 50 km as in the gasdynamic solution. The density and the initial temperature are varied in the ranges from 5×10^{13} to 10^{16} cm^{-3} and from 6000 to 8500 K, respectively. The plot of the contrasts is shown in Fig. 3.

It is seen that the high contrasts (>10%) are reached only at high densities ($\sim 10^{15}$ cm^{-3}) and temperatures ($\sim$8500 K).

Taking into account the external radiation in the gasdynamic response of the chromosphere to the heating should change the physical conditions inside the condensation. Namely, at the beginning of the process, when the condensation is tenuous, the external radiation should prevent the strong cooling (and hence the decrease of the ionization degree) in the middle of the condensation. But by the end of the non-thermal particle heating (approximately in 10 s after the onset of the response) the condensation would propagate quite deep and its density would increase while the temperature throughout it would still be high due to the "preliminary" heating by the X-rays. This provides the generation of the optical continuum. In other words, the optical thickness of the condensation at the wavelength 4500 Å becomes $\gtrsim 0.03$.

3 Conclusions

The general idea of the relation between the origin of the optical continuum and the impact of the accelerated particles on the atmosphere which was put forward by Grinin and Sobolev is of current interest. The further development of the gasdynamic model with account of the absorption of the short-wavelength radiation is desired. Following this way may probably help to understand the emergence of the powerful optical continuum. Note that the radiation of the condensation is most likely related to the blue continuum whereas the lower-temperature red continuum can arise as a consequence of the irradiation of the upper photosphere by the soft X-rays from the large cloud of the hot plasma which forms during a flare (as it is stated in [1]).

Acknowledgments. We thank Farid Goryaev for his help with CHIANTI. This work was partially supported by Russian Foundation for Basic Research (grants No. 14-02-00922 and 15-02-06271) and by the grant from Russian Federation President supporting Leading Scientific Schools 1675.2014.2.

CHIANTI is a collaborative project involving the following Universities: Cambridge (UK), George Mason and Michigan (USA).

References

1. *J.C. Allred*, *A.F. Kowalski*, *M. Carlsson*, Astrophys. J., **809**, 104, 2015.
2. *A.Ya. Boiko*, *M.A. Livshits*, Astron. Rep., **39**, 338, 1995.
3. *A.Ya. Boiko*, *M.A. Livshits*, Astrophys. Space Sci., **274**, 299, 2000.
4. *G. Del Zanna*, *K.P. Dere*, *P.R. Young*, *E. Landi*, *H.E. Mason*, Astron. Astrophys., **582**, A56, 2015.
5. *K.P. Dere*, *J.W. Cook*, Astrophys. J., **229**, 772, 1979.
6. *A.G. Emslie*, Solar Phys., **121**, 105, 1989.
7. *G.H. Fisher*, *R.C. Canfield*, *A.N. McClymont*, Astrophys. J., **289**, 414, 1985.
8. *V.P. Grinin*, *V.V. Sobolev*, Astrophys., **13**, 348, 1977.
9. *V.P. Grinin*, *V.V. Sobolev*, Astrophys., **28**, 208, 1988.
10. *V.P. Grinin*, *V.V. Sobolev*, Astrophys., **31**, 729, 1989.
11. *V.P. Grinin*, *V.M. Loskutov*, *V.V. Sobolev*, Astron. Rep., **37**, 182, 1993.
12. *M.M. Katsova*, *A.Ya. Boiko*, *M.A. Livshits*, Astron. Astrophys., **321**, 549, 1997.
13. *N.D. Kostiuk*, *S.B. Pikelner*, Sov. Astron., **18**, 590, 1975.
14. *M.A. Livshits*, *O.G. Badalyan*, *A.G. Kosovichev*, *M.M. Katsova*, Solar Phys., **73**, 269, 1981.
15. *G.B. Rybicki D.G. Hummer*, Astron. Astrophys., **262**, 209, 1992.

Moving Inhomogeneous Envelopes of Stars

L.M. Oskinova[1], B. Kubátová[2,3], W.-R. Hamann[1]

E-mail: *lida@astro.physik.uni-potsdam.de*

Luminous hot massive stars drive strong stellar winds. New observations together with progress in model calculations reveal that these winds are highly inhomogeneous. Building on the foundations laid by V.V. Sobolev and his school, we are now developing new methods to analyze stellar spectra emerging from such winds. Among them are the new sophisticated 3D models of radiation transfer in inhomogeneous expanding media that elucidate the physics of stellar winds and improve empiric mass-loss rate diagnostics.

1 Empirical diagnostics of stellar winds using UV resonance lines

Strong ionizing radiation and stellar winds of massive stars with OB spectral types strongly influence the physical conditions in the interstellar medium and affect the formation of new generations of stars and planets.

Hot star winds are driven by their intense ultraviolet (UV) radiation [1]. Theory predicts that the winds remove the mass with a rate $\dot{M} \approx 10^{-7} - 10^{-5} M_{\odot}\,\mathrm{yr}^{-1}$ depending on the fundamental stellar parameters: $T_{\rm eff}$, $L_{\rm bol}$, and $\log g$ [2]. Hence, during the life time of a massive star (up to a few$\times 10^7$ yr), a significant fraction of its mass is removed by the wind. Thus, the mass-loss rate is a crucial factor of stellar evolution.

Empirical diagnostics of mass-loss rates largely rely on a spectroscopic analysis of resonance lines from abundant ions. When formed in a wind, these lines typically display P Cygni-type profiles. The resonance lines are produced by a photon scattering, hence the line strength and shape depend on the wind velocity and density. The latter obeys a continuity equation $\dot{M} = 4\pi v(r) r^2 \rho$. Therefore, by fitting a model line to the observed one, it is possible to estimate the wind velocity, density, and the mass-loss rate.

Line formation in a moving stellar envelope was studied by V.V. Sobolev [3]. It was shown that *if* the thermal motions in the atmosphere can be neglected compared to the macroscopic velocity, the radiative transfer problem can be significantly simplified [4]. This is now known as the *Sobolev approximation.*

Hot star winds are fast, with typical velocities of a few$\times 1000\,\mathrm{km\,s^{-1}}$, justifying the use of Sobolev approximation for modeling their resonance lines [5, 6].

[1] Institute for Physics and Astronomy, University of Potsdam, Germany
[2] Astronomický ústav AV ČR, Czech Republic
[3] Matematički institut SANU, Serbia

V. Grinin et al. (eds) Radiation mechanisms of astrophysical objects. Yerevan: Edit Print, 2017, pp. 229–234.

Such models were used to estimate mass-loss rate already from the first available UV spectra of O-type stars [7, 8].

However, with time it became clear that the high turbulence in stellar winds limits the applicability of the Sobolev approximation. The error in the modeling arises mainly from the treatment of the formal integral and, to a lesser extent, from the approximated source function [9]. This is accounted for in the "Sobolev with Exact Integration" method (SEI), which treats the source function in Sobolev approximation, while finding exact integration for the transfer equation [10]. As a result, the model provides significantly better fit to the observed lines [11], and allows for more precise mass-loss rate determinations [12].

From the observational side, the problem with mass-loss determinations is that the strong resonance lines of the CNO elements are saturated in spectra of Galactic O-type stars. Therefore, these lines are not sensitive to the precise values of mass-loss rates. On the other hand, the resonance doublet of P V $\lambda\lambda 1117, 1128$ Å is never saturated because of a low phosphorus abundance ($\sim$1000 times less than the carbon one). Moreover, P V is a dominant ionization stage in O stars, hence its ionization fraction is nearly unity. This makes P V doublet very useful for the mass-loss rate measurements [13].

The Far Ultraviolet Spectroscopic Explorer (*FUSE*) measured spectra of P V for many O-type stars. The observed lines were weak, and the mass-loss rates derived from their modeling with the SEI method were found to be much smaller than expected [13]. It was concluded that either the true mass-loss rates are very small, or the traditional diagnostics of resonance lines are not suitable because of the strong stellar wind clumping.

2 Stellar wind clumping

There are clear evidences of stellar wind inhomogeneity. E.g., stochastic variability in the He II $\lambda 4686$ Å emission line in the spectrum of an O supergiant was explained by a clump propagating in its stellar wind [14]. The line-profile variability of Hα observed in a large sample of O-type supergiants was attributed to the presence of shell fragments in structured winds [15]. Using spectral diagnostics, it was shown that the winds of B supergiants are clumped [16]. The spectral lines of OB stars are variable on various time scales likely because of the wind clumping and structuring [17]. In high-mass X-ray binaries, accretion from the clumped stellar wind onto a neutron star powers strongly variable X-ray emission [18].

Stellar wind clumping is included in the modern non-LTE stellar atmosphere models [20, 21], using the usual approximation of *microclumping*, i.e. an assumption that all clumps in stellar wind are optically thin. Hence, the radiative transfer is significantly simplified in such models.

Assume that the density inside the clumps is enhanced by a factor D compared to a smooth model with the same mass-loss rate $\dot{M}$, while the interclump medium is void (i.e. the clump volume filling factor is $f_{\rm V} = D^{-1}$). Then, in the stellar atmosphere models, the rate equations have to be solved only for the clumps with the density $D\rho$ (instead of ρ as in the smooth wind case). In this case the mass-loss rates derived from fitting the lines that depend on the square of the density (such as, e.g., the recombination Hα line) will be by a factor $\sqrt{D}$ lower compared to the smooth wind models. On the other hand, mass-loss rates derived from the resonance lines (where both absorption and re-emission scales linearly grow with density) are not affected by microclumping.

3 Macroclumping

Albeit microclumping approximation is very convenient, it is too stringent for realistic stellar winds. Since optical depth in the UV resonance lines is high and the line photon mean free path is short, the wind clumps are likely to be optically thick at these wavelengths [19, 16]. To understand how such optically thick clumping ("macrocluming") affects the resonance line formation, it is useful to consider the Sobolev approximation. According to this approximation, only the matter close to the constant radial velocity surface contributes to the line optical depths. In a clumped wind, this surface will be porous (Fig. 1). Moreover,

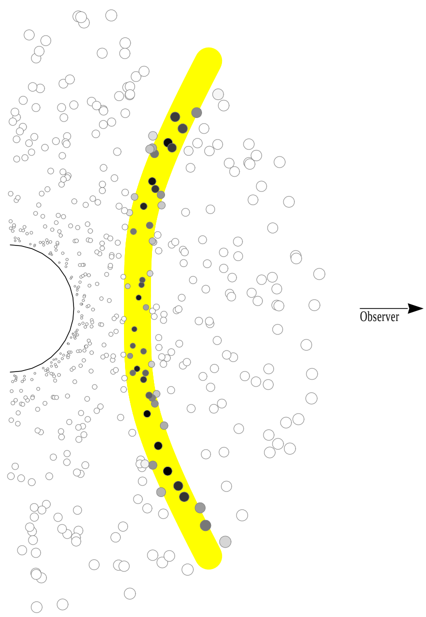

Figure 1: Sketch of a clumped stellar wind. In a smooth wind, rays of a given observer's frame frequency encounter line opacity only close to the "constant radial velocity surface" (thick shaded line). In a clumpy wind, assuming that the clumps move with the same velocity law as in the homogeneous wind, only those clumps interact with the ray that lie close to the corresponding constant radial velocity surface (dark-shaded circles). All other clumps are transparent (open circles) if the continuum opacity is small, so the wind is porous with respect to line absorption, even when the total volume is densely packed with clumps. Adopted from Oskinova et al. [19].

the opacity depends not only on geometrical matter distribution, but also on the Sobolev length $v_{\rm D}(dv/dr)^{-1}$, where $v_{\rm D}$ denotes the velocity dispersion within a clump. Correspondingly, the smaller the velocity dispersion within each clump, the narrower the constant radial velocity surface. Consequently, a smaller number of clumps can contribute to opacity, farther reducing it.

Adopting a statistical treatment of effective opacity $\kappa_{\rm eff}$, a correction factor for macroclumping that can be easily included in a sophisticated non-LTE codes was derived [19]. One can show that

$$\kappa_{\rm eff} = \kappa_{\rm f}\ \frac{1-e^{-\tau_{\rm C}}}{\tau_{\rm C}} \equiv \kappa_{\rm f}\ C_{\rm macro}. \tag{1}$$

The factor $C_{\rm macro}$ describes how macroclumping changes the opacity in the microclumping limit $\kappa_{\rm f}$. Note that for optically thin clumps ($\tau_C \ll 1$), the microclumping approximation ($\kappa_{\rm eff} \approx \kappa_{\rm f}$) is recovered. For optically thick clumps ($\tau_C \gtrsim 1$), however, the effective opacity is reduced by a factor $C_{\rm macro}$ compared to the microclumping approximation.

4 Radiative transfer using realistic 3D Monte-Carlo wind models

The statistical treatment of macroclumping provides only a first approximation for radiative transfer in clumped winds. For in-depth studies, the full 3D models of clumped winds are developed [22, 23]. In these models the density and velocity of the wind can be arbitrarily defined in a 3D space and can be non-monotonic. The photons are followed along their paths using the Monte Carlo approach. Allowing for an arbitrary optical depth, clumps can be optically thick in the cores of resonance lines, while they remain optically thin at all other frequencies. The model lines are calculated and compared to the observed ones.

Detailed study showed that strengths and shape of the resonance lines depend on the spatial distribution of clumping, density contrast, and velocity field [22]. Overall, these 3D models confirmed that macroclumping reduces effective opacity in the resonance lines, and rigorously proved that in realistic winds the P Cygni profiles of resonance lines are different from those in smooth and stationary 3D winds.

The models were compared with the observed spectra of five O-type stars to measure their mass-loss rates and other wind parameters [23]. This was done using a combination of the non-LTE Potsdam Wolf-Rayet (PoWR) stellar atmospheres (Fig. 2) and the Monte Carlo routine for the transfer of radiation in resonance lines. It was shown that the strength of model P V lines is reduced in realistic 3D models compared to the smooth wind models. Therefore, the observed lines could be fitted with high mass-loss rates similar to those theoretically expected (Fig. 3).

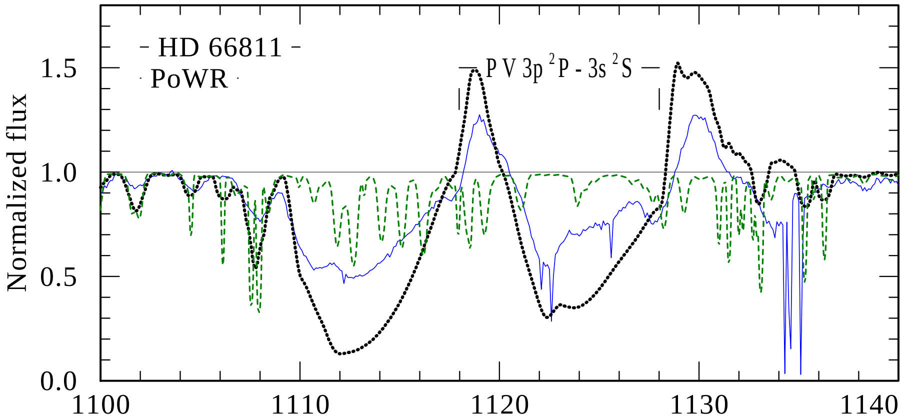

Figure 2: Comparison of observed and model spectra of P V in the O4I star HD 66811 (ζ Pup). Thin solid-blue lines is the observed spectrum. Dotted black line is the PoWR model spectrum adopting $\dot{M} = 2.5 \times 10^{-6}\, M_{\odot}\, \mathrm{yr}^{-1}$. The dashed-green lines are from the same model, but only accounting for the photospheric lines while wind contribution is suppressed.

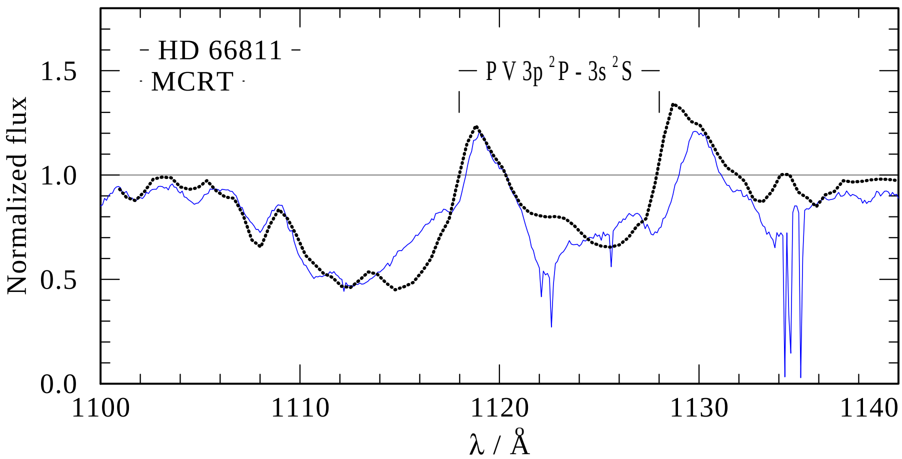

Figure 3: The same as in Fig. 2, but now the dotted black line is computed with the 3D Monte Carlo wind model, using the PoWR photospheric spectrum as input. The adopted mass-loss rate is $\dot{M} = 2.5 \times 10^{-6}\, M_{\odot}\, \mathrm{yr}^{-1}$. The line strength is significantly reduced compared to Fig. 2 despite the same adopted $\dot{M}$. See model details in Surlan et al. [23].

To summarize, the advances of macrocluming approach and 3D wind modeling improved empiric mass-loss rate diagnostics and showed that the mass-loss rates of OB supergiants are in good agreement with the theoretical predictions. Depending on the adopted clumping parameters, the observed spectra can be well reproduced with only a factor of 1–3 reduction compared to the predicted ones.

Thus, macroclumping is a new step in our quest for realistic descriptions of stellar wind, which would have been not possible without deep insights of V.V. Sobolev and his school into the physics of moving stellar envelopes.

References

1. *J.I. Castor, D.C. Abbott, R.I. Klein*, Astrophys. J., **195**, 157, 1975.
2. *A. Pauldrach, J. Puls, R.P. Kudritzki*, Astron. Astrophys., **164**, 86, 1986.
3. *V.V. Sobolev*, Moving Envelopes of Stars. Cambridge: Harvard Univ. Press, 1960 (Original in Russian: Dvizhushchiesya Obolochki Zvezd. Leningrad: Izd. Leningr. Univ., 1947).
4. *V.P. Grinin*, Astrophys., **44**, 402, 2001.
5. *J.I. Castor*, Mon. Not. Roy. Astron. Soc., **149**, 111, 1970.
6. *L.B. Lucy*, Astrophys. J., **163**, 95, 1971.
7. *J.I. Castor, H.J.G.L.M. Lamers*, Astrophys. J. Suppl., **39**, 481, 1979.
8. *P.S. Conti, C.D. Garmany*, Astrophys. J., **238**, 190, 1980.
9. *W.-R. Hamann*, Astron. Astrophys., **100**, 169, 1981.
10. *H.J.G.L.M. Lamers, M. Cerruti-Sola, M. Perinotto*, Astrophys. J., **314**, 726, 1987.
11. *M.A.T. Groenewegen, H.J.G.L.M. Lamers*, Astron. Astrophys. Suppl., **79**, 359, 1989.
12. *H.J.G.L.M. Lamers, S. Haser, A. de Koter, C. Leitherer*, Astrophys. J., **516**, 872, 1999.
13. *D. Massa, A.W. Fullerton, G. Sonneborn, J.B. Hutchings*, Astrophys. J., **586**, 996, 2003.
14. *T. Eversberg, S. Lépine, A.F.J. Moffat*, Astrophys. J., **494**, 799, 1998.
15. *N. Markova, J. Puls, S. Scuderi, H. Markov*, Astron. Astrophys., **440**, 1133, 2005.
16. *R.K. Prinja, D.L. Massa*, Astron. Astrophys., **521**, L55, 2010.
17. *S. Lépine, A.F.J. Moffat*, Astron. J., **136**, 548, 2008.
18. *L.M. Oskinova, A. Feldmeier, P. Kretschmar*, Mon. Not. Roy. Astron. Soc., **421**, 2820, 2012.
19. *L.M. Oskinova, W.-R. Hamann, A. Feldmeier*, Astron. Astrophys., **476**, 1331, 2007.
20. *W.-R. Hamann, L. Koesterke*, Astron. Astrophys., **335**, 1003, 1998.
21. *D.J. Hillier, D.L. Miller*, Astrophys. J., **519**, 354, 1999.
22. *B. Šurlan, W.-R. Hamann, J. Kubát, L.M. Oskinova, A. Feldmeier*, Astron. Astrophys., **541**, A37, 2012.
23. *B. Šurlan, W.-R. Hamann, A. Aret, J. Kubát, L.M. Oskinova, A.F. Torres*, Astron. Astrophys., **559**, A130, 2013.

* The color figures are available online in the Proceedings at *http://www.astro.spbu.ru/sobolev100/*.

Outflows and Accretion on the Late Phases of PMS Evolution. The Case of RZ Psc

I.S. Potravnov[1], V.P. Grinin[1,2], D.E. Mkrtichian[3], D.N. Shakhovskoy[4]

E-mail: *ilya.astro@gmail.com*

We consider the spectral variability of the post T Tauri star RZ Psc. The star does not show clear accretion traces, but at the same time it has distinct variable blue-shifted features in the Na I D resonance doublet and lines of other alkali metals which indicate the matter outflow from the stellar vicinity. We suppose that in case of RZ Psc we deal with the special type of interaction between the remnants of accreting gas and stellar magnetosphere in the "magnetic propeller" regime. It is expected that accretion in the propeller regime exists in some others young stars.

1 Introduction

Over three recent decades the magnetospheric accretion paradigm was developed and improved to explain the observed activity among young solar type stars. These so-called T Tauri stars actively accrete the matter from their protoplanetary disks and possess the notable spectroscopic evidences for complex gas motion in the near vicinity of the star. The profiles of the strong hydrogen emission lines and lines of some metals reveal the accretion infall as well as the less significant matter outflow due to the magnetospheric conical and X-wind. The overview of the basic concepts of the theory and its application to the observations can be found in the review by Bouvier et al. [1].

According to the recent investigations of several open clusters and young stellar associations, the phase of the actively accreting T Tauri star lasts only few million years (Myr) (see, e.g., the review by Williams and Chieza [2]). During this period the circumstellar disk evolves from an optically thick gaseous and dusty protoplanetary disk into an optically thin debris disk consisting of large particles, planetesimals, and planets. From the observational point of view, this evolution is reflected by a difference between the "Classical" (CTTS), "Weak line" (WTTS), and "Post" T Tauri stars. The last two subclasses in this sequence possess the mild characteristics of activity which decay with their age. Fedele et al. [3] show that on the timescale of 10 Myr accretion becomes vanishingly small (less than

[1] Pulkovo Astronomical observatory, Russia
[2] Sobolev Astronomical Institute of the St. Petersburg University, Russia
[3] National Astronomical Research Institute of Thailand
[4] Crimean Astrophysical Observatory, Crimea

V. Grinin et al. (eds) Radiation mechanisms of astrophysical objects. Yerevan: Edit Print, 2017, pp. 235–240.

$10^{-11} M_\odot$ yr^{-1}). Hence, the spectroscopic traces of the accretion/outflow process should also disappear on such a timescale.

The careful investigation of the stars near or even above this limit has the crucial importance for our understanding of the late stages of Pre-Main Sequence evolution. In the systems with the low accretion rate some special cases of interaction between stellar magnetosphere and remnants of the accreting gas can arise and can be studied in its “pure form”. Such observational traces are not masked by the more prominent accretion features typical of early stages of the PMS evolution.

One of such unique objects is the star RZ Psc.

2 RZ Psc and its spectroscopic behavior

RZ Psc belongs to the family of young variable UX Ori type stars. The photometric and polarimetric activity of these stars is caused by the variable circumstellar (CS) extinction [4]. RZ Psc is one of the coolest (Sp = K0 IV) and eldest member of the family. According to the latest estimates, based on calculating the trajectory of the star in the gravitational potential of Galaxy, its age is about 25±5 million years [5, 6]. This value is considerably higher than the characteristic lifetime of the accretion disks and means that the star is surrounded by the significantly evolved accretion disk.

The spectrum of the RZ Psc strongly resembles the spectrum of a star that already passed the stage of the T Tauri stars, without any prominent emission features above the continuum level. There is the only important exception: the lines of the resonance sodium doublet Na I D show the blue-shifted absorption components which manifest the gas motion from the star toward the observer [7]. These absorption details were initially discovered in the spectra obtained in

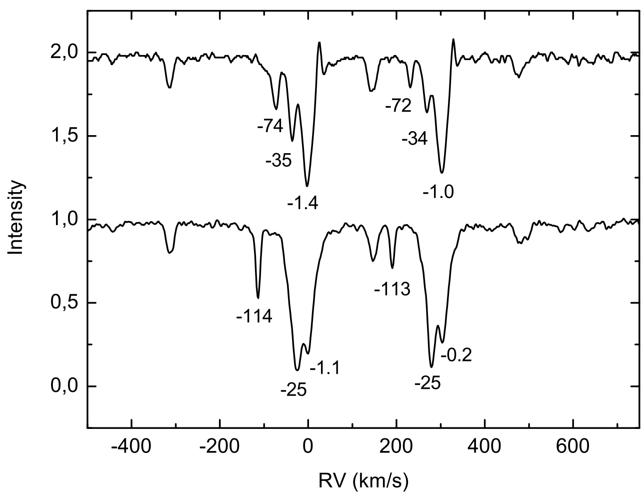

Figure 1: The Na I D lines in the spectra of RZ Psc observed with NOT.

the Peak Terskol Observatory during the seasons 2009–2012 with the moderate spectral resolution $R \sim 13500$ [7]. It should be stressed that despite blue-shifted absorptions are highly variable, no red-shifted details or signs of emission in Na D lines has been observed.

These details are very notable on the pair of the high-resolution FIES spectra ($R \sim 46000$), obtained in August and November 2013 by I. Ilyin with 2.56 m Nordic Optical Telescope (see [9] and Fig. 1).

The subsequent observations were carried out by one of the authors of our paper (D.E.M.) at the 2.4 m telescope of the Thai National Observatory with MRES echelle spectrograph in December 2014. The covered region was from 4400 to 8800 Å that allowed us to include lines of other alkali metals K I and Ca II into consideration. These lines are presented in Fig. 2.

One can see an appearance of the variable blue-shifted absorption components in Na I D lines which are accompanied by the similar structures in the K I 7699 Å line. The features in the K I line are less prominent due to the lower potassium abundance, but reach their maximum when the sodium lines also show the strongest additional absorption. The Ca II 8542 Å line belongs to the calcium IR triplet and demonstrates more complicated picture. The line core is filled in by the variable emission, while the additional low-velocity absorption appears on several dates. Nevertheless, RZ Psc still does not possess any clear accretion signs in its spectra.

The possible key to this mystery came from observations of the Hα line. It also has the pure absorption profile in RZ Psc spectrum. But a careful comparison of it with the synthetic profile and profile observed in the spectrum of the standard star σ Dra (K0 V) reveals the presence of the weak variable emission component in the central part of the Hα line. The spectral subtraction technique shows the narrow emission peak, that can be probably attributed to the chromospheric activity, and the broad (up to $\pm$ 200 km s^{-1}) emission base forms in the accreting matter (Fig. 3).

3 Discussion and conclusions

Measurement of the equivalent width (EW) of the Hα emission in RZ Psc spectra gives the mean value of about 0.5 Å. This value is significantly less than the standard value of 10 Å which separates the actively accreting CTTS from WTTS. According to this criteria, we can call RZ Psc as "the very Weak line T Tauri star". Measurement of Hα emission EW allows us to estimate the accretion rate in the system, using the empirical relationship between the observed emission line luminosity and total accretion luminosity from [8]. The obtained value $\dot{M} \sim 7 \times 10^{-12} M_{\odot}\,\mathrm{yr}^{-1}$ is an upper limit of the real accretion rate, because the Hα line in the RZ Psc spectrum possibly arises not only in the accreting matter but also in the stellar chromosphere. Nevertheless, this accretion rate is the lowest one known from the literature.

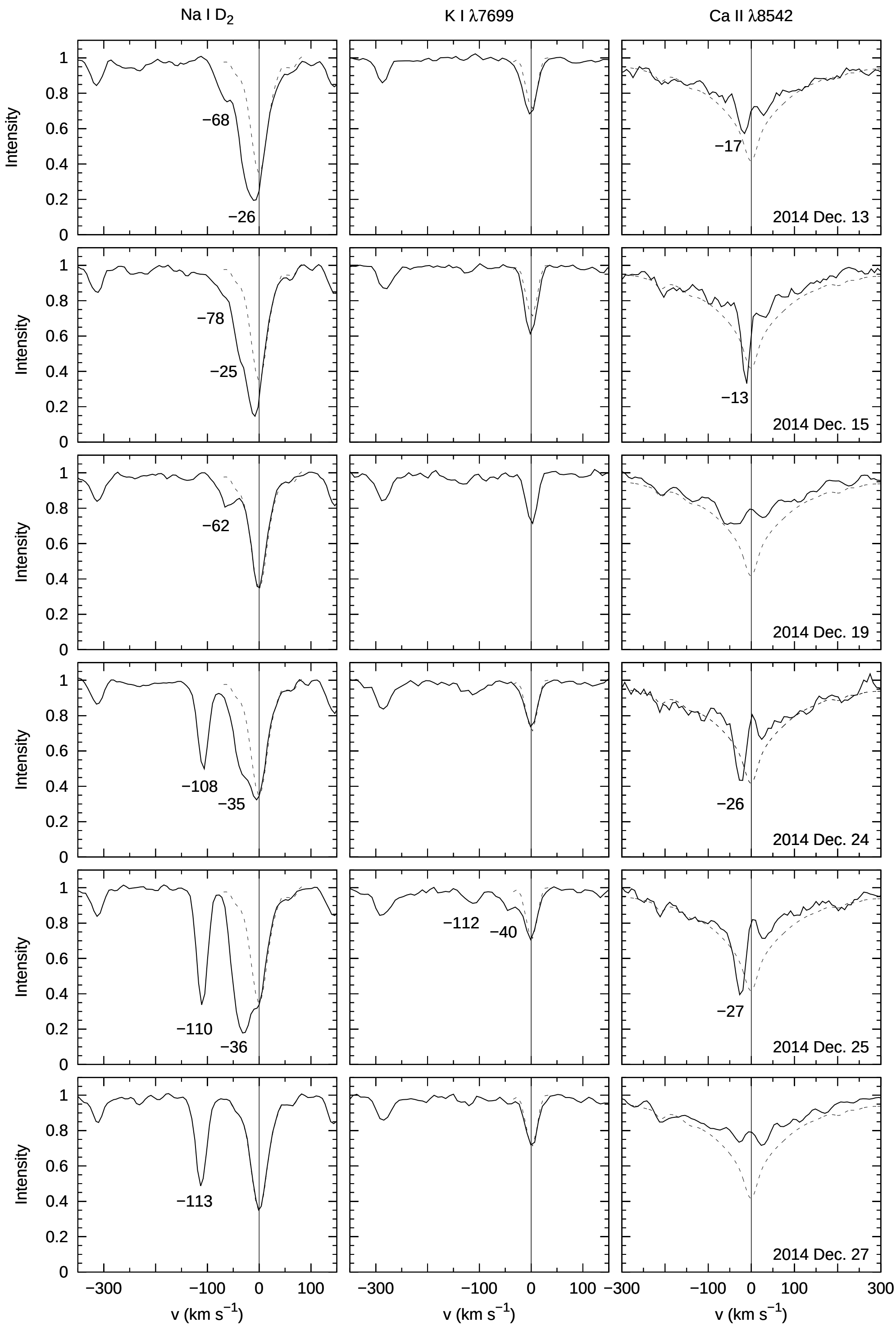

Figure 2: Alkali metal lines observed in the RZ Psc spectra with the MRES. The velocities in km s^{-1} of the variable absorption components are labeled. The reference photospheric profiles are plotted by dashed line.

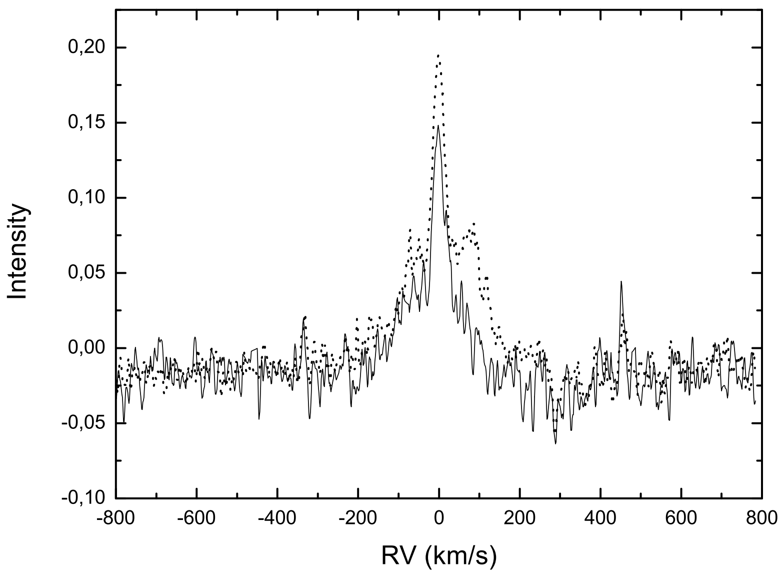

Figure 3: The emission components of the Hα line obtained after subtraction of the synthetic profile from the observed ones. Solid line corresponds to the observations obtained on Aug. 19, 2013, while the dotted line shows spectrum obtained on Nov. 21, 2013.

Hence, in the case of RZ Psc, we deal with the extremely low accretion rate and, at the same time, with nontrivial spectroscopic signs of the matter outflow. We supposed that the gaseous outflow from the RZ Psc vicinity was a result of the action of the so-called "propeller mechanism" arising at the interaction between the stellar magnetosphere and remnants of the gas in the circumstellar disk [9]. This mechanism is realized when the angular velocity of the star (and the magnetosphere) exceeds the angular velocity of the Keplerian disk at the truncation radius in the region where the magnetic field still controls the motion of the gas. The ratio between the corotation and truncation radii depends inversely on the mass accretion rate. When it is small, the truncation radius can significantly exceed the corotation radius. Under this conditions, most of the accreting matter is scattered into the surrounding space.

There are observational evidences (so-called AA Tau effect) that the situation, when the axis of magnetic dipole does not coincide with the rotational axis of the star, is not rare among young T Tauri stars (see, e.g., [10, 11]). Numerical simulations by Romanova et al. [12] showed that interaction between the accreting gas and inclined magnetic dipole produced the special case of a biconical outflow consisted of two expanding spiral structure. The multiple intersection of the line of sight by the spiral can produce the corresponding absorption lines shifted relatively to the star velocity.

Similar narrow absorption details are observed in the NaI D lines in the spectra of some other young stars such as MWC 480, NY Ori and BBW 76. However, these objects are at earlier evolutionary stages and show spectroscopic signs of accretion. However, the magnetic propeller regime is not necessary phase of the evolution of T Tauri stars. The unstable behavior of the gaseous outflow significantly complicates the theoretical modeling. Sobolev's theory for the medium with large velocity gradients was developed and applied to the media where the gas density was determined from the continuity equation. In the case of RZ Psc, the situation is quite different: narrow absorption components in the lines of the sodium doublet in combination with the lack of the emission in these lines indicate that the absorbing gas fills in only the minor part of the whole solid angle 4π (see [9]). It is important to learn how to calculate the profiles and intensities of the spectral lines formed in such conditions.

A more detailed description and discussion of the spectral variability of RZ Psc will be forthcoming.

Acknowledgments. This research has been supported in part by the Russian Foundation for Basic Research (Projects 15-02-09191 and 15-02-05399).

References

1. *J. Bouvier, S.H.P. Alencar, T.J. Harries et al.*, in Protostars and Planets V. Eds. Bo Reipurth et al. Tucson: Univ. Arizona Press, 2007, p. 479.
2. *J.P. Williams, L.A. Cieza*, Ann. Rev. Astron. Astrophys., **49**, 67, 2011.
3. *D. Fedele, M.E. van den Ancker, Th. Henning et al.*, Astron. Astrophys., **510**, A72, 2010.
4. *V.P. Grinin, N.N. Kiselev, G.P. Chernova et al.*, Astrophys. Space Sci., **186**, 283, 1991.
5. *V.P. Grinin, I.S. Potravnov, F.A. Musaev*, Astron. Astrophys., **524**, A8, 2010.
6. *I.S. Potravnov, V.P. Grinin*, Astron. Lett., **39**, 776, 2013.
7. *I.S. Potravnov, V.P. Grinin, I.V. Ilyin*, Astrophys., **56**, 453, 2013.
8. *E. Rigliaco, A. Natta, L. Testi et al.*, Astron. Astrophys., **548**, A56, 2012.
9. *V.P. Grinin, I.S. Potravnov, I.V. Ilyin et al.*, Astron. Lett., **41**, 407, 2015.
10. *J. Bouvier, S.H.P. Alencar, T. Boutelier et al.*, Astron. Astrophys., **463**, 1017, 2007.
11. *O.Yu. Barsunova, V.P. Grinin, S.G. Sergeev*, Astrophys., **56**, 395, 2013.
12. *M.M. Romanova, G.V. Ustyugova, A.V. Koldoba et al.*, Mon. Not. Roy. Astron. Soc., **399**, 1802, 2009.

Activity and Cool Spots on the Surfaces of Stars with Planetary Systems and G-type Stars with Superflares from Kepler Observations

I.S. Savanov[1]

E-mail: *isavanov@inasan.ru*

Based on the photometric observations obtained with the Kepler telescope, we investigated the properties of the active regions (cold spots) on the surfaces of stars with planetary systems (exoplanets) and G type superflare stars. Three methods for determining the spottedness (S) of stellar surfaces were used. We studied the dependencies of the spottedness of the stars with exoplanets on the effective temperature and on the period of their axial rotation. In most cases the spottedness of stars with planetary systems does not exceed 5% of the area of their surface. The properties of active regions (cool spots) on the surfaces of 279 G-type stars in which more than 1500 superflares with energies of 10^{33}–10^{36} erg were analyzed. Three groups of stars with different surface spottednesses can be distinguished in a plot of superflare energy vs. cool-spot area. It is confirmed that the flare activity is not related directly to circumpolar active regions, since the majority of the points on the diagram lie to the right of the dependence for $B = 1000$ G and $i = 3°$.

1 Observational data and methods of analysis

Using the high-accuracy photometric observations obtained with the Kepler telescope, we studied the properties of the active areas (cool spots) on the surfaces of stars with planetary systems. The analysis was carried out using the data on 737 objects for which the rotation periods were estimated in [1] and reliable estimates of atmospheric parameters were available. Three methods of stellar surface spottedness estimation from the photometric observations were reviewed (the values $S1$, $S2$, and $S3$). On the example of two stars (KOI 877 and KOI 896) from the full sample of 737 stars, we compared the results of the $S1$–$S3$ estimation with the three mentioned methods. It was found that the results of the accurate calculations ($S1$) and estimations ($S2$) by the method of [2] correspond to each other, although the values of the latter are systematically higher.

It was shown that the method proposed in [3] and modified by us in [2] can be applied to a large enough sample of objects and, most importantly, it

[1] Institute of Astronomy, Russian Academy of Sciences, Russia

V. Grinin et al. (eds) Radiation mechanisms of astrophysical objects. Yerevan: Edit Print, 2017, pp. 241–244.

yields homogeneous data which can be used for statistical estimation and finding dependencies of general nature. This allowed us from the brightness variability data for 34 030 objects from [4] to find the S parameters for the analysis of the distribution of the S on the effective temperature for different objects.

For the late type stars with planetary systems, we used the data from Table 1 in [1] for 12 Quarters of observations (Q3–Q14). In the final sample we included the data on 737 objects for which in [1] the rotation periods were estimated and reliable estimates of the atmospheric parameters were available (the effective temperature and gravities) and which are not eclipsing binaries (i.e., their photometric variability is associated mainly with the cold spots). According to [1], the estimated rotation periods for the 737 stars under study are in the range of 0.9 to 62 days and the values of the photometric variability R_{var} are in the range of 0.18 to 64 mmag.

Based on our approach we used the specified technique for the analysis of activity of 279 stars in which Shibayama et al. [5] have reported 1547 superflares. For this purpose, we used the data of Table 2 from [5], which contained information both about the photometric variability of these stars and their flare activity.

2 The dependence of the spottedness on the effective temperature and rotation period

We examined the variation of the spottedness ($S2$) for the stars with planetary systems as a function of the effective temperature of these objects and the period of their axial rotation. The $S2$ value for these stars in most cases does not exceed 5% of the area of their surface. The three objects for which it exceeds 5 percent were examined in detail. We have not found any indications that the magnetic activity of a star with exoplanets has any special features that distinguish it from the activity of the stars from a wider sample from [4]. It was found that for the stars with effective temperatures smaller than 5750 K, the spottedness values decrease monotonously with the stellar rotation period decrease. The absence of stars with small S values (smaller than 0.002) was established for the stars with effective temperatures lower than 5750 K and rotation periods up to 10 days. The stars with effective temperatures higher than 5750 K have a very small spottedness for fast-rotating stars, which increases for the objects with the rotation periods of about 20–25 days.

In the case of G-type superflare stars we carried out additional analyses of diagrams plotting the energy of superflares against parameters of the stellar activity (the area of their magnetic spots) and also conducted more extensive studies of the activity of two stars with the highest numbers of superflares [5]. For this aim, we analyzed the properties of the active regions (cool spots) on the surfaces of 279 G stars displaying more than 1500 superflares with energies of 10^{33}–10^{36} erg.

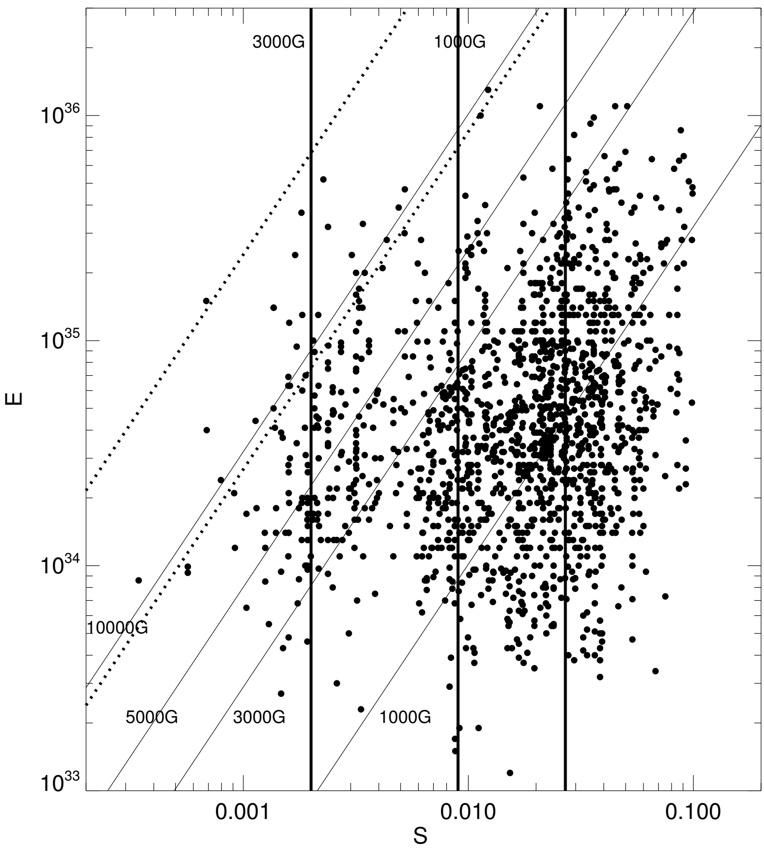

Figure 1: Comparison of the superflare energy E with the spotted area S.

We supplemented the conclusion of [5] that the maximum energy of superflares is independent of the stellar rotational periods P with the suggestion that the entire range of variations of the flare energies is independent of P. Analysis of the diagrams displaying comparisons of the superflare energy and the area occupied by cool spots (Fig. 1) suggests the possible existence of three groups of objects: stars whose spotted areas S exceed 1–1.1 % of the visible area of the star (the most numerous group), stars for which S more than 0.9 %, and stars for which S is less than 0.1 %. The majority of points on this diagram lie to the right of the dependence corresponding to B = 3000 G and $i = 90°$ (the first two groups of objects). Based on our new, more precise determinations of the parameter S we have confirmed the conclusion of [6] that the flare activity is not directly related to circumpolar active regions, since the vast majority of points in Fig. 1 lie to the right of the dependence for B = 1000 G and $i = 3°$ (the stars are essentially viewed pole-on). Our analysis of stars from a sample including objects with more than 20 superflares indicated that substantial variations in the flare energy can be achieved in the presence of only small variations in S for a single star (the range of flare energy can reach two orders of magnitude with essentially the same area occupied by magnetic spots). Only two objects in the sample displayed substantial variations in their spottedness (by factors of five to six; KIC 10422252 and KIC 11764567). Variations in the flare energy by orders of magnitude were observed for any level of spottedness.

3 Results

Using the high-accuracy photometric observations obtained with the Kepler telescope, we studied the properties of the active areas (cool spots) on the surfaces of stars with planetary systems. The analysis was carried out using the data on 737 objects. We have not found any indications that the magnetic activity of a star with exoplanets has any special features that distinguish it from the activity of the stars from a wider sample.

We also analyzed the properties of active regions (cool spots) on the surfaces of 279 G-type stars in which more than 1500 superflares with energies of 10^{33}–10^{36} erg were detected. Diagrams of superflare energy against activity parameters of the stars (the area of their magnetic spots) were considered. The range of variation of the superflare energies (up to two orders of magnitude) is realized over the entire interval of rotation periods. It is proposed that the plot of superflare energy vs. rotational period is bimodal. Three groups of stars with different surface spottednesses can be distinguished in a plot of superflare energy vs. cool-spot area. The range of variation of the flare energy within a group is roughly the same for these three groups. Most of the points on this diagram lie to the right of the dependence corresponding to $B = 3000$ G and an inclination $i = 90°$ (the first two groups of objects). It is confirmed that the flare activity is not related directly to circumpolar active regions, since the majority of the points on the diagram lie to the right of the dependence for $B = 1000$G and $i = 3°$.

Additional detailed information can be found in our publications [7, 8, 9, 10].

References

1. *A. McQuillan, T. Mazeh, S. Aigrain*, Astrophys. J. Lett., **775**, L11, 2013.

2. *I.S. Savanov*, Astron. Rep., **58**, 478, 2014.

3. *S.S. Vogt*, Astrophys. J., **250**, 327, 1981.

4. *A. McQuillan, T. Mazeh, S. Aigrain*, Astrophys. J. Suppl., **211**, 24, 2014.

5. *T. Shibayama, H. Maehara, S. Notsu et al.*, Astrophys. J. Suppl., **209**, 5, 2013.

6. *Y. Notsu, T. Shibayama, H. Maehara et al.*, Astrophys. J., **771**, 127, 2013.

7. *I.S. Savanov*, Astrophys. Bull., **70**, 83, 2015.

8. *I.S. Savanov*, Astrophys. Bull., **70**, 292, 2015.

9. *I.S. Savanov, E.S. Dmitrienko*, Astron. Rep., **59**, 879, 2014.

10. *I.S. Savanov, E.S. Dmitrienko*, Astrophys. Bull., **71**, 59, 2016.

Non-LTE Models of the Emitting Regions in Young Hot Stars

L.V. Tambovtseva[1], V.P. Grinin[1,2]

E-mail: *lvtamb@mail.ru*

Various disk and outflow components of the circumstellar environment of young Herbig Ae/Be stars may contribute to the hydrogen line emission. These are a magnetosphere, disk wind (photoevaporative, magneto-centrifugal, conical or X-wind), gaseous accretion disk (both hot surface layers (inward of 10 AU) and innermost hot midplane of the accretion disk heated by the viscous dissipation (inward of 0.1 AU). Non-LTE modeling was performed to show the influence of the model parameters on the intensity and shape of the line profiles for each emitting region, to present the spatial distribution of the brightness for each component and to compare the contribution of each component to the total line emission. The modeling shows that the disk wind is the dominant contributor to the hydrogen lines compared to the magnetospheric accretion and gaseous accretion disk.

1 Introduction

The star formation theory developed for T Tauri stars (TTSs) successfully explains magnetospheric accretion [1, 2, 3], and magneto-centrifugal disk wind and jet formation [4, 5, 6]. To improve our knowledge of the physical processes in Herbig Ae/Be stars, it is useful to investigate them with theoretical models developed for TTSs, taking into account the special features of HAEBEs (the large luminosity, rapid rotation, weak magnetic fields).

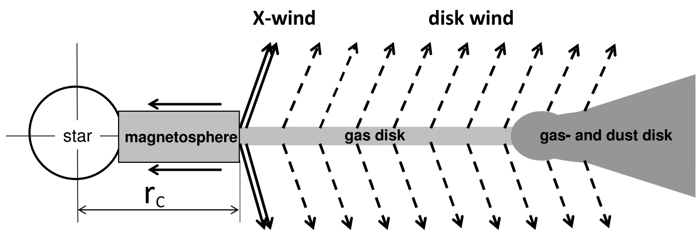

Figure 1: A sketch of line emitting regions in Herbig Ae star.

The promising method to probe the inner environment of young stars is to simultaneously reproduce both the hydrogen emission spectra and the observables of infrared long-baseline interferometry, that is, visibilities, wavelength-differential phases, and closure phases, e.g. [7, 8, 9, 10]. Let us consider

---

[1] Pulkovo Astronomical observatory, St. Petersburg, Russia
[2] Sobolev Astronomical Institute of St. Petersburg University, Russia

V. Grinin et al. (eds) Radiation mechanisms of astrophysical objects. Yerevan: Edit Print, 2017, pp. 245–252.

schematic picture of the environment of the young intermediate-mass Herbig Ae/Be stars (HAEBEs) (Fig. 1). It presents several gaseous regions emitting the hydrogen lines: (1) magnetospheric accretion region, (2) disk wind which can be presented in the different form (magneto-centrifugal wind, X-wind, conical wind and photoevaporative wind), (3) gaseous accretion disk, and (4) probably polar stellar wind. In this paper, we summarize results of our simultaneous non-LTE modeling of the Brγ emission lines in the spectra of several Herbig Ae/Be stars and interferometric variables obtained for these stars.

1.1 Computational scheme

For all emitting components we performed the non-LTE modeling solving the radiative transfer problem. Differences are in geometry of the regions, and, consequently, in the form of the mass continuity equation and velocity gradient. Solution of the radiative transfer problem has been made as follows. We calculated the excitation and ionization state with the help of numerical codes developed by [11, 12, 13] for the media with the large velocity gradient. The radiative terms in the equations of the statistical equilibrium which take into account transitions between the discrete levels are calculated in the Sobolev approximation [14]. The intensity of the disk wind radiation emergent at the frequencies within the spectral line has been calculated by exact integration over spatial co-ordinates in the approximation of the full redistribution over the frequencies in the co-moving coordinate system. We considered 15 atomic levels and continuum. The

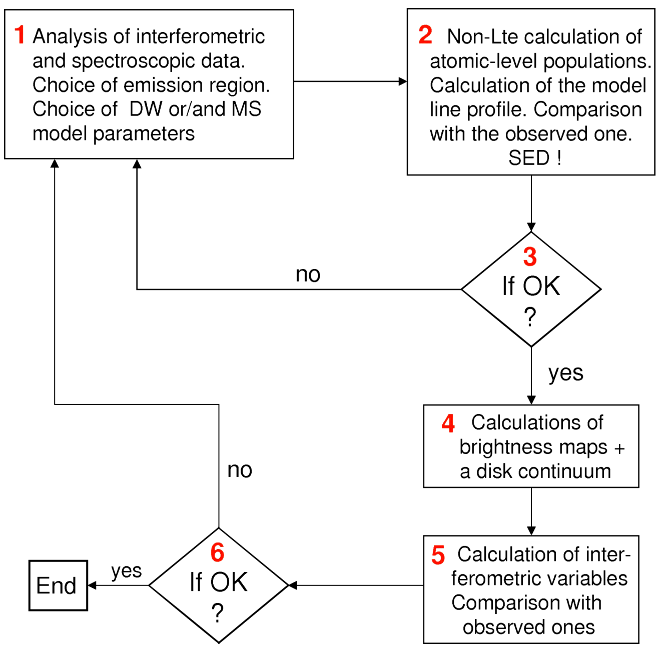

Figure 2: A principle algorithm of simultaneous calculations of emission in the line and interferometric variables.

algorithm of simultaneous calculations of the line emission and interferometric functions is shown in Fig. 2:

1) We choose the appropriate model parameters and compute the velocity and density distribution throughout the region.
2) We divide the integration region by the grid with cells over co-ordinates $[l, \theta, \varphi]$, assuming a wind/accretion temperature distribution. We solve the equation system of statistical equilibrium for the hydrogen atoms in each cell and find the populations of the atomic levels and ionization state in the media.
3) We compare the line profile with the observed one. In the case of a good agreement, we calculate brightness maps at the given frequencies.
4) We calculate the interferometric functions (visibilities, differential and closure phases) and compare them with the observed ones. In the case of the bad agreement we change the model of emitting region. Modeling process is described in details in [15, 16].

2 Models of emitting regions

2.1 Disk wind

Blandford and Payne [17] showed that if an open magnetic field passed through an infinitely thin, Keplerian disk, and is "frozen" into it, and if the field lines make with the disk surface an angle equal to or less than 60°, then gas from the disk surface will be flung out centrifugally along the field lines and can be accelerated to super-Alfvenic velocities. Father from the disk the toroidal component of the field collimates the outflow into two jets which are perpendicular to the disk plane.

There is a method of parametrization where the velocity and temperature distributions can be expressed in a parametric form (see, e.g. [3]). We applied it for HAEBEs. We divide the region of the disk wind by several streamlines, which are going out from point S (Fig. 3). We solve the mass continuity equation for each streamline using a sphere with the center in S. For simplicity, the disk wind consists of hydrogen atoms with a constant temperature (∼10 000 K) along

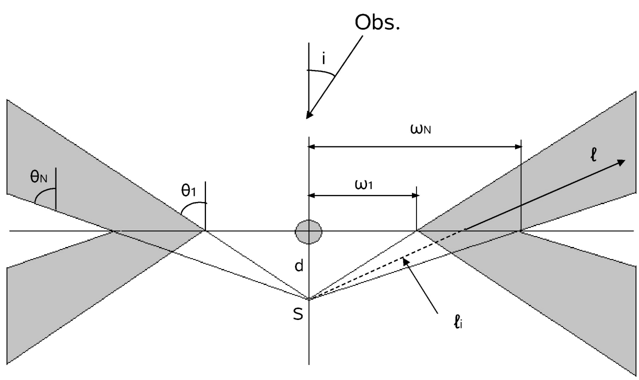

Figure 3: A sketch of the disk-wind region (not to scale).

Table 1: Disk wind model parameters

Model	θ_1	$\omega_1 - \omega_N$	γ	β	$\dot{M}_w$ in $M_\odot$ yr^{-1}
1	30°	$2R_* - 30R_*$	3	4	3×10^{-8}
2	30°	$2R_* - 20R_*$	3	5	3×10^{-8}
3	30°	$2R_* - 20R_*$	3	5	1×10^{-8}

the wind streamlines. As showed by Safier [18], the wind is rapidly heated by ambipolar diffusion to a temperature of ∼10 000 K. The wind electron temperature in the acceleration zone near the disk surface is not high enough to excite the Br line emission. Therefore, in our model, the low-temperature region below a certain height value does not contribute to the line emission. A full description of the disk wind model can be found in [15, 7].

Model parameters are as follows: ω_1 and ω_N are foot points of the disk wind launch region for the first and last trajectories of motion, or streamlines, respectively, θ_1 is the half opening angle between the 1st streamline and the vertical axis. The tangential velocity component $u(\omega)$ and poloidal velocity component $v(l)$ change along the streamlines, as given by

$$u(\omega) = u_K(\omega_i)\,(\omega/\omega_i)^{-1}, \tag{1}$$

$$v(l) = v_0 + (v_\infty - v_0)\,(1 - l_i/l)^{\beta}. \tag{2}$$

Here, $u_K(\omega_i) = (G\,M_*/\omega_i)^{1/2}$ at the starting point ω_i, v_0 and v_∞ are the initial and terminal velocities, respectively, G is the gravitation constant, M_* is the stellar mass, and β is a parameter. We assume v_0 to be the sound velocity in the disk wind, $v_\infty = f u_K(\omega_i)$, where $u_K(\omega_i)$ is the Keplerian velocity at distance ω_i from the star, and f is a scale factor. The two last parameters are the mass loss rate $\dot{M}_w$ and γ. The latter regulates the mass loading among the streamlines.

Examples of Hα and $H\beta$ line profiles (model 1 from Table 1) are presented in Fig. 4, where the profiles are shown for inclination angels from nearly pole-on

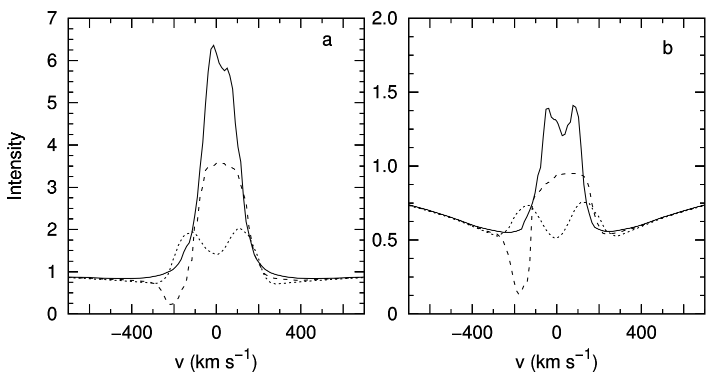

Figure 4: Hα (a) and Hβ (b) line profiles in the disk-wind model 1. Inclination angles are 30° (solid line), 47° (dashed line), and 85° (tiny dashed line); 0° corresponds to the face-on inclination.

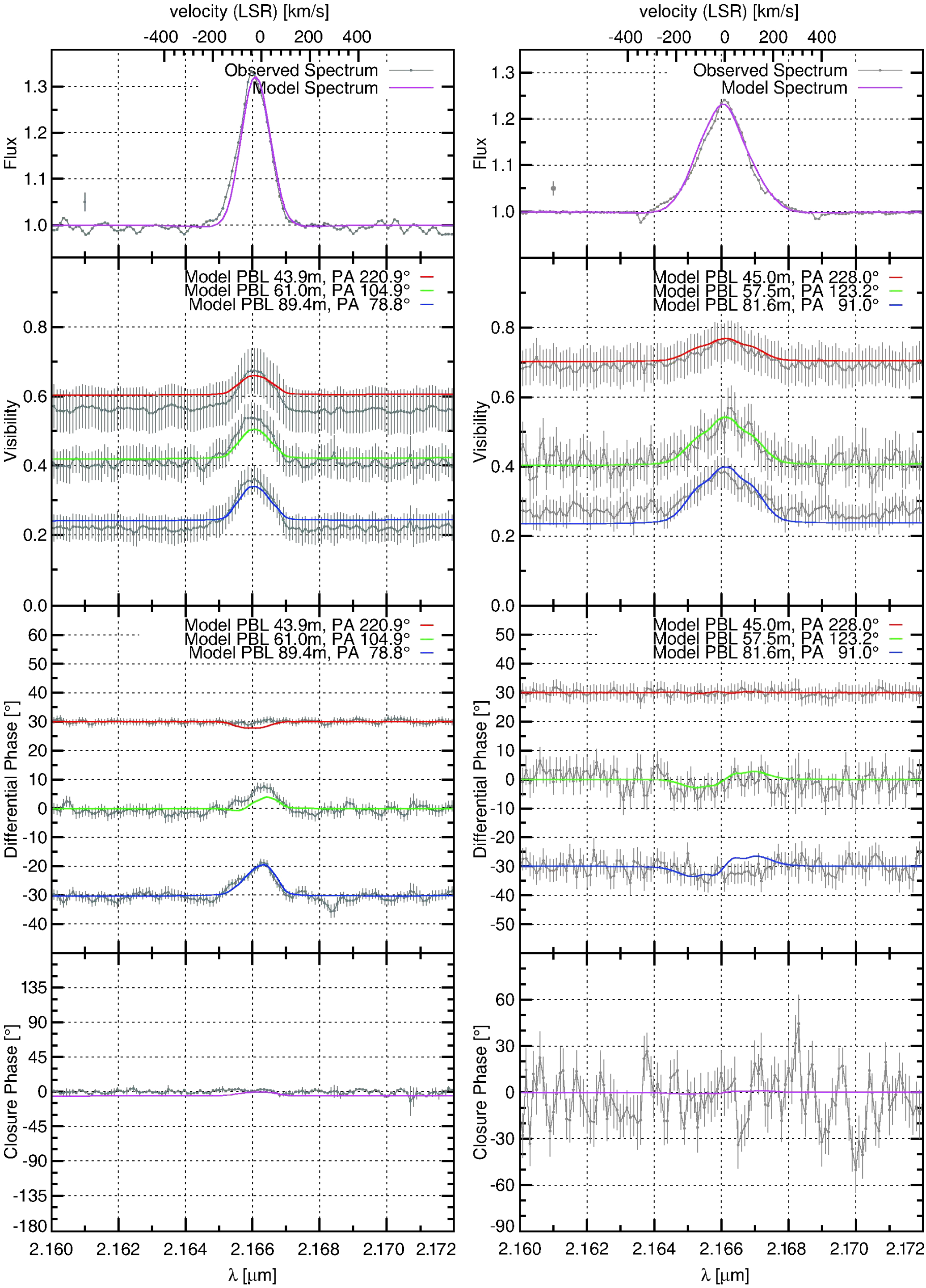

Figure 5: Brγ line profiles and interferometric variables observed and calculated in the framework of the disk wind models for the Herbig Be star HD 98922 (left) and the Herbig Ae star MWC 275 (right).

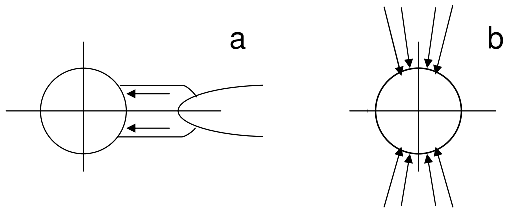

Figure 6: Sketch of the disk (a) and magnetospheric (b) accretion in HAEBEs.

to edge-on view. One can see modification of the line profile from a single one to P Cygni and double-peaked profiles. Modeling with simultaneous calculations of the Brγ line profiles and infrared interferometric variables was performed for several Herbig Ae/Be stars (MWC 297, MWC 275, and HD 98922 – [7, 8, 9]). Details and model parameters can be found in the papers cited. Examples of the observed and calculated line profiles and interferometric functions are presented in Fig. 5.

2.2 Magnetosphere and accretion disk

In our papers [13, 19, 16], we adapted the classical magnetospheric accretion model for TTSs to intermediate-mass Herbig Ae/Be stars. Taking into account that HAEBEs are luminous and rapidly rotating stars, we used a very compact disk-like magnetosphere with rotating gas in free-fall motion (Fig. 6a). This configuration can be used if the stellar magnetic field is weak enough to allow the accreting gas to approach the star surface at the low latitudes. Another configuration of the accreting zone (Fig. 6b) is expected if the magnetic field of the star is strong enough to transport the gas onto the pole regions [20]. In this case we can model the magnetospheric accretion zone by bi-polar thin cones because these regions contribute much more to the hydrogen line emission than outer parts of magnetosphere (not shown in Fig. 6b) due to the smaller gas temperatures in the outer regions. Our calculations of the infrared Brγ line emission (that probes the innermost stellar environment) together with interferometric functions showed that the contribution of the magnetospheric region to the hydrogen emission is no more than 40%. Our conclusion for hydrogen lines (including Balmer lines) is as follows: the emission from the magnetospheric accretion region is able to change the shape of the line profile, for example, to increase the wings of the profile and/or make it asymmetric. In calculations we used the ratio $\dot{M}_w/\dot{M}_{acc}$ = 0.1–0.3 $M_\odot$ yr^{-1}. Many examples of the Hα and Brγ lime profiles can be found in [19, 16].

We also considered the inner gaseous accretion disk as a possible source of the hydrogen emission. For formation of the hydrogen line, the temperature and density of the gas have to be high enough. We considered two components of the inner accretion disk: hot layers of the inner gaseous accretion disk (inward of 10 AU) and the innermost hot midplane of the accretion disk heated by viscous dissipation (inward of 0.1 AU) based on the study by Muzerolle et al. [21]

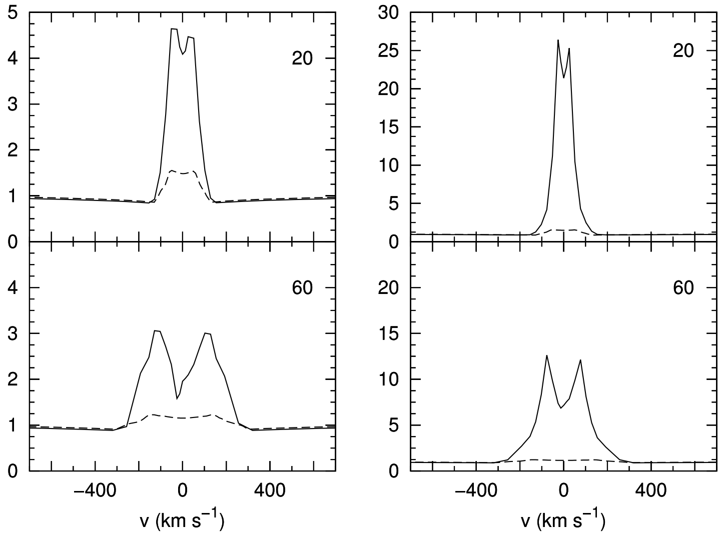

Figure 7: Brγ line profiles in the disk wind models (solid line) and the inner gaseous disk (dashed line) for inclination angles 20° and 60°. *Left*: the disk wind model 2; *right*: the disk wind model 3. Intensities are given in the units of the stellar continuum.

(see details in [16]). All of them contribute *less* Brγ and Hα emission than the *magneto-centrifugal disk*. Several examples of Brγ line profiles from the disk wind and inner gaseous disk are presented in Fig. 7. All they are normalized to the stellar continuum. At these frequencies the disk also emits in the continuum. The profiles for 20° and 60° inclination angles are presented. The same model of the inner disk heated by the viscous dissipation is compared with the disk wind models 2 and 3 from Table 1. Parameters of the disk model are: $R_{in} = 2R_*$, $R_{out} = 10R_*$, $\dot{M}_{acc} = 1 \times 10^{-7} M_\odot$ yr^{-1}. The gas temperature is equal to 6000 K near R_{in} and decreases with the distance r. The emission from the hot midplane of the inner gaseous accretion disk can also slightly change the line profile and increase the intensity of the line profile but is substantially less than that from the disk wind.

The hot layers of the inner gaseous accretion disk are not able to contribute strongly into the hydrogen line emission but together with the emission from the outer photoevaporating wind they are able to modify the shape of the line profile, for example, to fill in a small gap between two peaks with additional emission and transform the shape of the profile from double-peaked to single-peaked.

3 Conclusion

Unlike low-mass T Tauri stars, the disk wind of Herbig Ae/Be stars contributes substantially to the hydrogen emission spectra; nevertheless, the region of the magnetosphere is also a source of the emission and has to be taken into account.

Combination of the disk wind parameters and inclination angles permits us to obtain a large variety of profile shapes.

Calculation of the interferometric functions together with the emission lines modeling gives strong constraints to model parameters and provides us with an additional information about the star plus disk system.

Acknowledgments. This research has been supported in part by the Russian Foundation for Basic Research (Projects 15-02-05399 and 15-02-09191).

References

1. *L. Hartmann, R. Hewett, N. Calvet*, Astrophys. J., **426**, 669, 1994.
2. *J. Muzerolle, N. Calvet, L. Hartmann*, Astrophys. J., **550**, 944, 2001.
3. *R. Kurosawa, T.J. Harries, N.H. Symington*, Mon. Not. Roy. Astron. Soc., **370**, 580, 2006.
4. *A. Königl, R.E. Pudritz*, in Protostars and Planets IV. Eds. V. Mannings, A.P. Boss, S.S. Russell. Tucson: Univ. Arizona Press, 2000, p. 759.
5. *J. Ferreira*, Jets from Young Stars. Lect. Not. Phys., No. 723. Berlin: Springer-Verlag, 2007, p. 181.
6. *J. Ferreira, C. Dougados, S. Cabrit*, Astron. Astrophys., **453**, 785, 2006.
7. *G. Weigelt, V.P. Grinin, J.H. Groh et al.*, Astron. Astrophys., **527**, 103, 2011.
8. *R. Garcia Lopez, L.V. Tambovtseva, D. Schertl et al.*, Astron. Astrophys, **576**, A84, 2015.
9. *A. Caratti o Garatti, L.V. Tambovtseva, R. Garcia Lopez et al.*, Astron. Astrophys., **282**, 44, 2015.
10. *I. Mendigutía, W.J. de Wit, R. Oudmaijer et al.*, Mon. Not. Roy. Astron. Soc., **453**, 2126, 2015.
11. *V.P. Grinin, N.A. Katysheva*, Izv. Krym. Astrofiz. Obs. (Bull. Crim. Astrophys. Obs.), **62**, 59, 1980.
12. *V.P. Grinin, A.S. Mitskevich*, Astrophys., **32**, 216, 1990.
13. *L.V. Tambovtseva, V.P. Grinin, B. Rodgers, O.V. Kozlova*, Astron. Rep., **45**, 442, 2001.
14. *V.V. Sobolev*, Moving Envelopes of Stars. Cambridge: Harvard Univ. Press, 1960.
15. *V.P. Grinin, L.V. Tambovtseva*, Astron. Rep., **55**, 704, 2011.
16. *L.V. Tambovtseva, V.P. Grinin, G. Weigelt*, Astron. Astrophys., submitted, 2016.
17. *R.D. Blandford, D.G. Payne*, Mon. Not. Roy. Astron. Soc., **199**, 883, 1982.
18. *P. Safier*, Astrophys. J., **408**, 115, 1993.
19. *L.V. Tambovtseva, V.P. Grinin, G. Weigelt*, Astron. Astrophys., **562**, A104, 2014.
20. *F.H. Shu, J. Najita, E. Ostriker, F. Wilkin*, Astrophys. J., **429**, 781, 1994.
21. *J. Muzerolle, P. D'Alessio, N. Calvet, L. Hartmann*, Astrophys. J., **617**, 406, 2004.

Relative Content of Be Stars in the Young Open Clusters

A.E. Tarasov[1]

E-mail: *aetarasov@mail.ru*

Based on high and medium resolution spectra, we analyze the population of Be stars in young open clusters. We have found a clear dependence of the relative content of early-type (B0–B3) stars on the cluster age. The relative concentration of Be stars of spectral types B0–B3 gradually increases with the cluster age, reaching its maximum value of 0.46 in clusters with ages of 12–20 Myr. The almost complete absence of Be stars in older clusters can be easily explained by the fact that B stars leave the main sequence. The few emission objects in clusters with ages of 1–7 Myr are most likely Herbig Be stars. Such a distribution of Be stars in clusters unequivocally points to the evolutionary status of the Be phenomenon. We also briefly consider the causes of this pattern.

1 Introduction

The Be phenomenon, the presence of emission (usually HI) lines in the spectra of normal B-type dwarfs and giants, is widespread. The relative content of Be stars is currently estimated to be about 17% of total number of Galactic B stars [1]. It is not completely clear why the geometrically thin and extended disks are formed [2]. These can be both the weakly decretion disks of single stars or binaries after mass exchange and the accretion disks of massive binaries at the first mass exchange stage [3]. The Be phenomenon is commonly observed in stars with a rotation velocity higher than its average and is probably unrelated to the ordinary outflow of matter from the star's equator [2, 4] unless it rotates with a critical velocity [5].

One of the key problems for understanding the Be phenomenon is to answer the question of whether the disks around B stars appear immediately after they have reached the main sequence (MS) or this is a characteristic of objects at the end of their MS life. Young open clusters undoubtedly are a good test for verifying these assumptions.

One of the first investigation of Be stars in open clusters was made in [6] where it was concluded that stars with a high angular momentum become Be stars at the end of their evolution on MS. In [7] the authors also obtained a similar result that Be stars occupy the entire MS, but the fraction of Be stars is at a maximum in clusters with the turn-off point in the region of spectral types B1–B2, and their

[1] Crimean Astrophysical Observatory of RAS, Russia

V. Grinin et al. (eds) Radiation mechanisms of astrophysical objects. Yerevan: Edit Print, 2017, pp. 253–260.

population decreases with increasing age. No clear age dependence was revealed in subsequent papers [8, 1].

Later on, the authors of [9] showed that the Be phenomenon is nevertheless an evolutionary stage and is observed for B stars in the second half of their MS life. Using photometry and spectroscopy for Be stars in open clusters, they concluded that emission objects are present in clusters with ages of less than 10 Myr, but these are mostly Herbig Ae/Be stars or other pre-main-sequence objects. In contrast, classical Be stars appear in clusters with age of 10 Myr, and the maximum number of such objects is observed in clusters with age of 12–25 Myr.

A plot of the relative population of Be star against the cluster age was constructed in [10]. It showed no clear dependence, although a larger number of Be stars is contained in clusters with ages of 25–100 Myr and, according to [11], in clusters with ages of 10–40 Myr. The authors of [11] point out that the maximum fraction of B stars with emission in their spectra is observed in clusters with ages 0–10 and 20–30 Myr. When studying the population of Be stars, the authors of [12] investigated objects of spectral types B0–B3 and separately B4–B5. They found that the fraction of Be stars of spectral types B0–B3 increases in clusters of the Magellanic Clouds with ages of 10–25 Myr.

As we see, the available data are so far insufficient, they give a blurred and largely contradictory picture of the nature of the Be phenomenon. Since the number of well-studied clusters is small, most of the authors analyzed Be stars of all spectral types, when studying the Be phenomenon, while objects of later spectral types (later than B3) are known to usually exhibit a weak line emission. Given that many authors studied the emission based on narrow-band Hα photometry or low-resolution spectroscopy, there is a high probability that not all later-type Be stars have been identified. These methods do not allow a weak emission to be clearly revealed in Be stars. In addition, the MS lifetime of late B stars is longer by order of magnitude. Therefore, since most authors use

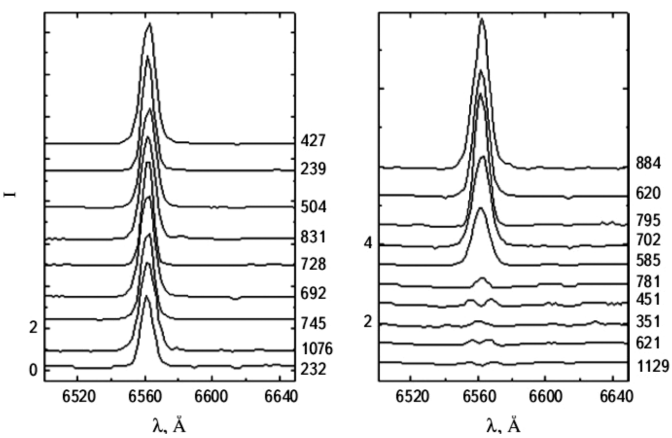

Figure 1: The Hα profiles of the selected Be stars in the open stellar cluster NGC 7419 [15]. Estimated age of the cluster is 14 Myr.

observational data for all B and Be, the age dependence of the fraction of Be stars is indistinct. For a proper analysis of the evolutionary status of Be stars, it is also important to determinate their position on the color-magnitude diagram and, accordingly, to determine the reddening coefficient. Considering Be stars in open clusters can partly help in this determinations. In some cases, however, significant reddening non-uniformity is observed within the cluster field, besides the additional reddening introduced by the envelopes of the Be stars themselves cannot be accurately taken into account either.

The spectroscopic data and, what is important, homogeneous studies of the age dependence of the population of B stars are very scarce, and the question about the nature of Be phenomenon currently remains unsolved [13, 14]. Therefore, the problem of studying Be stars in young open clusters based on high and medium resolution spectra remains topical.

2 Observations and age dependence of the Be stars fraction in clusters

During the last decade, based on high and medium resolution spectra taken with the 2.6 m telescope of the Crimean Astrophysical Observatory, we studied B and Be stars in nine open clusters with ages of 30–40 Myr: NGC 457, NGC 659, NGC 663, NGC 869, NGC 884, NGC 6871, NGC 6913, NGC 7419 and Berkley 86. To obtain a sample being complete and identical for B and Be stars and to analyze the age dependence, where possible, we restricted our study only to objects of early spectral types (B0–B3) when investigating the population of Be stars in young open clusters. Accordingly, the choice of clusters was also limited by the age less than 40 Myr, although there are Be stars in relatively older clusters, but these are generally stars of later spectral types (later than B3). We considered at least 60% of the Be stars in NGC 869, NGC 884, NGC 6913, NGC 7419 and took the spectra of all Be stars in NGC 457, NGC 659, NGC 5871 and Berkley 86. The example of Hα profiles of found and new Be stars in the open stellar cluster NGC 7419 is presented in Fig. 1. The results of our analysis of the relative content of early-type Be stars in the clusters studied are presented in [15, 16, 17, 18] and Table 1.

Table 1: The content of Be stars of spectral types B0–B3 in open clusters

Cluster name	Age, Myr	N(Be)	N(B+Be)	N(Be)/N(B+Be)
Berkley 86	6–8	1 (3)	15	0.07
NGC 457	11–20	4 (5)	15	0.27
NGC 659	12–20	4 (5)	16	0.25
NGC 663	18–25	16 (20)	50	0.32
NGC 869	12–14	20	47	0.43
NGC 884	12–14	18	39	0.46
NGC 7419	14	35 (37)	80	0.43
NGC 6871	6–12	2 (3)	14	0.14
NGC 6913	3–6	3	43	0.07

When constructing the age dependence of the fraction of Be stars, we took into account the data only for B0–B3 stars. However, since there is no spectral classification for some cluster member, we used the spectra in the wavelength range 4050–5200 Å for all observed objects to estimate their atmospheric parameters or to perform their spectral classification. The fraction of Be stars in the clusters was found as the ratio of the number of Be stars to the number of all B0–B3 objects (including the Be stars). When constructing the dependence, we also took into account the uncertainty in the relative number of Be stars and the estimated cluster ages. We calculated the upper limit for the estimated fraction of Be stars by taking into account the identified Be stars of spectral types B0–B3 and the Be candidates of the same spectral type.

The objects without any well-defined spectral type but with a probability that they are B0–B3 stars (as a rule, we used color-magnitude diagram for clusters) or objects, whose low-resolution spectroscopy showed some features indistinctly designed by the authors of the papers, were considered to be candidates. The third column (N(Be)) in Table 1 gives the number of Be stars and the possible maximum number of Be stars in the cluster (in parentheses), i.e. the sum of the identified Be stars and Be candidates.

Apart from the absence of spectral classification, the problem of cluster age determination also arose, because the estimations obtained by different methods often differ significantly. In addition, there are also large discrepancies in age determination when using the same method but with a different sample of program objects. We attempted to critically estimate the cluster ages. For all clusters, we constructed their color-magnitude diagrams with a set of isochrones (constructed from the data from [19]). We constructed the isochrones for each cluster by taking into account the already available reddening and distance modulus and then chose the most satisfactory reddening and distance modulus parameters. An example of this procedure is presented in Fig. 2. This allows us to estimate the age in a more homogeneous way. Our estimates of the ages, the number of B and Be stars, and the fraction of Be stars in each of clusters are given in Table 1.

In Fig. 3 the relative content of Be stars in the program clusters is plotted against the age. These data have a sufficient statistical significance, because we investigated almost all of the B0–B3 objects for their belonging to Be stars. As we see from the figure, the fraction of Be stars increases appreciably in clusters with ages of more than 10 Myr. This suggests that with a high probability the Be phenomenon is an evolutionary effect.

3 Discussion

Let us analyze in more details the data presented in Fig. 4 showing the gradual increase in the relative fraction of Be stars of spectral types B0–B3 with the cluster age.

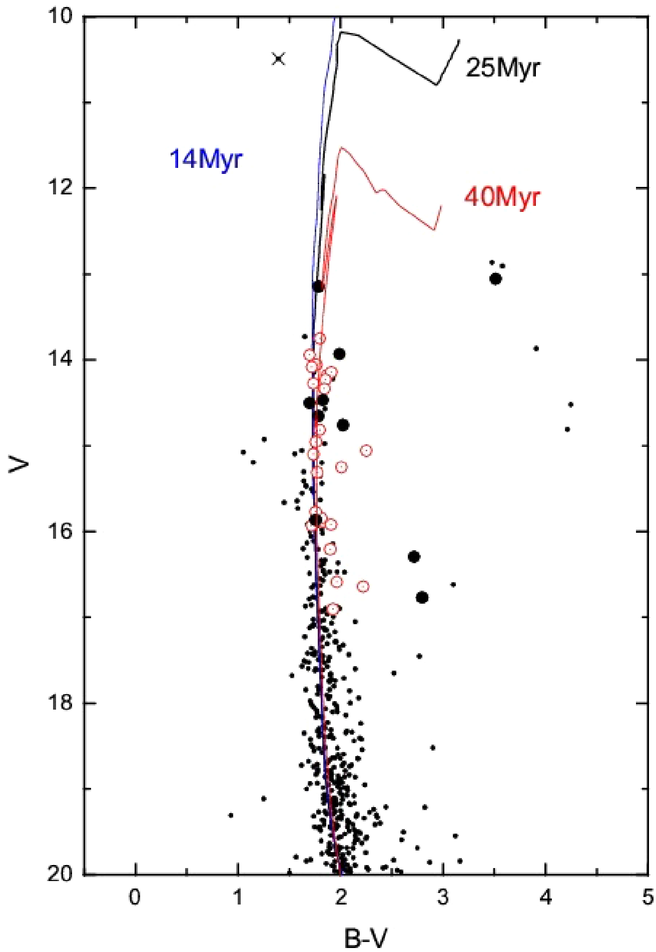

Figure 2: Example of the color-magnitude $((B-V)-V)$ diagram for the open stellar cluster NGC 7419 [16]. Open circles are for observed spectroscopically Be stars, large black circles for observed B stars. Three isochrones are presented for 14, 25 and 40 Myr.

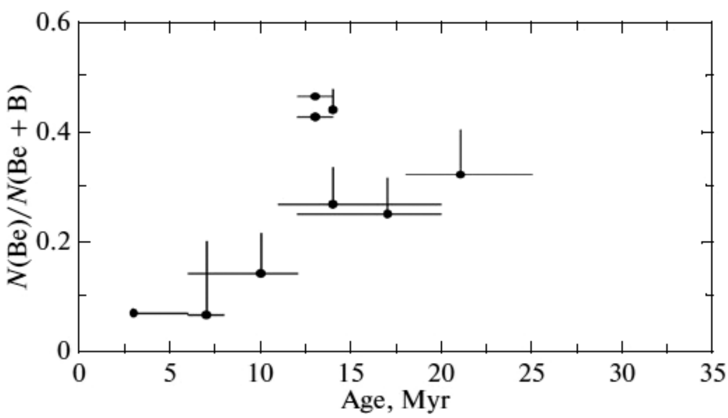

Figure 3: Relative number of Be stars versus cluster age (based on the data from Table 1).

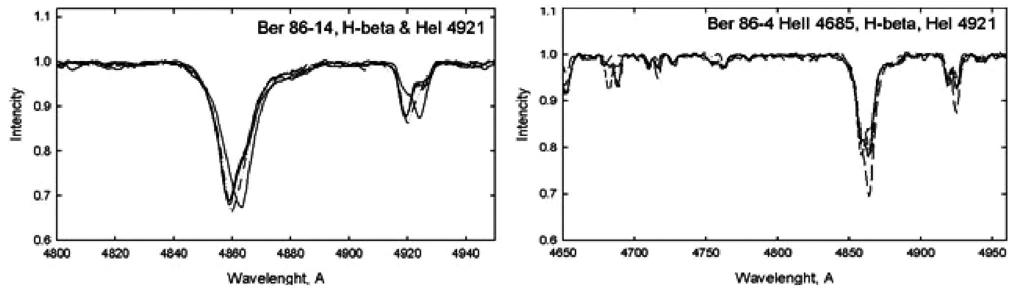

Figure 4: Two examples of spectral variability of the line double systems Ber 86 - 14 (P_{orb} < 4 days) and Ber 86-4 (P_{orb} < 2 days) in a very young open cluster Berkley 86 with age 6-8 Myr. Both systems have MS components.

According to [20], three evolutionary scenarios leading to the formation of disks around B stars are possible:

(A) Be stars were born as rapidly rotating B stars, and the HI line emission is observed throughout their MS life.

(B) The Be phenomenon arises in a single, sufficiently rapidly rotating B star during the change in its V/V_{crit} ratio (where V is the star's equatorial rotation velocity and V_{crit} is the critical equatorial rotating velocity) as the star moves from the zero-age main sequence (ZAMS) to the terminal age main sequence (TAMS) [13].

(C) Be stars are binary systems at the stage after active mass exchange.

Case A should probably be excluded from consideration. As we can see from Fig. 3, classical Be stars are observed very rarely in very young clusters, with ages of less than 8 Myr, and can be Herbig Be stars or pre-main-sequence objects with a high probability.

Case B, where V/V_{crit} ratio increases in the second half of the MS life of a rapidly rotating B star, was considered in detail in [13]. In particular, they showed that when the star is on MS, the equatorial rotation velocity of the star decreases significantly at the very end of its MS life. Thus, the V/V_{crit} ratio becomes the most important parameter. Assuming $V/V_{crit} \geq 0.7$ and solar metallicity for Be stars, any non-stationarities of the outer layers of Be stars, such as, for example, non-radial oscillations, can contribute to the outflow of matter from the stellar photosphere. According to these authors, a noticeable fraction of Be stars, 10-20% or, in a more optimistic case, up to 35%, are formed from single, rapidly rotating B stars during their MS life. For B0–B3 stars, this corresponds to an age of about 15–25 Myr. A comparison of these data based on the evolution theory and Fig. 3 obtained from observations suggest that this scenario is possible.

Case C, the formation of Be stars through mass and angular momentum exchange in close binary systems, was considered in detail by several authors (see [20, 21]). Spectroscopic studies of several young clusters in [14] point to an appreciable fraction of massive binaries in young clusters (about 25% of the total number of B stars). Moreover, since the latter authors performed only 2–3 episodic observations at close dates, one might expect that they revealed only short-period ($P_{orb} < 20$ days) massive binaries and did not detect numerous systems with the periods of 30–1000 days, typical of Be stars and mass ratio differing noticeably from one. Thus, the data from [14] may be reliably considered to be a lower limit for the fraction of binaries with B-type components in young open clusters. Clearly, all of the detected binaries will enter the phase of rapid mass exchange as soon as the more massive component leaves MS. In this case, the previously more massive component will become inaccessible to optical observations, because it will become either a helium star, or a white dwarf, or, in the most massive systems, an X-ray binary [20].

Our spectroscopic observations confirm data of [14]. In Fig. 4 we present two examples of spectroscopic binaries in a very young open cluster Berkley 86 (age of 6–8 Myr). The cluster has only one (possibly 3) early type Be stars but we found at least three short orbital period double systems and all of them have MS components.

Obviously, the scenario C is most natural as was pointed out, for example, in [21], and qualitatively describes our dependence of the relative content of Be stars at the end of their MS life. In the case where the V/V_{crit} ratio for a single B star evolves, it is necessary to prove that this star is actually a single object rather than a binary system with $P_{orb} < 1000$ days and a secondary degenerate component. This problem is known to be difficult and allows one to investigate only the brightest objects, which usually do not include the B and Be stars in open clusters.

Modern statistical investigations of the field B stars showed that among OB stars, whose evolution leads to the phase of active mass exchange, the relative fraction of double systems decreased with decreasing of spectral type of the primary MS component. As it was shown, for example, by authors of [22], among of O7–O9 stars relative concentration of double systems reaches 80%, 65% for B0–B1.5 stars and 55% for MS stars of spectral types B2–B3. Nearly the same values were found during the studying of Scorpios OB2 association [23]. These authors found that the relative fraction of double and multiple systems among B0–B3 stars and B4–B9 stars is 80% and 50%, respectively. All these statistical data again support the scenario C as the most natural explanation of our statistical results presented in Table 1 and Fig. 3.

4 Conclusions

The data considered revealed the pattern of distribution of the relative content of early-type Be stars in clusters of different ages. The maximum number of Be stars is observed in clusters with ages of 12–25 Myr. The increase in the number of Be stars in clusters with a certain age confirms the hypothesis that Be stars emerge when they leave the main sequence. On the other hand, the Be phenomenon can arise in binaries when the more massive component leaves the main sequence, which leads to mass exchange in the system and produces hydrogen emission lines in the spectrum. Both these effects operate simultaneously for single stars and binary systems.

References

1. *J. Zorec, D. Briot*, Astron. Astrophys., **318**, 443, 1997.
2. *J.E. Bjorkman, J.P. Cassinelly*, Astrophys. J., **409**, 429, 1993.
3. *A.E. Tarasov*, in Proc. IAU Coll. No. 175. The Be Phenomenon in Early Type Stars. Eds. M.A. Smith, H.M. Henrichs, J. Fabregat. Astron. Soc. Pacif. Conf. Ser., **214**, 644, 2000.
4. *Y. Flemat, J. Zorec, A.-M. Hubert, M. Floquet*, Astron. Astrophys., **440**, 305, 2005.
5. *R.H.D. Townsend, S.P. Owocki, I.D. Howarth*, Mon. Not. Roy. Astron. Soc., **350**, 189, 2004.
6. *R.E. Schild, W. Romanishin*, Astrophys. J., **204**, 493, 1976.
7. *J.C. Mermilliod*, Astron. Astrophys., **109**, 48, 1982.
8. *A. Slettebak*, Astrophys. J. Suppl., **59**, 759, 1985.
9. *J. Fabregat, J.M. Torrejon*, Astron. Astrophys., **375**, 451, 2000.
10. *M.V. McSwain, D.R. Gies*, Astrophys. J. Suppl., **161**, 118, 2005.
11. *B. Mathew, A. Subramaniam, B.Ch. Bhatt*, Mon. Not. Roy. Astron. Soc., **388**, 1879, 2008.
12. *J.P. Wisniewski, K.S. Bjorkman*, Astrophys. J., **652**, 458, 2006.
13. *S. Ekström, G. Meynet, A. Maeder, F. Barblan*, Astron. Astrophys., **478**, 467, 2008.
14. *W. Huang, D.R. Gies*, Astrophys. J., **648**, 580, 2006.
15. *C.L. Malchenko, A.E. Tarasov*, Astrophys., **51**, 250, 2008.
16. *C.L. Malchenko*, Odessa Astron. Publ., **21**, 60, 2008.
17. *C.L. Malchenko, A.E. Tarasov*, Astrophys., **52**, 235, 2009.
18. *C.L. Malchenko, A.E. Tarasov*, Astrophys., **54**, 52, 2011.
19. *T. Lejeune, D. Schaerer*, Astron. Astrophys., **366**, 538, 2001.
20. *O.R. Pols, I. Cote, L.M.F.M. Waters, J. Heise*, Astron. Astrophys., **241**, 419, 1991.
21. *W. Huang, D.R.. Gies, M.V. McSwain*, Astrophys. J., **722**, 605, 2010.
22. *R. Chini, V.H. Hoffmeister, A. Nasseri et al.*, Mon. Not. Roy. Astron. Soc., **424**, 1925, 2012.
23. *N.B.N. Kouwenhoven, A.G.A. Brown, H. Zinnecker et al.*, Astron. Astrophys., **430**, 137, 2005.

* The color figure is available online in the Proceedings at *http://www.astro.spbu.ru/sobolev100/*.

Model Approach for Inelastic Processes in Collisions of Heavy Particles with Hydrogen

S.A. Yakovleva[1], A.K. Belyaev[1]

E-mail: *cvetaja@gmail.com*

The quantum model approach within the framework of the Born–Oppenheimer formalism has been recently proposed to evaluate physically reliable data on rate coefficients for inelastic processes in collisions of atoms and positive ions of different chemical elements with hydrogen atoms and negative ions.

1 Introduction

Formation of spectral lines in stellar atmospheres is determined by many physical processes. Collisions of atoms and positive ions of different species with hydrogen atoms and anions are one of the main sources of uncertainties for non-LTE studies due to the high concentration of hydrogen [1].

The best way to get information on the rate coefficients for hydrogen collisions is to carry out full quantum studies. But these calculations are very time-consuming, and only a few collisional partners have already been studied at low collision energies. These are hydrogen collisions with hydrogen [2], helium [3], lithium [4, 5], sodium [6], and magnesium [7].

The data for hydrogen collisions are still rare, so the Drawin formula was widely used to estimate inelastic collision rate coefficients, although it has been shown [8] that the Drawin formula does not provide reliable data and can not be applied to charge transfer processes, which have been found to be the most important in astrophysical applications. A comparison of the rate coefficients obtained in full quantum studies and with the Drawin formula was performed in [8]. The rate coefficients obtained in quantum calculations are not larger than 10^{-8} cm^3/s, while the highest values for estimations by means of the Drawin formula are up to 10^{-2} cm^3/s, which is a huge value for an inelastic rate coefficient. Moreover, this formula gives zero rates for charge transfer processes, such as mutual neutralization and ion pair formation, which have been shown to have one of the largest values according to quantum calculations.

That is why it is important to develop and apply quantum model approaches that would provide reliable data, even approximate. Such quantum model approach for collisions of atoms and positive ions of different chemical elements with hydrogen atoms and negative ions was recently proposed in [9, 10].

[1] Dep. of Theoretical Physics and Astronomy, Herzen University, St. Petersburg, Russia

V. Grinin et al. (eds) Radiation mechanisms of astrophysical objects. Yerevan: Edit Print, 2017, pp. 261–264.

2 Quantum model approach

Low-energy atomic collisions are well described within the quantum Born-Oppenheimer approach. Within this framework the problem is solved in two steps. The first step includes electronic structure calculations. It can be based on accurate quantum-chemical data, if available. For many cases, accurate quantum-chemical data are not available, and approximate adiabatic potentials can be constructed via modeling of ionic-covalent interaction as described in [9]. Also it is possible to combine modeled potentials for higher-lying states with available *ab initio* potentials for low-lying states.

The second step includes non-adiabatic nuclear dynamics calculations. In the case, when adjacent states form several non-adiabatic regions, the probability current method described in [9] can be applied. The other option is to use multichannel formulas [10, 11], but they are only applicable for the case of ionic-covalent interaction (every pair of adjacent states form only one non-adiabatic region).

3 Results

The comparison of the results given by the quantum model approach and by full quantum study was performed in [7] for the case of magnesium-hydrogen collisions. Rate coefficients obtained in these studies are shown in Fig. 1.

The vertical axis represents results of the quantum model calculations, while the horizontal axis does results of the full quantum study. The symbols in Fig. 1 correspond to the rate coefficients of the partial processes, associated with

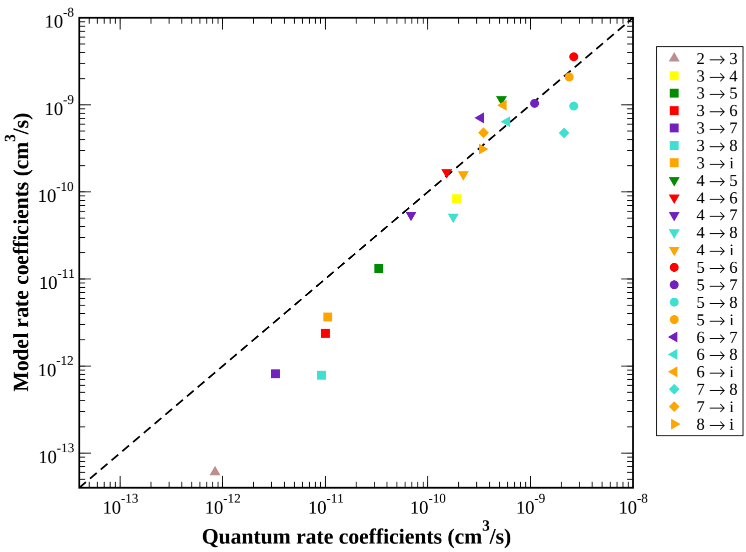

Figure 1: Comparison of the rate coefficients at $T = 6000\,\mathrm{K}$ for the case of Mg-H collisions.

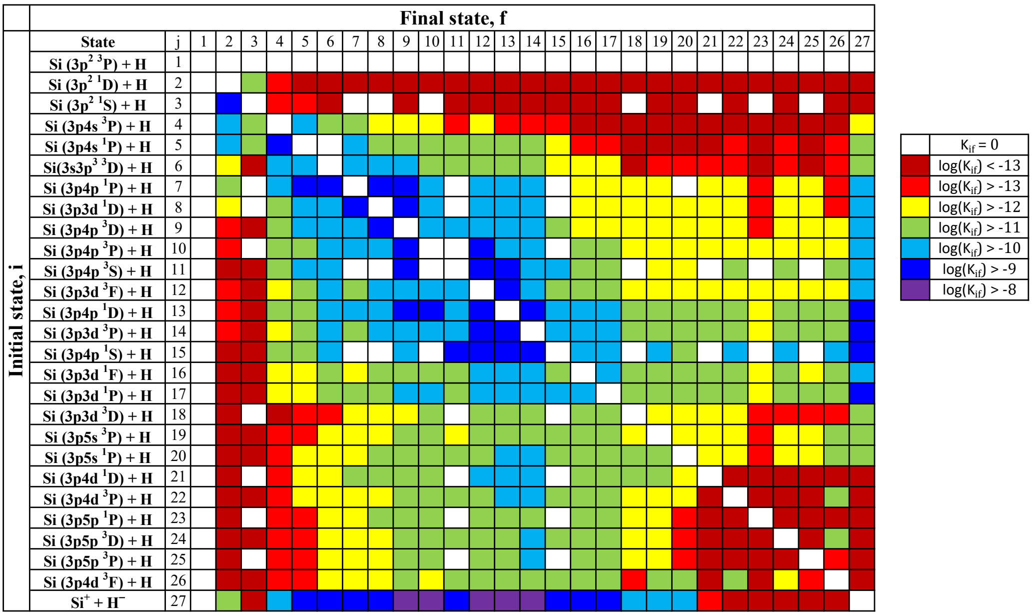

Figure 2: Rate coefficients (in cm^3/s) at $T = 6000\,\mathrm{K}$ for the case of Si-H collisions.

transitions between different molecular states numbered starting from the ground one (the index i corresponds to the ionic state). It is seen that the agreement for the rate coefficients with high and moderate values is quite good. While there are some deviations for the processes with small values of the rate coefficients, for which both the quantum model approach and the full quantum study give negligibly small values.

In [10], the quantum model approach was applied to silicon-hydrogen collisions. These calculations included 27 molecular states, and the heat map with the rate coefficients for different inelastic processes is represented in Fig. 2. The purple squares correspond to the highest rates, while white ones correspond to zero rates. It is seen that the highest values correspond to the charge transfer processes such as mutual neutralization and ion pair formation.

Acknowledgments. The partial support of the work from the Ministry for Education and Science (Russian Federation) and from the Dinasty foundation is gratefully acknowledged.

References

1. *M. Asplund*, Ann. Rev. Astron. Astrophys., **43**, 481, 2005.

2. *M. Stenrup, Å. Larson, N. Elander*, Phys. Rev. A, **79**, 012713, 2009.

3. *A.K. Belyaev*, Phys. Rev. A, **91**, 062709, 2015.

4. *H. Croft, A.S. Dickinson, F.X. Gadéa*, J. Phys. B, **32**, 81, 1999.

5. *A.K. Belyaev, P.S. Barklem*, Phys. Rev. A, **68**, 062703, 2003.

6. *A.K. Belyaev, P.S. Barklem, A.S. Dickinson, F.X. Gadéa*, Phys. Rev. A, **81**, 032706, 2010.

7. *M. Guitou, A. Spielfiedel, D.S. Rodionov et al.*, Chem. Phys., **462**, 94, 2015.

8. *P.S. Barklem, A.K. Belyaev, M. Guitou et al.*, Astron. Astrophys., **530**, A94, 2011.

9. *A.K. Belyaev*, Phys. Rev. A, **88**, 052704, 2013.

10. *A.K. Belyaev, S.A. Yakovleva, P.S. Barklem*, Astron. Astrophys., **572**, A103, 2014.

11. *A.K. Belyaev*, Phys. Rev. A, **48**, 4299, 1993.

* The color figures are available online in the Proceedings at *http://www.astro.spbu.ru/sobolev100/*.

Low-Energy Inelastic Magnesium-Hydrogen Collisions

D.S. Rodionov[1], A.K. Belyaev[1]

E-mail: *virtonoobne@bk.ru*

Available quantum calculations of cross sections for inelastic processes in $\mathrm{Mg} + \mathrm{H}$ and $\mathrm{Mg}^+ + \mathrm{H}^-$ collisions, that is, the processes of astrophysical interest, are analyzed. It is shown that cross sections with large values are calculated with high accuracy. The calculations include all transitions between the nine lowest adiabatic $\mathrm{MgH}(^2\Sigma^+)$ molecular states, with the uppermost of those diabatically extended to the ionic molecular state in the asymptotic region. Calculations also include transitions between five lowest adiabatic $\mathrm{MgH}(^2\Pi)$ molecular states. The inelastic cross sections with large values are stable with respect to a number of channels treated. The non-adiabatic nuclear dynamical calculations have been performed by means of the reprojection method in the framework of the Born–Oppenheimer approach, which provides reliable physical results.

1 Aims

The measurement of abundances of chemical elements in stellar atmospheres, as interpreted from stellar spectra, is of fundamental importance in modern astrophysics. Inelastic processes in collisions of different atoms with hydrogen atoms are important for the non-local thermodynamic equilibrium modeling of stellar spectra which is the main tool for obtaining relative and absolute chemical abundances [1, 2].

Magnesium is of particular astrophysical interest since it is an α-element produced by supernovae of type II. The spectral lines of such α-element provide diagnostic tools to study distribution with time of chemical abundances in stellar populations [2, 3, 4]. Neutral Mg lines give many spectral features in different wavelength ranges and are easily observed in spectra of late-type stars, even in the most extreme metal-poor stars, e.g. the oldest stars in the Galaxy. Thus, the need for investigation of inelastic collisions of hydrogen atoms with magnesium atoms is well justified.

2 Methods and results

Non-adiabatic nuclear dynamical calculations have been performed by means of the reprojection method [5] in the framework of the standard Born–Oppenheimer approach, which provides reliable physical results. The method takes into account

[1] Herzen State Pedagogical University, St. Petersburg, Russia

V. Grinin et al. (eds) Radiation mechanisms of astrophysical objects. Yerevan: Edit Print, 2017, pp. 265–266.

non-vanishing asymptotic non-adiabatic matrix elements, provides the correct incoming and outgoing asymptotic total wave functions, and removes non-adiabatic transitions between atomic-state channels in the asymptotic region. The present analysis of the reprojection procedure within the reprojection method shows a reliable convergence with respect to a number of channels treated.

We have performed full quantum calculations [6, 7] of cross sections and rate coefficients for all excitation and de-excitation processes for all transitions between the eight lowest atomic states of Mg in inelastic collisions with H, as well as for mutual neutralization processes in $\mathrm{Mg^+ + H^-}$ collisions and their inverse processes, the ion-pair formation ones, involving these Mg atomic states.

The first group of partial processes consists of the processes with large values of the cross sections, typically larger than $10\,\text{Å}^2$ for endothermic processes. The processes with the largest cross sections are $\mathrm{Mg(3s4s^1S) + H \to Mg^+ + H^-}$, $\mathrm{Mg(3s4s^1S) + H \to Mg(3s3d^1D) + H}$, $\mathrm{Mg(3s4p^3P) + H \to Mg(3s3d^3D) + H}$. The present calculations show that these cross sections are rather stable with respect to variation of a number of channels treated.

The second group consists of inelastic processes with moderate values of cross sections, typically with the values between $0.1\,\text{Å}^2$ and a few Å^2. This is the largest group. The processes of these two groups are important for astrophysical applications [2].

The third group consists of the processes with low cross sections. The inelastic processes for transitions between, from and to low-lying states (including the ground one) are typically in this group due to large energy splittings, which result in small non-adiabatic transition probabilities.

Acknowledgments. The work was partly supported by Ministry for Education and Science (Russian Federation).

References

1. *P.S. Barklem*, J. Phys. Conf. Ser., **397**, 012049, 2012.
2. *Y. Osorio, P.S. Barklem, K. Lind et. al.*, Astron. Astrophys., **579**, A53, 2015.
3. *R. Cayrel, E. Depagne, M. Spite et. al.*, Astron. Astrophys., **416**, 1117, 2004.
4. *K. Fuhrmann*, Mon. Not. Roy. Astron. Soc., **384**, 173, 2008.
5. *A.K. Belyaev*, Phys. Rev. A, **82**, 060701(R), 2010.
6. *A.K. Belyaev, P.S. Barklem, A. Spielfiedel et. al.*, Phys. Rev. A, **85**, 032704, 2012.
7. *M. Guitou, A. Spielfiedel, D.S. Rodionov et. al.*, Chem. Phys., **462**, 94, 2015.

Orbital Parameters and Variability of the Emission Spectrum Massive Double System 105 Tau

A.E. Tarasov[1]

E-mail: *aetarasov@mail.ru*

Using high resolution spectroscopy, we detected the weak lines of the secondary component in the known massive binary system 105 Tau. Orbital parameters of the system are derived. Observations show that both components are MS stars with the more evolved primary star. The orbital variability of the weak emission component in the profile of Hα line is found. Accretion disk is formed around the less massive secondary component.

Some massive double systems with the Main Sequence (MS) components demonstrate, as a rule, the presence of a weak emission component in the core of the Hα line. One of such systems is the well known single-lined binary system 103 Tau (HR 1659, HD 32990, Sp B3V, V $= 5.3^m$). The system was discovered as a single-lined spectroscopic binary in 1924 [1]. Its period ($P_{orb} = 58.25^d$) and orbital elements were found in [2] and corrected in [3]. The star has a weak emission component in the core of the Hα line [4].

For understanding nature of emission in the Hα line and obtaining an improved orbital solution of the system, we carried out high resolution spectroscopy of 103 Tau in the region of lines HeI λ 6678 Å and Hα in the coude focus of 2.6 m telescope of CrAO with the spectral resolution 30000 in 2001–2004.

In Fig. 1a we present two typical spectra in the region of the HeI λ 6678 Å line. As it is seen from the figure, we found a faint secondary component in orbital elongations and its intensity allows us to construct the orbit of the secondary and obtain the complete spectroscopic orbital solution of the system. Using the code FOTEL [5], we obtained an improved orbital solution with $P_{orb} = 58.305(3)$, $e = 0.277(27)$, $K_{prim} = 44.8(2.8)\,\mathrm{km\,s^{-1}}$, $K_{sec} = 79.3(8.7)\,\mathrm{km\,s^{-1}}$, $\gamma = 14.6(1.0)$, $M_{prim}\sin^3 i = 6.6\,M_\odot$, $M_{sec}\sin^3 i = 3.7\,M_\odot$, $a\sin i = 50\,R_\odot$ and $b\sin i = 88\,R_\odot$. Variability of the radial velocities with the phase of the orbital period and the orbital solution obtained are presented in Fig. 1b.

The rotational velocities of both components of the system are synchronized in periastron. For the primary component, $v\sin i = 47 \pm 11\,\mathrm{km\,s^{-1}}$ [6] is identical to $K_{prim} = 45.7 \pm 2.1\,\mathrm{km\,s^{-1}}$. Our estimates of the rotational velocity of the secondary have lower quality because of low intensity of the line, but it is less than 80 $\mathrm{km\,s^{-1}}$ and is close to the orbital value $K_{sec} = 78.9 \pm 6.2\,\mathrm{km\,s^{-1}}$.

[1] Crimean Astrophysical Observatory of RAS, Russia

V. Grinin et al. (eds) Radiation mechanisms of astrophysical objects. Yerevan: Edit Print, 2017, pp. 267–268.

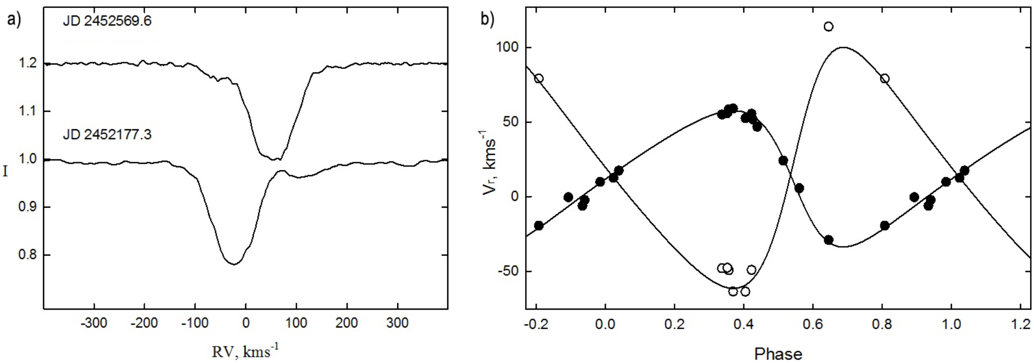

Figure 1: a) Spectral region around the HeI λ 6678 Å line. b) Radial velocity changes with the phase of the orbital period. Dots show the radial velocities of the primary component, open circles do the radial velocities of the secondary component.

Our analysis of the orbital variability of the faint emission component in the core of Hα line allows us to locate it in the Roche lobe of the secondary, which most probably is a late B star on MS. The primary, more massive component, is a MS or normal giant star that definitely has not reached its Roche lobe and cannot be an active mass loser. For the secondary, synchronization of the rotational and orbital velocities in periastron means that the accretion disc has appeared, which says about sporadic mass loss by the primary or recently started mass exchange.

References

1. *S.N. Adams, A.H. Joy, R.F. Sanford*, Publ. Astron. Soc. Pacific, **36**, 137, 1924.

2. *S.N. Hill*, Publ. Domin. Astrophys. Obs., **4**, 261, 1929.

3. *H.A. Abt, A.E. Gomez, S.G. Levy*, Astrophys. J. Supll., **74**, 551, 1990.

4. *J. Boulon, V. Doazan, N. Letourneur*, Astron. Astrophys., **40**, 203, 1975.

5. *P. Hadrava*, Prep. Astron. Inst. Czech. Acad. Sci., 1, 1991.

6. *W. Huang, D.R. Gies, M.V. McSwain*, Astrophys. J., **722**, 605, 2010.

Atomic Data for Inelastic Processes in Collisions of Beryllium and Hydrogen

Ya.V. Voronov[1], S.A. Yakovleva[1], A.K. Belyaev[1]

E-mail: *voronov_yaroslav@mail.ru*

The recently proposed model approach is applied to low-energy inelastic beryllium-hydrogen collisions for the purpose of obtaining quantum data for inelastic processes in beryllium-hydrogen collisions. The cross sections and the rate coefficients for the excitation, de-excitation, mutual neutralization and ion-pair formation processes are calculated.

1 Introduction

Atomic and molecular data on the inelastic processes in low-energy collisions of beryllium with hydrogen are important for astrophysical modeling of stellar atmospheres. Accurate quantum calculations are time-consuming and require accurate quantum-chemical input data. For this reason, it is important to develop and apply reliable model approaches, e.g. the approach described in [1, 2]. The approach is developed within the framework of the Born–Oppenheimer formalism and based on the asymptotic method [1] for construction of potential energy curves and on the multichannel formula [2] for calculations of non-adiabatic transition probabilities. It has been shown [2] that the data obtained by the model approach and by full quantum calculations are in good agreement for processes with large cross sections, i.e. the processes of the main interest for astrophysical applications.

2 Brief theory

A transition probability for a single passing of a non-adiabatic region created by molecular states k and $k+1$ is calculated within the Landau–Zener model [3]

$$p_k = \exp\left(-\frac{\xi_k^{LZ}}{v}\right), \quad \xi_k^{LZ} = \frac{\pi}{2\hbar}\sqrt{\frac{Z_k^3}{Z_k''}}\Bigg|_{R=R_c}, \tag{1}$$

with Z_k being a local minimum of an adiabatic splitting (see [3] for details). The total probability for a transition from an initial state i to a final state f is obtained by the multichannel formula [2]

[1] Dept. Theoretical Physics and Astronomy, Herzen University, St. Petersburg, Russia

V. Grinin et al. (eds) Radiation mechanisms of astrophysical objects. Yerevan: Edit Print, 2017, pp. 269–270.

$$P_{if}^{tot} = 2p_f(1-p_f)(1-p_i)\prod_{k=f+1}^{i-1} p_k \left\{1+\sum_{m=1}^{2(f-1)}\prod_{k=1}^{m}\left(-p_{f-\left[\frac{k+1}{2}\right]}\right)\right\}$$
$$\times\left\{1-\frac{\prod_{k=i}^{F} p_k^2\left(1+\sum_{m=1}^{2(i-1)}\prod_{k=1}^{m}\left\{-p_{i-\left[\frac{k+1}{2}\right]}\right\}\right)}{\sum_{m=1}^{2F}\prod_{k=1}^{m}\left(-p_{F+1-\left[\frac{k+1}{2}\right]}\right)}\right\}, \tag{2}$$

where F is a total number of open channels. The cross sections and rate coefficients are calculated as usual.

3 Results

Cross sections and rate coefficients of inelastic low-energy beryllium-hydrogen collisions for 12 covalent states and one ionic are calculated. The labels are shown in Fig. 1, where the channel $j = 13$ corresponds to the ionic one, $\mathrm{Be}^+(2s\ ^2S)$+H^-. Rate coefficients are presented in Fig. 1 in form of heatmap. It is seen that the largest rate coefficients correspond to non-adiabatic transitions between the ionic state, the Be($2s3p\ ^{1,3}P$), Be($2s3d\ ^3D$) and Be($2s3s\ ^1S$) states.

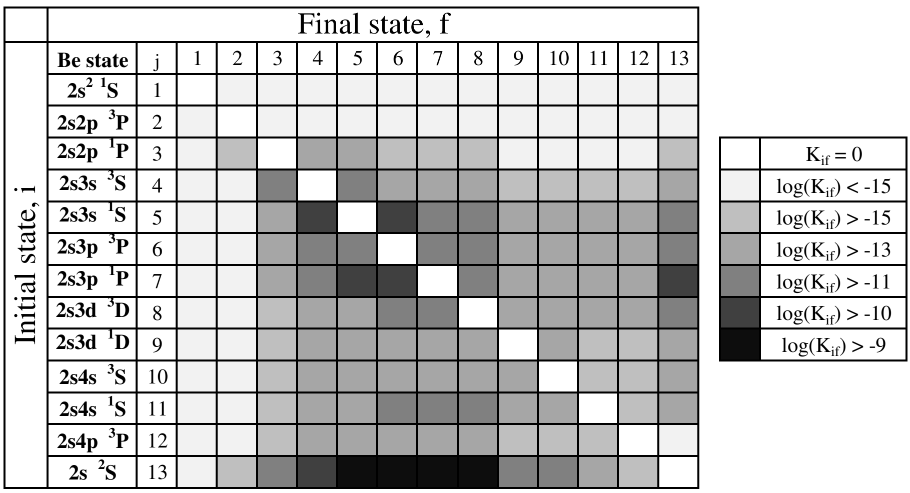

Figure 1: Calculated rate coefficients for Be+H, Be^++H^- collisions for $T = 6000$ K.

Acknowledgments. A support from the Ministry for Education and Science (Russia) is acknowledged.

References

1. *A.K. Belyaev*, Phys. Rev. A, **88**, 052704, 2013.

2. *A.K. Belyaev, S.A. Yakovleva, P.S. Barklem*, Astron. Astrophys., **572**, A103, 2014.

3. *A.K. Belyaev, O.V. Lebedev*, Phys. Rev. A, **84**, 014701, 2011.